BRILLOUIN ELASTOGRAPHY FOR MONITORING CELL BIOMECHANICS IN RESPONSE TO EXTERNAL STIMULI

A Dissertation

by

ZACHARY N. COKER

Submitted to the Office of Graduate and Professional Studies of
Texas A&M University
in partial fulfillment of the requirements for the degree of

DOCTOR OF PHILOSOPHY

Chair of Committee,	Vladislav V. Yakovlev
Committee Members,	Alexey M. Zheltikov
	Philip R. Hemmer
	Girish S. Agarwal
Head of Department,	Albert L. Ford

May 2021

Major Subject: Applied Physics

ABSTRACT

The biomechanical properties of tissues and their constituent cells are a critical component in determining their function, development, and overall wellness. As such, many approaches have been developed to measure these properties. Atomic force microscopy (AFM), magnetic twisting cytometry (MTC), particle-tracking microrheology (PTM), parallel-plates rheometry, cell monolayer rheology (CMR), and optical stretching (OS) are only some of the methods used to investigate cell and tissue biomechanics. These modern investigative methods are all either invasive and destructive or require the introduction of foreign agents, thereby changing the natural state of the sample. Optical techniques such as optical coherence elastography have shown promise and become more prevalent for tissue-level studies, but still require mechanical excitations and are limited regarding spatial resolution. The few optical techniques available are generally limited to either micro-scale or macro-scale measurements, and are not applicable at both tissue and cellular levels. Advances in spectroscopic methods, however, have provided a viable alternative capable of both micro- and macro-scopic measurements for both tissues and cellular level studies: Brillouin spectroscopy.

Brillouin spectroscopy is an all-optical, non-invasive, label-free investigative technique that has rapidly emerged as a powerful tool in biomedical sensing and imaging. The past 15 years have seen an expansive growth in Brillouin spectroscopy utilization and development. The implementation of static dispersion optics, a range of elastic scattering background removal techniques, and improved data analysis methods have helped to bring Brillouin spectroscopy to the forefront of elastography and use in biomedical applications. Recently, Brillouin spectroscopy has also been adapted for use as an imaging modality, enabling mechanical mapping of biological material properties.

This dissertation covers the development of a custom built high resolution multi-modal confocal microscopy system and its application to achieve a series of firsts in cellular level studies: the first non-contact recording of subcellular biomechanical changes in response to a non-specific external stimulus, the first reporting of sub-second biomechanical changes using spontaneous Bril-

louin spectroscopy, and the first reporting of sub-second dynamic biomechanical changes with location specificity in each of the cytoplasm, nucleoplasm, and nucleolar compartments of cells. The custom microscopy system is capable of simultaneous Raman and Brillouin spectroscopic measurements, allowing for measurement of both the chemical and mechanical properties from micro- or macro-level materials. This dissertation also provides details about a unique synergistic behavior between short picosecond optical and nanosecond electrical pulses that was discovered while considering surrogate exposure methods for generating transient pressure waves comparable to those produced by electrodes during nanosecond pulsed electric fields in cell culture exposures.

DEDICATION

To my loving family and friends who have supported me through this journey.

ACKNOWLEDGMENTS

If there was one fundamental truth that came to me about graduate school and doctoral research, it is that this journey is not meant to be taken alone. I cannot imagine where my research would be, or if I would have been able to reach this point in my academic career without the help and support of my colleagues, mentors, family, and friends.

Many people have contributed to the overall success of this project. First and foremost, I would like to express my sincerest gratitude to my research mentors who guided and coached me throughout my doctoral program: Dr. Vladislav V. Yakovlev of Texas A&M University who graciously served as my Research Advisor. Dr. Yakovlev has always advocated for his students success and encouraged testing of innovative and creative ideas. Likewise, Dr. Bennett L. Ibey and Dr. Joel N. Bixler, both of the Air Force Research Laboratory at Fort Sam Houston, TX, who served as my research sponsors and mentors for a combined total of 7 years. Both Dr. Ibey and Dr. Bixler have always made sure that I was engaged in what I was working on, helped to provide new perspectives and ideas, and always pushed me to better myself as an engineer and scientist. I would also like to express my gratitude to each of my committee members for their willingness to engage and for always being willing to make time in their busy schedules whenever I asked. Likewise, Dr. Alexey Zheltikov and Dr. Philip Hemmer were excellent instructors in Quantum Mechanics and Experimental Optics, respectively.

I would like to acknowledge and thank every member of Dr. Yakovlev's lab group and all of our collaborators; however, I would specifically like to express my gratitude to Dr. Maria Troyanova-Wood (Texas A&M University graduate and current NRC Post-doctoral fellow), who helped tremendously in the design and construction of the VIPA-based Brillouin spectrometer at Fort Sam Houston, and who was always eager to aid in carrying out experiments. She was not only a great friend and ally during the general difficulties of graduate life, but also an amazing lab partner that went above and beyond her own responsibilities to help others. Dr. Troyanova-Wood wrote a custom Python script for Brillouin spectral analysis that she distributed to other members

in the lab, such that all students in the group could have a "unified" approach to analysis of our collected Brillouin spectra and would not each have to wrestle with the tediousness of hunting for typos and missed keystrokes while programming our own. Dr. Andrew Traverso (Texas A&M University graduate) also a former laboratory member, who allowed me to inherit the 780 nm base Brillouin spectroscopy system that he had designed and built when I first began my research with Dr. Yakovlev's group, allowing me to jump straight in to research, making mistakes, and learning things the hard way. I'd like to thank Dr. Georgi Petrov of Texas A&M University who was always encouraged clever solutions to problems, provided guidance in finding answers to questions, and was always willing to share his abundance of knowledge and experience with suggestions for most all optics-based problems.

I would like to thank Allen Kiester who built a custom motorized microscope stage, enabling raster scanning for developing 2D Brillouin maps and images. Likewise, I would like to thank Gary Noojin (SAIC), for his willingness to always provide suggestions and help in guiding me toward reasonable solutions when all else seemed to fail.

I would like to specifically thank Dr. Alfred Vogel and Dr. Xiao-Xuan Liang (Institut für Biomedizinische Optik, Universität zu Lübeck) who, through sharing their deep knowledge of physics and ionization mechanisms, and specifically Dr. Liang's development of our mathematical model and simulation, were truly invaluable in successfully publishing our work earlier this year that has since been selected as an Editor's Pick in the journal *Photonics Research*.

I have received an abundance of support and encouragement from colleagues who are not directly related to my work, but who have helped me to learn and develop the technical skills necessary to complete it, or who have contributed to discussions that have helped to advance my knowledge and this work. Thus, I would like to thank, in no particular order: Dr. Caleb Roth, Dr. Ronald Barnes, Dr. Chris Valdez, Stacey Martens, Dr. Brett Hokr, Dr. Dawson Nodurft, Dr. Sunny Guha, Cesario Cerna, Dr. Hope Beier, Dr. Charles Ballmann, Dr. Jonathan Thompson, and Dr. Gary Thompson.

CONTRIBUTORS AND FUNDING SOURCES

Contributors

This work was supported by a dissertation committee consisting of Professors Vladislav V. Yakovlev, Alexey M. Zheltikov, and Girish S. Agarwal of the Department of Physics & Astronomy, and Professor Philip R. Hemmer of the Department of Electrical & Computer Engineering .

The mathematical model and simulation for opto-electric breakdown in Chapter 5 was developed and provided by Dr. Xiao-Xuan Liang (Institut für Biomedizinische Optik, Universität zu Lübeck) as part of a collaborative effort with the Air Force Research Laboratory and was published in the journal *Photonics Research* March of 2021.

A custom spectral analysis code for analyzing Brillouin spectroscopy data was written and provided by Dr. Maria Troyanova-Wood. Specifically, this code was used for data analysis presented in chapter 4. Dr. Troyanova-Wood distributed this Python code to students shortly after her graduation and departure from the Texas A&M University lab group. Dr. Joel N. Bixler wrote a background subtraction code in Matlab that was used prior to analysis of the Raman spectra acquired from cell structures, as presented in Chapter 4.

All other work conducted for the dissertation was completed by the student independently.

Funding Sources

Graduate study and research efforts were supported by Texas A&M University, a fellowship from the Consortium Research Fellows Program, and SAIC under Air Force Research Laboratory (AFRL) contract #FA8650-C-6024.

TABLE OF CONTENTS

Page

LIST OF FIGURES

FIGURE Page

LIST OF TABLES

TABLE Page

1. INTRODUCTION

As our overall body of scientific knowledge and our technology advance, the perceived lines between the traditional scientific and engineering disciplines blur and begin to vanish. In 1969 Nils Roll-Hansen wrote a paper titled, *On the Reduction of Biology to Physical Science* [1]. In this article he stated that, "a characteristic feature of the development [for biological science] has been the steady inflow of new methods and theoretical viewpoints from physical sciences (physics and chemistry)." More than 50 years later, this sentiment is true across all scientific fields. The terms biochemistry, biophysics, chemical engineering, engineering physics, and bioengineering are all ubiquitous across university campuses and science conferences. It should be of no surprise that fields like "biomechanics and biochemistry have gained traction. A new frontier has emerged at the interface of biology, physics, and engineering with the field of mechanobiology. Mechanobiology is a rapidly emerging field focused on how the mechanical properties of biological materials and the physical forces actingon them influence cell and tissue behavior, morphogenesis, and disease progression [2]. Such mechanical properties and interactions have been identified as fundamental to many basic behaviors, such as cell reproduction, cell migration, and stem cell differentiation [3, 4, 5, 6, 7]. In fact, most pathological and physiological processes involve changes in the mechanical and chemical properties on both tissue and cellular levels. For example, studies have implicated cell stiffness as a biomarker for metastatic potential of cancer cells, and the cells within tumor tissue exhibit different mechanical properties based on their location within the tumor itself [8]. Likewise, variations in phospholipid and protein concentrations have been associated with cancer transformations in the membrane of human colorectal cancer cells [9]. Likely the most common known example is physician encouragement for patients to perform self-examinations and check for breast or testicular cancer. This is done by checking for abnormal lumps of dense or hard tissue that could indicate the presence of a tumor. Cellular stiffness has been implicated as a biomarker for cancer cell metastatic potential and cells within tumors exhibit different properties based on their location within the tumor [8]. Measuring the mechanical (elastic and viscoelastic) properties

of tissue and cells *in situ* can provide critical information for advancing our understanding of cells, tissues, their environments, disease pathology, and how they change in response to stresses and stimuli. This relationship between the mechanical properties and disease is the hallmark of elastography-based medical diagnostics.

Elastography is the field of research that aims to study the elastic properties and stiffness of tissue with the main purpose being to measure differences in tissue properties leading to diagnostic information. Elastography is a relatively young field, having been established in the 1990s [10]. Since then it has experienced rapid growth and development. Engineers and scientists have devised several tests for measuring the mechanical properties in both bulk and micro-scale materials (tissues and cells); however, biologically safe methods for micro-scale investigation remain elusive. One challenge in biomechanics and elastography is that the small-scale structures of biology require microscopic spatial resolutions, while most testing methods for these spatial scales are invasive, destructive, or require the use of exogenous materials that cannot be excised from tissue or cells. Ideal tests should be wholly non-invasive such that the measurements themselves do not influence or alter the behavior of living samples. Recent developments in spectroscopic methods and dispersion optics have positioned a new technique, Brillouin spectroscopy, to help fill this niche role in mechanobiology for biologically safe microscale elastographic measurement and imaging.

The goal of this dissertation was to establish Brillouin spectroscopy as a viable means to measure and observe the mechanical properties of cells and sub-cellular components in response to external stimuli. As such, this dissertation provides details about the development of a high resolution multi-modal confocal microscopy system capable of simultaneously measuring both the chemical and mechanical properties of micro-scale materials, its application for measuring the biomechanical properties of cells, and how those properties change in response to an external stimulus. The manuscript begins by providing the motivation for this work, including a brief overview relating the goals of this study to past works conducted by the High Peak Power Microwave laboratory group (Air Force Research Laboratory, 711$^{\text{th}}$ Human Performance Wing, Airman Systems Directorate HPW/RHDR) on cellular responses to externally applied electric fields. The introduction

concludes with a brief abstract for each of the investigations carried out through the course of this study to provide the reader with a quick reference for each chapter. Chapter 2 begins with an overview of optical scattering phenomena, starting with the physical principles and governing theory, then an introduction to both Raman and Brillouin scattering processes and related spectroscopy methods. Detail about how to interpret Brillouin spectra and how to extract a materials mechanical properties from acquired spectra is provided. Chapter 2 concludes with a brief discussion of the historical developments of Brillouin spectroscopy and provides a look at the modern state of the art for Brillouin applications. Chapter 3 provides information regarding the development and instrumentation of a custom multi-modal Brillouin spectroscopy system. An assessment of the spectrometers performance against a scanning multi-pass Tandem Fabry-Perot Interferometer (TFPI), historically considered the "standard" method for Brillouin spectroscopy investigations, is also provided in Chapter 3. Chapter 4 presents the experimental details, results, and and discussion regarding our time resolved Brillouin spectroscopy investigations of cellular biomechanics and cell responses to an external electrical impulse. Chapter 5 describes the discovery of a synergistic effect between picosecond optical and nanosecond electrical pulses on dielectric breakdown in aqueous solutions. This effect was discovered while trying to find more efficient means of achieving pressure transients from cavitation bubbles via optical breakdown to emulate the mechanical vibrations induced by nanosecond pulsed electric fields in cell culture solutions. Chapter 5 also provides a detailed description of the experimental methods used and a supporting theoretical model that was developed by collaborators from the Institut für Biomedizinische Optik at Universität zu Lübeck. The final concluding remarks are presented in Chapter 6.

1.1 Motivation

The High Peak Power microwave (HPPM) laboratory at Fort Sam Houston, Texas is dedicated to understanding the impact that high voltage electric fields have on cells and tissues. Specifically, we have focused on understanding how cells are impacted by exposure to high voltage nanosecond electric pulses (nsPEF), a surrogate for free field high peak power microwaves. The primary insult experienced by the biological system, due to the brevity of the pulse, comes directly from the

strong directional electric field rather than secondary sources like thermal deposition. We have identified critical biological pathways that are activated by electric field induced breakdown of cell plasma membranes [11, 12, 13, 14, 15, 16, 17, 18]. These biological pathways mirror multiple known stress response pathways in biological systems.

Interestingly, cells appear to respond to these short electric pulses in a manner similar to that of mechanical stressors rather than thermal or chemical induced stressors. We have also found that different cell lines often exhibit different responses and damage thresholds under the same pulse exposures. These observations formed the seminal hypothesis that electric fields acting on cells in the short pulse high energy regime manifest as biomechanical interactions instead of a purely electrical phenomena (as has been postulated and modeled). This hypothesis aligns with that of Zimmerman et al. who suggested that Maxwell-Wagner polarization of the cell, represented as two cavities with mismatch conductivity, will generate a pressure force that will act on the cell membrane and can lead to disruption in the form of electroporation or electropermeabilization [19]. Such a pressure force would activate pressure sensitive mechano-receptive channels and elicit a downstream biological response that mirrors mechanical stress. Additionally, as these strong electric fields are delivered by two nearby electrodes, we hypothesized that acoustic waves generated by the mechanical vibrations from the electrode pair may cause membrane damage through a sonoporation type effect [20]. We have has since validated that such acoustic waves are indeed generated by the nsPEF electrodes through use of a probe beam deflection microscopy technique. The study also showed that acoustic waves generated by the electrodes have sufficient intensity to adversely impact plasma membrane health [21].

Based on this hypothesis, we utilized AFM and fluorescent microscopy to measure the mechanical rigidity of cells and the organization of the cell cytoskeleton (the apparatus responsible for much of a cells rigidity and structure) [22, 23, 24]. The results demonstrated that cellular rigidity could be used as a predictor of cell sensitivity to electric fields in that softer cells are inherently be more sensitive (i.e. react at a lower exposure threshold). We also found that after nsPEF exposure, cells became less rigid leading to higher sensitivity to subsequent pulses. Based on these findings,

our goal became to understand the biomechanics of a cell before and after exposure to electric pulses to both predict susceptibility and to better understand the downstream responses. Specifically, as opposed to AFM, we sought a noncontact method that could resolve spatial changes in bulk mechanical properties (elastic moduli) across a single cell. This is critical as electric fields applied to cells are generally directional. Being able to resolve both the bulk changes in the cellular biomechanics and any directionality to this response would inform our biomechanical interaction hypothesis.

Additionally, have observed that bipolar nsPEF exposures (two subsequent pulses with the electrode polarity inverted for the second pulse) cause substantially less response from cells than would otherwise occur from a single pulse stimulus [13, 25, 26, 27, 28, 29]. In the bipolar configuration, such fields can generate mechanical pressure waves that travel in opposite directions and destructively interfere to yield a small net pressure force on the cell leading to a smaller response. Membrane changing and discharging measurements with high-speed imaging systems have validated that the electric field is present on the plasma membrane and felt by the cell. It is likely a summation of forces that results in bipolar fields having substantially less impact on cell membranes. Efforts to model bipolar exposures as facilitated discharge of the plasma membrane have failed to provide a logical explanation for such cancellation of field effects [30]. We conclude that this is another example of how pulsed electric fields act on a cell as a mechanical system with much longer time constants than would be expected from electrical charging. Specifically, we have observed that the delay between pulse phases must be 10 μs or greater to elicit a strong cellular reaction (calcium or YO-PRO-1 dye uptake into the cell) [26].

Ultimately, framing the research into high power microwaves as a biomechanics problem is novel and enables our team to better understand why environmental and chemical changes in cells cause drastic alterations in cell sensitivity to electric field exposures. Brillioun microscopy, albeit too slow to resolve the mechanical waves produced by nsPEF exposures, would be a valuable tool in assessing whether lasting mechanical changes occurred within cells subject to these types of electrical and mechanical insults.

Lastly, though we postulate that pulsed electric fields are felt by the cells as mechanical forces, we lack a method to validate the cellular response to rapidly applied mechanical fields. This is a difficult physical separation to achieve as the electric field is manifesting the mechanical pressure either externally at the electrodes or internally within the cells via polarization. We engineered a system capable of producing laser induced breakdown at a distance from the cell to isolate the impact of rapidly applied mechanical forces on the cell membrane without an electric field. This breakdown generates cavitation bubbles that collapse and produce acoustic waves that can be adjusted in intensity (by distance from the cell) mirroring waves measured between the electrics during a high-power pulsed field exposure. We investigate whether a simultaneous application of pulsed electric field and short picosecond laser pulse could allow for a reduced breakdown threshold to improve the efficiency of breakdown experiments in biologically relevant liquids and to enable precise control of breakdown timing. We discovered an interesting synergy between the two types of pulses that indeed does lead to reduced breakdown thresholds in biological solutions. This synergistic behavior could be valuable in multiple applications related to breakdown spectroscopy, combined cellular poration, clinical therapy for cancer, laser-based micro- and nanosurgeries, and increased electro transfer of genetic material into cells.

1.2 Quick reference - individual chapter summaries

1.2.1 Chapter 2 - Optical scattering and spectroscopy

Light scattering is the fundamental process behind spectroscopy and spectroscopic measurements used to characterize a material's chemical and mechanical properties. This chapter first provides an introduction to the basic principles of optical scattering, a brief discussion on both Raman and Brillouin spectroscopy, the relevant information for understanding the inelastic scattering phenomena that enable them, and how to interpret their respective spectral measurements. The chapter then provides a review of the history and development of Brillouin spectroscopy and then concludes with a look at some state-of-the-art Brillouin applications.

1.2.2 Chapter 3 - Modern Brillouin spectroscopy and instrumentation

Brillouin spectroscopy and imaging has experienced a renaissance in recent years seeing vast improvements in methodology and an increasing number of applications. This resurgence has sparked the development of new spontaneous Brillouin instruments that often tout superior performance compared to conventionally established and commercially available systems such as tandem Fabry-Perot interferometers (TFPI). The performance of these new systems is often neglected beyond discussing the relevant application, as applications and immediate results often take precedence. We, therefore, present an evaluation of three modern Brillouin spectrometers: two VIPA-based with wavelength-specific notch filters, and one scanning 6-pass TFPI. Performance analysis is presented along with a discussion about the dependence of measurements on excitation laser sources and the various susceptibilities of each system.

1.2.3 Chapter 4 - Brillouin spectroscopy: cellular and sub-cellular biomechanics in response to external stimuli

Modern methods for probing viscoelastic and rheological properties of cells and small-scale tissues are limited to mostly invasive and destructive means. Recent advancements have positioned Brillouin spectroscopy as a viable non-invasive method to assess viscoelastic properties of living systems. Here, we utilize a custom multimodal imaging and spectroscopy system to monitor the viscoelastic response of cells and subcellular structures to a non-specific external stimulus. The viscoelastic properties of three regions within CHO-K1 cells (cytoplasm, nucleoplasm, and nucleoli) were monitored for their dynamic changes in response to single 600 ns electric impulses of various field intensities. This proof-of-principle study demonstrates the capability of Brillouin spectroscopic imaging to visualize the biomechanical response of subcellular structures to external stimuli. Our results can be used to quantify viscoelastic changes within individual subcellular components in response to external stimuli and support the promising future of Brillouin spectroscopy within the broad scope of cellular biomechanics.

1.2.4 Chapter 5 - Synergistic effect of picosecond optical and nanosecond electric pulses on dielectric breakdown

The combined effect of short (picosecond) optical and (nanosecond) electrical pulses on dielectric breakdown is investigated both theoretically and experimentally. It was demonstrated that nanosecond pulsed electrical fields (nsPEFs) applied simultaneously with picosecond optical pulses can reduce the optical pulse energy required to achieve breakdown. Experimental results and an extended model for opto-electrical-induced breakdown are discussed. The newly unveiled effect is expected to play a significant role in spatially confined electroporation and further advances in laser-ablation-based processes while also allowing for measurements of ambipolar diffusion constants.

2. OPTICAL SCATTERING AND SPECTROSCOPY

Light scattering is the fundamental process behind optical spectroscopy and the spectroscopic measurements used to characterize various properties of a sample material. This dissertation primarily focuses on the use of inelastic scattering from molecular and mechanical vibrations; therefore, this chapter first provides an introduction the basic principles of optical scattering from small particles. The following sections then provide relevant information needed to understand the inelastic optical scattering phenomena that enable Raman and Brillouin spectroscopy, and how to interpret their spectra. The chapter concludes with a brief, generalized history and development of Brillouin spectroscopy and a review of today's state-of-the-art Brillouin spectroscopy and imaging applications.

2.1 Basic principles: light scattering from small particles

In general, light scattering is a weak process; only a small portion of light incident on a transparent medium is scattered, while most of the light transmitted or absorbed. To examine this, we can consider an ideal scattering case where the electric field $\boldsymbol{E_i}(r,t)$ of a monochromatic beam of light is incident on a sample volume. The electric field $\boldsymbol{E_i}(r,t)$ is described as a plane wave with wavelength λ, amplitude E_0, angular frequency ω_i, and propagation vector $\boldsymbol{k_i}$, which has the expression:

$$\boldsymbol{E_i}(\boldsymbol{r},t) = \boldsymbol{n_i} E_0 \exp\left[i(\boldsymbol{k_i}\cdot\boldsymbol{r} - \omega_i t)\right] \tag{2.1}$$

where $\boldsymbol{n_i}$ is a unit polarization vector (this unit vector also describes the direction of the incident electric field, perpendicular to the direction of propagation). The vector $\boldsymbol{k_i}$ is then defined by:

$$\boldsymbol{k_i} = (\frac{\omega_i}{c})\hat{\boldsymbol{k}}_{\boldsymbol{i}} \tag{2.2}$$

where $\hat{\boldsymbol{k}}_{\boldsymbol{i}}$ is the unit vector in the direction of propagation and c the speed of light. This description of an electromagnetic wave stems from Maxwell's equations [31] and is the most simple form

fundamental solution to the wave equation, given in Eq. 2.3:

$$\nabla^2 \mathbf{E} - \frac{1}{c^2}\frac{\partial^2 \mathbf{E}}{\partial t^2} = 0 \tag{2.3}$$

where $c = 1/\sqrt{\epsilon\mu}$ with ϵ and μ the *permittivity* (dielectric constant) and *magnetic permeability* respectively.[1]

When such an electromagnetic wave is incident on a sample, the individual molecular components can be considered as individual small particles (i.e. particles with radius $a \ll \lambda$) on which the field induces a dipole moment **p** parallel to the polarization of the incident electric field:

$$\mathbf{p} = \alpha_p E_i \tag{2.4}$$

where α_p is the polarizability of the particle due to changes in permeability (charge separation) in the particle volume. Oscillations of this induced dipole, accelerated by the incident electric field, cause emission of a new electromagnetic wave of equal frequency. This process is known as *Rayleigh scattering*. The far-field radiation created by oscillating dipoles gives the expression for the scattered electric field in vacuum (where observer distance r $\gg \lambda$):

$$\boldsymbol{E_s} = -\frac{1}{4\pi\epsilon_0}\left(\frac{\omega}{c}\right)^2 \frac{1}{r^3}\mathbf{r} \times (\mathbf{r} \times \mathbf{p}) \tag{2.5}$$

The intensity of light scattered or radiated from oscillations of a single dipole is $I_s \propto |\boldsymbol{E_s}^2|$ and is given by:

$$\frac{I_s}{I_i} = k_s^4 \frac{sin\theta^2}{r^2}\alpha_v^2 \tag{2.6}$$

where I_i is the intensity of the incident electromagnetic radiation, k_s the wavenumber of the scattered light, and α_v the volume polarizability $\alpha_v = \alpha_p/4\pi\epsilon_0$. Aside from the standard expected intensity dependence on the distance of the observer or detector from the scattering source, an

[1] A brief, yet simple derivation of the wave equation from Maxwell's equations has been provided in Appendix A for the readers convenience.

important relationship to the scattering intensity is the *Rayleigh law*, i.e. $I_s \propto \lambda^{-4}$. (See Jackson, Ch. 9 for a detailed derivation of the intensity distribution given by the time averaged magnitude of the *Poynting vector*[32].) These relationships and the scattering process described provide the foundation of this following chapter.

2.2 Inelastic scattering and spectroscopy

When a light source such as a laser is incident on a material, that light can be scattered either elastically or inelastically. A majority of the scattering that occurs is elastic *Rayleigh scattering* that produces photons of the same wavelength as the incident light. A small percentage of the scattering, however, is inelastic scattering which produces photons of slightly different energy or wavelength from that of the incident light. This section presents a general overview of the two scattering phenomena of interest to this dissertation: Raman and Brillouin (or Brillouin-Mandelstam) scattering and their respective spectroscopic techniques.

2.2.1 Raman scattering and spectroscopy

Raman scattering occurs when incident photons interact with the rotational, translational, and vibrational modes of molecules within a material or medium and exchange energy, thereby producing or emitting photons of different energy and frequency. The energy exchange interactions occur via an excitation-emission scattering process where the incident photons are absorbed and subsequently emitted via an intermediate virtual energy state (sometimes referred to as (ro)-vibrational energies). The resultant scattered photons are emitted with slightly increased (anti-Stokes) or decreased (Stokes) frequency. This energy-exchange process must obey the laws of energy and momentum conservation, thus the newly scattered photons shifted" frequency is equal to the difference in the vibrational energy levels of the material's constituent molecules (typically on the order of 1-100 THz). Therefore, the Raman scattered photons carry with them information on the energy levels of the molecules within the target material. The first theoretical description of the Raman scattering effect was published in 1922, by Indian Physicist Sir Chandrasekhara Venkata Raman

[33]. The first experimental demonstration of Raman scattering was published in 1928 [34, 35].[2]

Measuring the changes in photon energy (frequency) from Raman scattered light is the fundamental principle for Raman spectroscopy. The change in frequency of the scattered light can be mathematically described as $\omega_s = \omega_i \pm \omega_{vib}$ where subscripts s, i, and vib denote the scattered photon, the incident photon, and the molecular vibrations, respectively. Figure 2.1 provides a visualization of the quantum particle interpretation of the Raman effect and virtual energy levels.

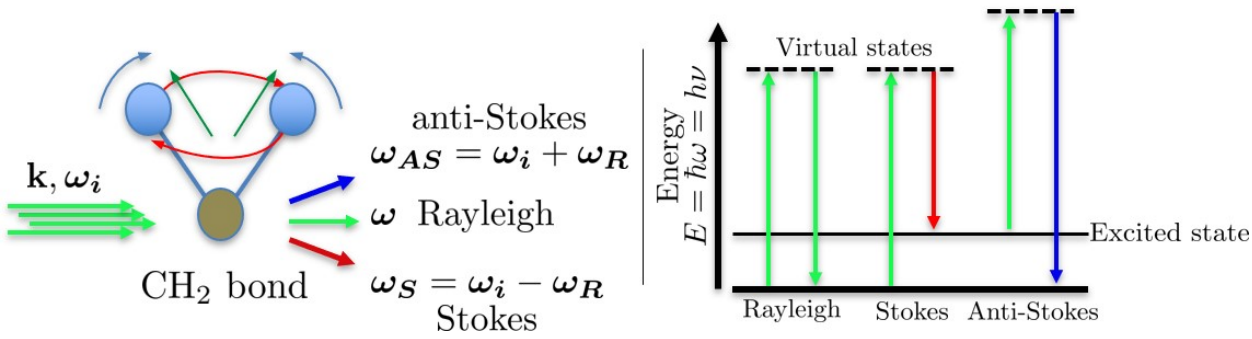

Figure 2.1: Visualizing Raman scattering. (Left) molecular vibrations and scattering diagram to display the different molecular vibration modes. (Right) Jablonski diagram of quantum energy transitions for Rayleigh and Raman scattering processes with indications to the virtual energy levels. When spontaneous Raman scattering occurs, the molecules may be excited to a higher virtual energy state, and the energy of the scattered photon is lowered by that same excitation energy. Conversely a molecule that is already in an excited state may be reduced to the ground state by the incident photons, leading to an anti-Stokes shift.

Raman spectroscopy has become a powerful tool with widespread use across the sciences and has become the de facto choice for any situation where non-destructive, microscopic, chemical analysis and imaging is required as it allows for interrogation and identification of a material's constituent molecules and of their vibrational states [39]. A key benefit to Raman spectroscopy over other chemical analysis techniques is that Raman spectroscopy does not require sample preparation and Raman scattering can occur regardless of incident wavelength. Likewise, there are often

[2]The Raman scattering effect is sometimes referred to as the Smekal-Raman-Effekt in German literature, as Austrian Physicist Adolf Smekal predicted inelastic scattering of light in 1923 [36]. and was also reported by Grigory Landsberg and Leonid Mandelstam in February 1928, thus in Russian scientific literature the effect is usually referred to as *combination scattering* [37, 38]

clearly defined peak locations or "Raman lines" that correspond to energies of certain vibrational modes of the material. Patterns of such lines often form clear spectroscopic fingerprints for certain substances. These spectra are very specific and chemical identifications can be performed by comparison against digital databases. Furthermore, since the emission band areas are proportional to molecular concentrations, Raman spectra can be used for quantitative analysis of chemical compositions.

Finally, for practical application purposes, it is worth noting that even though the peak locations from the Stokes and anti-Stokes frequency shifts should be symmetric about the Rayleigh peak, their intensities usually differ. The anti-Stokes peaks of Raman spectra are generally much weaker than those of the Stokes peaks as there are many more molecules at ground state energy levels than at (typically thermally) excited states. Likewise, this ratio between the populations of ground and excited states is temperature dependent and can be exploited in specific cases to provide an additional utility in the form of temperature measurements [40]. A fundamental difference between the Raman scattering phenomenon and that of fluorescence emission where a photon is absorbed and then one of longer wavelength is re-emitted, is that Raman scattering occurs due to a modulation-type scatter as described by the previously discussed induced dipole section starting with Eq. (2.4) and can occur independent of wavelength, even far from the absorption band of molecules.

The only Raman spectroscopy method focused on in this dissertation is that of spontaneous Raman spectroscopy; however, there are now more than two dozen types of Raman spectroscopy techniques such as stimulated Raman, coherent anti-Stokes Raman scatter-ing (CARS), surface-enhanced Raman scattering (SERS) and tip-enhanced Raman scattering (TERS) to name a few. Despite Raman spectroscopy being a well established technique with both its applications and theory extensively explored and reviewed, its potential for broad scale use in biomedical applications has only just been realized in the past few decades.

2.2.2 Brillouin scattering and spectroscopy [‡]

Brillouin scattering, named after Léon Brillouin the French Physicist credited as the first person to have predicted the phenomenon in 1922 [41][4], is the mechanical parallel to the chemical-based Raman scattering. Where Raman scattering and spectroscopy can provide information about the chemical properties and structures of a material, Brillouin scattering can provide information about a material's mechanical vibrations and properties.

Like Raman scattering, Brillouin scattering involves inelastic processes between photons and vibrations within a target material. In fact, the general principles underlying the energy exchange in Brillouin scattering very closely match those of the previously described Raman scattering except that Brillouin scattering is based on photon energy exchange with (generally thermally-induced) periodic spatial and temporal density (and thus refractive index) fluctuations in the material. These types of vibrations are referred to as acoustic phonons. The resultant frequency of the inelastic scattered light, after the photon-phonon interaction, is again shifted by one of two processes: the creation and emission (Stokes process) or the absorption and annihilation (Anti-Stokes process) of a phonon. Again, the energy conservation law dictates that the change in photon energy, and, thus, the shift in frequency, must come from the angular momentum of the phonons. The shifted frequency can again be described in the familiar from $\nu_s = \nu_i \pm \nu_B$ where, in this case, ν_B represents the phonon frequency or what will often be referred to later as the "Brillouin frequency shift". The change in frequency as indicated by the '$\pm$' represents the respective Stokes and anti-Stokes frequency shifts, dependent on the propagation direction of the phonon. When trying to discern the value that these measurements provide, one may consider the propagation of an acoustic wave through a medium: as the mechanical properties of a material govern how acoustic waves propagate

[‡]The notation in this chapter for Brillouin frequency shift and measurement follow guidelines proposed during a recent BioBrillouin workshop for unified reporting of Brillouin spectroscopy measurements. Further detail can be found in Appendix B.

[4]This scattering phenomenon is also sometimes referred to as Brillouin-Mandelstam scattering - most commonly in Russian literature. This discrepancy in naming originates from the description provided by Brillouin in his first publication, which was technically a description of light scattering from two counter-propagating waves akin to what might happen during *impulsive stimulated* Brillouin scattering events. Additionally, Mandelshtam first described *spontaneous* Brillouin scattering from spontaneous and dissipating fluctuations in a medium in his doctoral thesis, in 1918, though he did not publish results until 1926 [42].

through them, the light scattered off of these waves (the Brillouin scattered light) carries with it information about those specific mechanical properties.

The magnitude of the Brillouin frequency shift in scattered light depends on the incident wavelength, the sample material or medium composition, the temperature, and pressure of the medium. Thus, the information that can be obtained from measuring the Brillouin frequency shift includes the speed of sound, adiabatic compressibility, and the longitudinal modulus of a sample. While the frequency and spectral location of Brillouin shifts can provide critical information, the linewidth of the Brillouin peaks can also be used to fully describe the viscous properties through association with the acoustic attenuation coefficient and the loss modulus of a sample.

Finally, where Raman frequencies are generally in the THz range, Brillouin frequency shifts are orders of magnitude smaller often between 1 - 10 GHz. Brillouin scattering can also occur through interactions with magnetic modes (magnons, spin waves) [43, 44], however that is outside the scope of this dissertation and will not be addressed in detail.

Table 2.1 provides a brief overview of the differences between Raman and Brillouin spectroscopy. Figure 2.2 provides an example plot for visualization and comparison of Raman and Brillouin spectra and their respective differences in frequency shift, alongside a centralized elastic scattered Rayleigh peak.

Brillouin spectroscopy has recently seen rapid development of both instrumental design and technique application. With these new advances, Brillouin spectroscopy has become another powerful spectroscopy technique that takes advantage of inelastic scattering of light. The following sections are dedicated to the interpretation of Brillouin spectra and the underlying physical principles behind it. The discussion provides focus on defining the frequency shift and the peak linewidth and how those parameters relate to and help describe the mechanical properties of a material.

Table 2.1: Quick-reference comparison table for Raman and Brillouin spectroscopy. Though both processes rely on the inelastic scattering of light, the two processes produce scattered photons that carry different information from the target material and induce substantially different magnitudes frequency shifts, with Raman frequency shifts being orders of magnitude ($\sim 10^3$ to 10^4) larger than those of Brillouin frequency shifts.

Data Type	**Raman**	**Brillouin (ν_B)**
Information	Chemical	Mechano-elastic
Use	Widespread (past ~80 years)	Developing (~20 years development)
Time-scale	< 1 sec	> 1 min*
Typical shift (frequency)	100 – 4000 cm^{-1} (3 – 120 THz)	~1-10 GHz (0.03 – 0.3 cm^{-1})
Typical shift (wavelength)	~ 10 – 150 nm	~ 1 – 10 pm
Source of Contrast	Chemical bonds	Acoustic waves

2.3 Spectral Measurement and physical interpretation

2.3.1 Brillouin frequency shift

As discussed in the previous section, Brillouin scattering occurs when photons interact with acoustic vibrations in a target material and either lose energy (Stokes) or gain energy (anti-Stokes) through inelastic scattering processes. These new photons then carry with them information about the mechanical properties of the target material from which they have scattered. When considering the physical interpretation of the scattering, one can look at the acoustic waves as traveling at the adiabatic speed of sound in the material *V*. This is typically between ($10^3 - 10^4$ m/s), which is much lower than that of the incident photons, $c \approx 3 \times 10^8$ m/s. Therefore, these acoustic waves (local variations in density or refractive index) can be considered as quasi-static and act like a Bragg grating with periodicity Λ (the wavelength of the phonon). The way in which the light scatters in this condition is fairly simple to predict and the concept can be pictured as

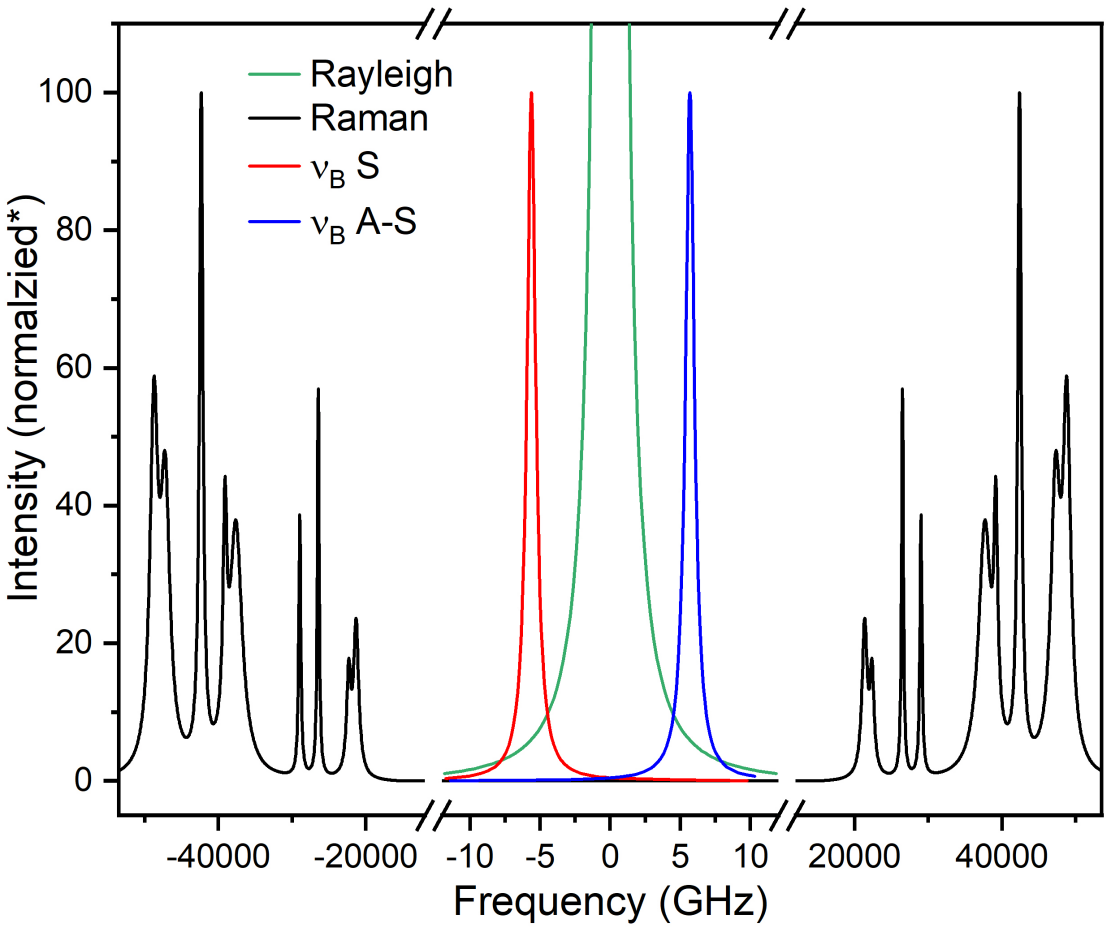

Figure 2.2: Example of spectra. Raman (black line) and Brillouin ν_B (red and blue lines) spectra with x-axis representing the magnitude of frequency shift from the central Rayleigh scattered peak (green). Peak intensities have been normalized to 100 with respect to their maximal intensity. This plot demonstrates the substantial difference in magnitude of the frequency shifts between Raman and Brillouin spectral peaks.

monochromatic electromagnetic wave, $\mathbf{E} = E_0 \cos(\omega_0 t - \mathbf{k} \cdot \mathbf{r})$ interacting with an elastic wave $\mathbf{A} = A_0 \cos(\nu_B t - \mathbf{q} \cdot \mathbf{r})$, where $\mathbf{k}$ and $\mathbf{q}$ are the wave vectors of the two waves, respectively, as pictured in Fig. 2.3.

If we consider an ideal case where photons interact with a purely elastic medium, the electromagnetic wave will be reflected by the different grating layers (wave fronts of the acoustic wave) at angle θ (the angle between the incident and scattered wave vectors). Constructive interference between the multiply reflected waves will occur when the difference between the path lengths is

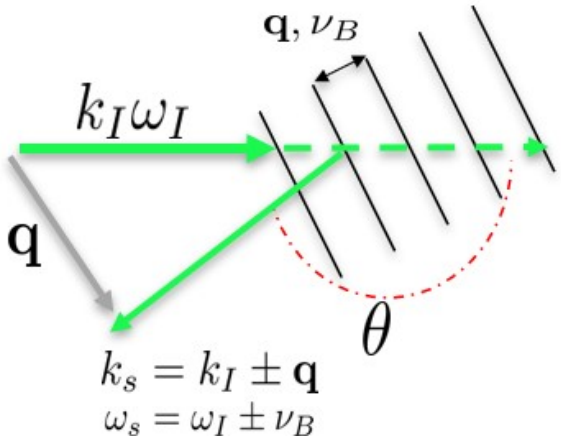

Figure 2.3: Schematic diagram of the Brillouin scattering and frequency shift process while treating the acoustic waves as a quasi-static Bragg grating. The direction of the phonon wave vector **q** is responsible for the reduced frequency of the scattered photons due to the Doppler effect. This image depicts the concept of a Stoke shift scattering event, but the equations present the case for both Stokes and anti-Stokes scattering outcomes.

equal to an integer multiple of the wavelength, i.e. constructive interference is maximized under the condition that:

$$2n\Lambda \sin(\theta/2) = \lambda \tag{2.7}$$

where λ is the wavelength of the incident light and Λ the wavelength of the acoustic wave. Since the scattering interaction process must obey the energy and momentum conservation laws, i.e. when the scattered photon has less energy than the incident photon, this must relate to the creation of a excitation in the scattering medium and vice-versa. If we note that the acoustic phonons that make up the elastic wave **A** travel through the medium at the adiabatic speed of sound, V with frequency $\nu_B \ll \omega_{s,I}$, the frequencies of the incident and scattered light, we can assume that the $\omega_s \approx \omega_i$ and that $k_s \approx k_i$. Each incidence of the Doppler frequency shifted emissions are then simply defined by:

$$\nu_B = \pm\frac{|\mathbf{q}|V}{2\pi} \quad or \quad \omega_B = \pm qV \tag{2.8}$$

where V is the adiabatic sound velocity in the medium and vector $|\mathbf{q}|$ the wave vector. In other words, the frequency shift is due to the creation or annihilation of a phonon as a function of

the momentum, or magnitude, of the wave vector. Therefore, the momentum exchanged in the scattering process:

$$q = 2nk_i sin\left(\frac{\theta}{2}\right) \tag{2.9}$$

with refractive index n, of the material and scattering angle θ, and wave vector k_i:

$$k_i = \frac{2\pi}{\lambda} \tag{2.10}$$

leads to the angular frequency of the shift:

$$\omega_B = \frac{\pm 4\pi n}{\lambda} V. \tag{2.11}$$

Noting the magnitude of the wave vector $|\mathbf{q}|$ [45]:

$$|\mathbf{q}| = \frac{4\pi n}{\lambda} sin\left(\frac{\theta}{2}\right) \tag{2.12}$$

we can combine the left side of Eq. 2.8 with Eq. 2.12 to extrapolate the frequency ν_B:

$$\nu_B = \frac{2n}{\lambda} V sin\left(\frac{\theta}{2}\right) \tag{2.13}$$

Equation 2.13 provides the magnitude of the frequency shifts for the Brillouin spectral peaks. From the simple sinusoidal relation, we can infer that when $\theta = 0^\circ$ the frequency shift is minimized to zero. Likewise, in a back scattering configuration when $\theta = 180^\circ$, ν_B is maximized:

$$\nu_B = \frac{2n}{\lambda} V \sin\left(\frac{\theta}{2}\right) \therefore \nu_{B,\theta=0}^{min} = 0, \nu_{B,\theta=\pi}^{max} = \frac{2n}{\lambda} V \tag{2.14}$$

2.3.2 Brillouin peak linewidth and the phonon lifetime

The lifetime of the phonon quasi-particle can be defined as given in equation 2.15 [46]:

$$\tau_p = \frac{\rho_0}{\eta q^2} = \frac{\rho_0 \lambda^2}{16\pi^2 \eta n^2 sin^2(\theta/2)} \tag{2.15}$$

where ρ and η are the density and viscosity of the medium, respectively. For a backscattering geometry in liquids, the lifetime has been found to be $\tau_p \approx 10^{-9}$ s [46]. It is possible to estimate the phonon propagation length in most liquids (where V is generally on the order of $\sim 10^3$ m/s) to be $\approx 1\mu m$. This propagation distance is on a scale larger than most microscopic materials, thus imposing a fundamental limit to the spatial resolution of Brillouin imaging and due to the photon-phonon interaction lengths [47, 48, 49].

The Brillouin peak linewidth Γ, determined as the full width at half maximum (FWHM) is given by:

$$\Gamma_{FWHM} = \frac{1}{2\pi\tau_p} = \frac{\alpha V}{\pi} \tag{2.16}$$

where α is the attenuation coefficient in the medium. Equation 2.16 shows that both $\alpha \propto \Gamma \propto 1/\tau_p$. If we define $\zeta = \eta/\rho$, which is referred to as the damping parameter, we can then find Γ in terms of the measured Brillouin frequency shift:

$$\Gamma_{FWHM} = \frac{1}{2\pi\tau_p} = \frac{\eta q^2}{2\pi\rho_0} = \frac{16\pi^2 \zeta n^2 sin^2(\theta/2)}{2\pi\lambda^2} = \frac{8\pi\zeta n^2 sin^2(\theta/2)}{\lambda^2} \tag{2.17}$$

the final product of which looks to hold similarity to $\nu_B^2 = 4n^2 V^2 sin^2(\theta/2)/\lambda^2$, simply without the velocity term. We can therefore substitute in ν_B and write:

$$\Gamma_{FWHM} = \frac{2\pi\zeta\nu_B^2}{V^2} \tag{2.18}$$

which can then be related back to equation 2.15 through:

$$\Gamma_{FWHM} = \frac{\alpha V}{\pi} \tag{2.19}$$

so that we can define the attenuation coefficient in terms of the Brillouin frequency shift as:

$$\alpha = \frac{2\zeta\nu_B^2}{V} \tag{2.20}$$

We can, therefore, given specific information such as ρ and η use the measurements from the Brillouin spectra to determine several of a materials physical parameters, and vice versa. Likewise, the linewidth of the Brillouin spectra can provide information about the thermal relaxation processes and sound absorption and attenuation of the medium. This leads to the next section, where we discuss the physical interpretation of these measurements.

2.3.3 Elasticity and the complex longitudinal modulus

As the mechanical properties of the material govern how the acoustic wave propagates through the medium, the Brillouin scattered light carries with it information about those mechanical properties. The peak position and linewidth on a spectrometer, i.e. the magnitude of the Brillouin frequency shift and corrected full-width at half-maximum of the Brillouin peak allows one to probe the complex longitudinal modulus through the following relationships:

$$M = M' + iM'' = \rho V^2 + i(2\rho V^3\alpha/\omega) \tag{2.21}$$

where ω is the angular velocity of the shift. The real part *M'*:

$$M' = \rho V^2 \tag{2.22}$$

is the longitudinal bulk modulus or the elastic *storage modulus M'* and describes the elastic response of the probed material.

The complex part *M"*:

$$M'' = 2\rho V^3 \alpha/\omega = \frac{\rho V^3 \alpha}{\pi \nu_B} \tag{2.23}$$

is the loss modulus, and describes the viscous response of viscoelastic materials. Recalling from Eq. 2.13 that in a 180° back scattering arrangement, $\nu_B = 2nV/\lambda$, M' can be determined as:

$$M' = \rho V^2 = \rho \left(\frac{\lambda \nu_B}{2n} \right)^2 \tag{2.24}$$

which gives an analytical expression for determining the longitudinal storage modulus from the Brillouin frequency shift. The complex modulus determined through this method would, in theory, be the same as that obtained by hypothetical dynamic mechanical analysis at the GHz frequency range [50]. Additionally, one may note from Eq. 2.24 that there exists a relationship between the hyperspeed velocity in the medium *V* and both the mass density and storage modulus M'; i.e. $V = \sqrt{\frac{M'}{\rho}}$. Therefore, if the mass density and refractive index of the material are known, determining the speed of sound *V* from the measured Brillouin frequency shift ν_B is simple.

The Brillouin shift can then be expressed as:

$$\nu_B = \frac{2n}{\lambda} \sqrt{\frac{M'}{\rho}} \sin \frac{\theta}{2} \tag{2.25}$$

where as usual, n and ρ are the refractive index and mass density of the material, λ the wavelength of incident light, and θ is the collection angle for the scattered light collection angle (180°for all measurements reported within this manuscript). One may also note that the square root may be used specifically for finding the modulus: $M' = \rho V^2$. This is what is often referred to as the "Brillouin Modulus". The Brillouin modulus can also be expressed in terms that include the Bulk and Shear moduli *K* and *G*:[5]

$$M' = K + \frac{4}{3} G \tag{2.26}$$

[5]A note regarding the relationship between M, K, and E; See Appendix B

Which is then related to the more familiar Young's Modulus, E:

$$K = \frac{E}{3(1-2\sigma)} \tag{2.27}$$

where σ is Poisson's ratio that defines material compressability. Analysis by Scarcelli, et al. empirically determined a log-log linear relationship between Brillouin and quasi-static Youngs moduli, [51] which can be expressed as:

$$\log(M') = a\log(E) + b \tag{2.28}$$

where a and b are arbitrary coefficients.

2.4 Brillouin spectroscopy: history of developments and biological applications

Brillouin scattering was theoretically described and then experimentally demonstrated nearly a century ago, at roughly the same time as Raman scattering [41, 52]. The advent of the laser brought with it a renewed interest in optical spectroscopy, resulting in hundreds of studies; Brillouin spectroscopy became the single-most frequently used technique for crystalline property measurements in materials sciences, condensed matter, and geophysics [53, 54]. Despite the surge of interest, Brillouin spectroscopy applications were still quite limited. The very weak and small frequency shifts that occur with Brillouin scattering are difficult to measure and require an extremely high resolving power ($\mathcal{R} = \lambda/\Delta\lambda \sim 10^6$). Standard spectrometers cannot easily achieve this level of resolving power [55, 56]; therefore, applications of Brillouin spectroscopy have been limited, making it and under developed and under represented in literature when compared to its chemical counterpart. Furthermore, the overall accessibility and applicability of Brillouin spectroscopy investigations has been limited by a lack of available commercial systems; until two years ago, TFPI were the only high-contrast systems commercially available for Brillouin spectroscopy investigations. Advances in lasers, optics, and optical sensing devices have enabled several developments in Brillouin instrumentation that included unique wavelength dependent angular dispersion-type optics and initiated a phase of rapid development starting in 2005 that has continued through today

[57, 50, 58, 59].

2.4.1 Development

Two critical challenges exist for Brillouin spectroscopy. The first is that Brillouin scattered light experiences such small frequency shifts that it is generally indistinguishable from elastically scattered Rayleigh light and incident noise. Second, Brillouin scattering is a weak process with small cross section area. High spectral contrast (or extinction) must be achieved to separate the nearby frequency-shifted Brillouin light from the much stronger elastically scattered Rayleigh light and high sensitivity detectors must be used to detect the weak Brillouin signal.

Scanning the optical cavity of high finesse Fabry-Perot interferometers (FPI) has been the most popular method for performing Brillouin spectroscopy. Conventional Fabry-Perot interferometers, however, do not achieve the contrast needed to easily resolve the weak Brillouin doublets. In 1970, Sandercock introduced a scanning multi-pass tandem Fabry-Perot interferometer (TFPI) arrangement to improve signal contrast, signal-to-noise ratio (SNR), and free spectral range (FSR) [60]. Even though the TFPI arrangement introduced by Sandercock provided for substantial advancements in capabilities, TFPI typically require very long signal acquisition times ranging from minutes to even hours due to their point-sampling and scanning methodology [61, 62]. Brillouin spectroscopy applications were mostly limited to transparent condensed matter such as crystals, polymers, and liquids [63].

The first significant advances to Brillouin spectroscopy since the 1970s came with the development of new high-sensitivity multichannel area-detectors or, specifically, improved charge-coupled device (CCD) cameras used in conjunction with static, nonscanning, angle-dispersive FabryPerot interferometers [64, 65]. Combining area detection sensors with static FPIs allowed for more rapid measurements of Brillouin spectra by eliminating the necessity for cavity scanning and allowing for single-shot acquisition of entire spectra and the first demonstrations of Brillouin imaging. This development allowed for the first transition from point-scanning spectroscopy toward Brillouin spectroscopic imaging, as first performed by acquiring spectra across a liquid interface by Koski and Yarger in 2005 [57]. The introduction of a novel Fabry-Perot type etalon, known as the Vir-

tually Imaged Phase Array (VIPA)[66, 67, 67], discussed in greater detail in Chapter 3, helped to further improve the spectral resolution and efficiency of static non-scanning techniques. The VIPA etalon allows the Brillouin spectral peaks (mostly limited to transparent samples such as liquids) to be localized and resolved from the central Rayleigh signal. Unfortunately, the VIPA etalons do still suffer from low extinction of the dominating Rayleigh signal [50], limiting their overall application potential without additional enhancement. Scarcelli and Yun explored multi-stage, or tandem VIPA etalon arrangements in an attempt to resolve this issue. They found that two and three stage VIPA systems could achieve an extinction ratio of 55 dB and 80 dB, respectively [68]. Despite the impressive extinction ratio of the three stage system, it only provides for a maximum throughput efficiency of 7%, which makes it unsuitable for detecting low intensity Brillouin scattered signal. Though multi-stage VIPA arrangements do help to reduce the background and Rayleigh signal, the loss in efficiency is often not worth the trade-off, particularly those with more than two VIPA etalons.

An ideal spectrometer configuration is one that employs a single VIPA etalon yet still achieves high spectral contrast. Such a system requires alternative methods for removing or suppressing the dominant Rayleigh signal. Several approaches have been taken to achieve this. In 2014 Meng, et al. combined a single-stage VIPA spectrometer with a molecular absorption cell, following previous work presented by Horoyski and Thewalt in 1994 [69]. The molecular absorption cell provided elastic signal suppression and enhanced contrast by more than 50 dB in Brillouin spectra acquired from highly scattering samples [70]. The following year, Antonacci, et al. utilized a Michelson interferometer type arrangement to take advantage of destructive interference for elastic signal suppression in both single and double-stage VIPA spectrometers, achieving an additional enhancement in spectral contrast by 36.4 dB [71]. Antonacci, et al. contributed further in 2017, demonstrating dark-field Brillouin microscopy, using annular illumination and confocal detection, reporting an extinction ratio of 30 dB. That same year, Edrei, et al. adapted coronagraphy techniques typically used for exosolar planet imaging and integrated it with a double-stage VIPA spectrometer, achieving an increase of 20 dB with nearly no additional insertion losses [72]. Finally, in 2018,

Antonacci, et al. presented findings on a background deflection technique that makes use of a simple diffraction mask at the VIPA output to achieve greater than 40dB enhancement. Additional efforts have also been made to increase the overall signal strength and resolution limits inherent to Brillouin spectroscopy. A notable report published by Edrei and Scarcelli in 2018 addressed the potential for adaptive optics to correct for aberrations and improve spectral precision and resolution in Brillouin spectrometers [73]. The method used for all experiments related to this dissertation is that of both Iodine and Rubidium molecular absorption filters, depending on wavelength combined with a single VIPA etalon. Details regarding the experimental design of our custom spectrometer is provided in Chapter 3.

2.4.2 Biological applications

The first reports demonstrating Brillouin spectroscopy applied to biologically-relevant material date back to the 1970's when Bedborough and Jackson reported a study of gelatin gel in 1976 [74]; Cusack and Miller also presented a similar study in 1979 [75]. The first applications of Brillouin spectroscopy to biological material were reported at roughly the same time. Harley, et al. reported measuring the elastic moduli of collagen and molluscan muscle in 1977 [76], and Randall, Vaughan, and Cusack presented the first look at Brillouin measurements from rat tail collagen and horsehair keratin in 1979 [77]. Vaughan and Randall then provided measurements of the elastic properties and refractive tissue densities in the eyes of multiple vertebrate species including measurement of the cornea, capsule, and lens [61]. The demonstrated successes of Brillouin measurements from biological tissues were limited, however, as signal acquisition times were too long for any living or dynamic biological systems. Despite this limitation, many impressive studies were conducted in the following years, including investigations on lipid samples, DNA fibers, lysozyme solutions, muscle fibers, and collagen-based biopolymers and fibers [78, 79, 80, 81, 82, 83].

The introduction of static dispersion optics like the static FPI and VIPA with their accompanying $>$100-fold reduction in signal acquisition times combined with various elastic scattering suppression methods led to new innovations and applications, and the beginning of a Brillouin-renaissance in 2005 [84]. Since then, Brillouin spectroscopy has become a powerful tool for sens-

ing and imaging, finding use in myriad applications from materials and nanoscience [85, 86, 87] to remote sensing [88, 89] and most important to our primary interest, biomedical imaging [84, 90, 91].

The custom Brillouin spectrometers used today are capable of high (~ 1 μm) spatial and spectral ($<$ GHz) resolution, and enable what is referred to as Brillouin Microspectroscopy systems (or micro-Brillouin Light Spectroscopy) capable of measuring spectra from microscale biological materials with sub-second acquisition times. The first application of modern Brillouin spectrometers to biology came in 2007, when Scarcelli and Yun presented the first *in situ* biomechanical measurement of the crystalline lens in a mouse eye. Since then, these researchers have continued their work in ocular biomechanics, demonstrating Brillouin spectroscopy and imaging for a variety of eye-based measurements, including two and three dimensional Brillouin imaging studies, and the first *in vivo* clinical investigation with human subjects in 2012 [92, 50, 93, 94, 95].

2.5 Brillouin spectroscopy: state-of-the-art

Brillouin spectroscopy and imaging efforts of the past decade have offered insights into the role of biomechanics in a variety of biological processes at the tissue, cellular, and even subcellular levels. The following sections review some of the most recent achievements and demonstrations of Brillouin spectroscopy's unbound potential for biologic and clinical applications.

2.5.1 Investigations at the macro scale: tissues and bio-fluids

Changes in the mechanical properties of biological tissue is often indicative of disease pathogenesis [96, 97]. Recent studies have demonstrated Brillouin microscopy as a viable tool for measuring the mechanical properties of tissues such as muscle, heart, and brain tissue. For example, a 2017 report by Mattana, et al. demonstrated Brillouin spectral analysis of the micromechanics and viscoelasticity of Aβ plaques, and provided correlative Raman analysis of the plaques to demonstrate chemical specificity in identifying the molecules responsible for the mechanical property changes. They then related high rigidity to the Aβ plaque core and indicated low rigidity within a surrounding the lipid ring. Damage or trauma to the brain parenchyma often results in a loss of

cognitive ability, and a buildup of amyloid plaques in the parenchyma is regarded as the leading underlying cause of Alzheimer's disease [98].

Fukui, et al. used Brillouin microspectroscopy to characterize the mechanical properties of cortical bone from a cow femur, estimating the hypersonic sound velocity relation with hydroxyapatite content and showed that decalcification caused a significant decrease in sound velocity, thus reducing stiffness [99]. Matsukawa, et al. performed a similar study using bovine and cortical trabecular bone [100].

A study by Troyanova, et al. evaluated the effect of a high-fat diet on the chemical and mechanical properties of adipose tissue in mice, using a correlative Brillouin-Raman spectral analysis [101]. Their results indicated that high-fat diet can lead to increased stiffness and lipid concentration in both white and brown adipose tissue, and an overall reduction in structural heterogeneity of both the brown and white adipose tissue. These results provide insight into how adipose tissue changes both mechanically and chemically, with high-fat diet and obesity. Another report produced by Troyanova, et al. in 2019 demonstrated the potential of Brillouin spectroscopy toward clinical diagnosis of melanoma showing differences in properties between healthy skin and that of both regressing and non-regressing melanoma [102]. Troyanova, et al. continued their adipose tissue investigations further, investigating impact of prolonged antihistamine use on the same type adipose tissue samples. They reported prolonged intake of desloratadine lead to an increase in Brillouin shift in both adipose tissue types. Raman spectra indicate that antihistamine use reduces protein-to-lipid ratio in brown adipose tissue but not white adipose tissue, indicating the effect on adipose tissue is location-dependent [103].

Esophageal tissue properties exhibit change in patients with symptoms of Barrett's esophagus. This disease occurs when the cells lining the esophagus become damaged and then develop abnormally resulting in dysplasia, a pre-cancerous condition that can lead to esophageal cancer if left untreated. In 2016, Palombo, et al. generated chemico-mechanical maps of Barrett's esophagus epithelial metaplasia using both Raman, Brillouin, and Fourier-transform infrared (FTIR) spectral imaging, and proposed the future development of Brillouin endoscopy techniques for clinical and

diagnostic applications.

In 2015, Steelman, et al. published a report demonstrating Brillouin spectroscopy as a novel method for screening of increased protein levels in patients with bacterial meningitis, using a cerebral spinal fluid (CSF) model [104]. Traditionally, the diagnosis of bacterial meningitis is difficult and can slow (>24 hours), when early detection and treatment is of utmost importance for successful treatment and patient survival. This report indicated that increased protein concentrations present in the CSF during bacterial meningitis can be measured by Brillouin spectroscopy, providing the possibility of a rapid, efficient, and nondestructive approach to screening for the disease.

As optically clear samples are ideal for spectroscopic investigations, tissue clearning techniques are often used to reduce the opacity of biological tissues through lipid removal. Tissue clearing helps to reduce optical scattering and enhance light penetration depth for relevant light-based studies. As lipid removal and tissue clearing processes modify the optical properties of the sample, there exists the concern of tissue mechanical property changes as well. Riobóo et al. sought to resolve the concern by measuring Brillouin frequency shifts and hypersonic attenuation from mice myocardium after tissue clearing [105]. Their results indicated that the tissue clearing methods they used did not change the values obtained using Brillouin spectroscopy (magnitude of Brillouin frequency shift and peak linewidth), but did serve to enhance reliability of spectral measurements.

Last, Margueritat, et al. demonstrated Brillouin imaging and measurement discrimination between healthy tissues and those with altered tumorigenic properties. They produced mechanical maps and longitudinal modulus measurements from tumor colorectal carcinoma cell line spheroid models (SW480 and HCT116) [106]. Furthermore, they propose Brillouin modulus as an indicator for monitoring drug efficacy, showing that the modulus is unevenly altered across sphereoids treated with 5-fluorouracil drug therapy revealing a lag of efficacy in the tumor core.

2.5.2 Investigating organism growth and development

The previous subsection presented tissue-level studies that illustrate the potential for Brillouin technologies to bring new insights to medicine and pharmacology. However, recent studies have

shown Brillouin microscopy to be capable addressing a key focus in developmental biology. The use of Brillouin microscopy combined with other optical techniques has provided researchers the opportunity to non-invasively measure and observe the mechanical properties and behaviors of tissues throughout physiological and developmental processes. For example, a 2018 report by Schlüßler, et al. provided spinal cord tissue images acquired using Brillouin microscopy. Their report included measurements of longitudinal modulus, elasticity, and viscosity from zebrafish larvae tissue both during embryonic development and spinal cord regeneration after damage [107]. They also found that the pathological and developmental processes observed had respective changes, as measured by Brillouin frequency shifts. This work by Schlüßler, et al. proved Brillouin microscopy capable of mechanical property mapping of distinct anatomical structures without interfering with the natural processes of an organism. Their report provided the first Brillouin microscopy images of spinal cord tissue, and indicated the necessity of *in situ* measurement capabilities for biomedical and clinical applications, pointing to differences found between *in vivo* and *ex vivo* type measurements.

Raghunathan, et al. combined Brillouin microscopy with optical coherence tomography (OCT) to measure stiffness distributions of developing murine embryos. This combination of technology provided visual identification of specific structures (OCT) for targeted imaging or mechanical mapping of individual organs (Brillouin microscopy) [108]. Zhang, et al. also used this same combination in 2019 to generate maps of cranial neural tube closure during embryogenesis [109]. They found the modulus of tissue varied distinctly within the neural tube region of embryos at different stages of development and that the tissue stiffens significantly after the neural tube fully closes. Further demonstrating the capability of Brillouin microscopy for tissue-level imaging applications during embryonic development.

2.5.3 Microscale investigations using Brillouin microscopy [6]

Though the mechanical properties of organs and tissues are increasingly recognized as important factors in developmental and pathological phenomena, a complete understanding of these organ-level behaviors can only be obtained by tracing them back to events at the cellular level. The following subsection reviews some of the most recent applications of Brillouin spectroscopy and imaging for examining the fundamental concepts of biomechanics at the cellular and subcellular-levels.

2.5.3.1 Investigations at the cellular level

Brillouin spectroscopy's contact-free nature has led to its adaptation into confocal microscope arrangements, enabling single-cell and even subcellular organelle-level imaging. Scarcelli, et al. reported the first Brillouin-based mechanical maps of cells in 2015 [110], presenting two dimensional images and z-stack series from NIH/3T3 fibroblast cells in 2D and 3D collagen gel cultures. Additionally, they reported two interesting measurements: an increase in magnitude of Brillouin frequency shift measured from cells after hyperosmotic shock, and ten minute time series of relative Brillouin frequency shift measurements from cells during actin polymerization into the culture gels. They observed that rigid substrate environments influence cell stiffness and they observed a relationship between cell stiffness measurement and cell spreading areas. That same year, Meng, et al. demonstrated lateral scanning of regular and FITC-functionalized red blood cells. Intracellular elasticity fluctuations were identified across cell bodies, with greater Brillouin frequency shifts measured along cell edges than those from cell centers. The Brillouin shifts correlated with the presence of hemoglobin toward cell edges, as indicated by concurrently acquired Raman spectra. The functionalization process removed $\sim$95% of the hemoglobin from the cells, thereby altering their composition and morphology. The functionalization process led to a differences in both average Brillouin frequency shift and linewidth measurements, $\sim$300 MHz lower in the functionalized

[6] An example of a two-dimensional mechanical mapping of CHO-K1 cells is provided in Chapter 4 of this dissertation; the structural inhomogeneities within the cell and between different cell structures can be distinguished and characterized through contrasts in the magnitude of the measured Brillouin frequency shift.

cells compared to normal cells, while the functionalized cells also exhibited a slightly increased viscosity. These results indicate that the presence of hemoglobin in red blood cells likely contributes to the mechanical stability and overall rigidity of the cells.

2.5.3.2 Investigations at the subcellular level

Below the whole-cell level, subcellular structures exhibit different properties than that of their surrounding environment and organelles. The first high-resolution subcellular measurements and images were presented in 2016 by Antonacci and Braakman [111]. Their report demonstrated Brillouin microscopy as a viable tool for subcellular measurements and imaging by comparing healthy endothelial cells against cells exposed to latrunculin, a chemical toxin that prevents actin polymerization and causes an overall decrease in cell stiffness. Following the 2016 report, Antonacci, et al. published a background deflection technique for spectral enhancement by which they measured the mechanical properties of intracellular stress granules in fixed HeLa cells and their changes in response to mutant protein associated with development of amyotrophic lateral sclerosis (ALS)[112]. A 2018 report by Mattana, et al. provided single cell Raman and Brillouin analysis that showed induced tumoral fibroblasts (NIH/3T3 cell line) have a decreased nuclear elastic modulus, which was then related to the increased capacity of cancer cells to squeeze through narrow passages and migrate [49]. The results in their report were presented alongside an often overlooked consideration from high resolution spectral measurements and mapping: the fundamental spatial resolution limit of Brillouin microscopy itself. There exists a fundamental spatial barrier by which Brillouin spectroscopy is limited. This limit ~ 1 μm, and is due to the relative length-scales of acoustic phonon wavelengths, material scattering volumes and barriers, subcellular structure sizes, and the optical collection volume of the collection optics. Phonon path lengths, and structure sizes in complex inhomogeneous materials determine a fundamental limit for the spatial resolution in Brillouin spectroscopy, apart from the diffraction limit and Rayleigh criterion. Depending on the relative size of the component structures in relation to the acoustic phonon wavelength, individual components within the focal volume may present a unique, average, or sum of their spectra [90].

Finally, in 2020, Zhang, et al. reported *in vitro* Brillouin microscopy measurements and 3D

chemomechanical modeling of cell nuclei following targeted disruptions of cytoskeletal and nuclear structures. Their results indicate that the cell nuclear modulus is strongly regulated by both internal nuclear nanostructures (lamin and chromatin) and cytoskeletal behavior. Their results demonstrated that actin network depolymerization leads to a reduced nuclear modulus in NIH/3T3 cells, while disruption of the microtubule network leads to a greater nuclear modulus.

2.6 Summary and conclusion

Microscopy and imaging tools based on Brillouin technology have the potential to bring new insights to the fields of mechanobiology and clinical diagnostics. This chapter introduced the fundamental concepts needed to understand Raman and Brillouin spectroscopy, with a historical overview of both Brillouin instrumentation and its transition to a modern imaging modality. Examples from state-of-the-art Brillouin investigations are provided that demonstrate the unbarred potential of Brillouin spectroscopy toward various biomedical and clinical applications. The following chapter introduces the static-dispersion optic that has enabled the development of modern non-scanning Brillouin spectrometers and provides an assessment of a VIPA-based spectrometer design and of what has previously been viewed as the golden standard of Brillouin investigations: a multi-pass tandem Fabry-Perot interferometer.

3. MODERN BRILLOUIN SPECTROSCOPY AND INSTRUMENTATION*

One of the greatest challenges in Brillouin spectroscopy and imaging is that of how to resolve or isolate the inelastic scattered Brillouin signals from that of the elastically scattered signal. With highly scattering samples such as biological tissues, or with samples of high turbidity, the elastic scattered Rayleigh signals can be orders of magnitude greater than that of the Brillouin scattered signals. Due to this extreme difference in signal strength, the elastically scattered signal can either saturate detection devices or completely dwarf and cover up the less intense inelastic scattering signals (the frequency shifts associated with Brillouin scattering are on the order of gigahertz, which is too small to resolve with conventional spectrometers). Additionally, there is an absolute necessity for high spectral resolution and rapid spectral acquisition times in order to make the technique feasible for a wide variety of applications.

High finesse Fabry-Perrot interferometers are the only commercially available high-contrast system for Brillouin spectroscopy experiments; however, conventional Fabry-Perot interferometers do not provide a high enough contrast to resolve Brillouin signals from the elastic backscattered signal, and as well, have very long signal acquisition times. In 1970 Sandercock used a tandem multi-pass interferometer arrangement to improve contrast, and thus signal resolution, as well as a means to increase the free spectral range (FSR), or distance between interference orders [60]. Since then, many new approaches have been proposed for improving Brillouin spectrometer designs from implementing different collection geometries, to notch filters, to sequential VIPAs [114, 70, 68, 115, 71, 116]. The history and advancements of Brillouin spectroscopy have been covered extensively [62, 84, 57], and a large number of reports are available on improvements for system optimization and spectral analysis [117, 118]. Likewise, reports covering the broad range of Brillouin applications in materials and nano-science, biomedical imaging [110, 104, 119, 101],

*Portions of this chapter are reprinted with permission from "Assessing performance of modern Brillouin spectrometers by Coker Z N, TroyanovaWood, M, Traverso, A J, Yakupov, T, Utegulov, Z N, Yakovlev, V V, 2018. Optics Express, 26, 3, 2400-2409, Copyright 2018 Optical Society of America under the terms of the OSA Open Access Publishing Agreement [113]

and multi-modal Brillouin systems [120, 121] are readily available.

3.1 Assessing performance of Brillouin spectrometers

In this chapter, we present a performance evaluation of three Brillouin spectrometers across a range of acquisition times. The spectrometers evaluated were a conventional scanning 6-pass tandem Fabry-Perot interferometer (TFPI) system with single photon counter, and two custom-built spectrometers using virtual imaged phase array (VIPA) dispersion optics and atomic absorption-based notch filters.

The purpose of this assessment was to provide a detailed look at the performance of two types of modern Brillouin spectrometers. Additionally, we present information critical to understanding how each spectrometer design (either static - dispersive VIPA-based design, or conventional commercially-available scanning TFPI) impacts performance and applicability to a wide range of potential investigations. Through characterizing our spectrometers, we set out to answer three fundamental questions: *"How accurate can our systems be?" "How long does it take for each system to achieve this level of accuracy?"* and *"Can we do better?"* By answering these questions, we not only evaluate our systems performance, but also develop a better understanding of how to further improve modern Brillouin spectrometer designs.

We have examined the accuracy and spectral resolution of Brillouin measurements acquired from acetone (a reliable, commonly-used calibration sample) from all three spectrometers, to evaluate each of their performances against a range of spectral acquisitions times. The result of each system analysis is presented alongside the others to allow the reader to easily examine the differences between each system design and its respective performance.

Ultimately, the two most important goals for modern Brillouin spectrometers is to offer sub-GHz spectral resolution and to achieve high accuracy in both Brillouin frequency shift (peak position) and Brillouin peak linewidth (FWHM) measurements. The sub-GHz resolution provides high spectral contrast between elastic-scattered Rayleigh signal, and the inelastic-scattered Brillouin signal, while high accuracy and precision of Brillouin frequency shift and linewidth measurements provides accurate information about the materials elastic modulus and viscoelastic proper-

ties. There is a strong focus on improving spectral contrast with the development of VIPA-based spectrometers.

Every new technique and design falls into one of only two established methods for high accuracy Brillouin measurements: scanning methods using scanning interferometers, and static or non-scanning angular dispersive etalon methods. Each new proposed design claims an advantage over others, but few researchers have presented how their system performance varies with time. Most Brillouin spectroscopy reports focus primarily on specific instrument application and use, often only providing data acquired under optimal conditions or very specific sample and exposure conditions. Such specific data might not be applicable across different fields or when studying different materials. Without a clear understanding of how the different types of modern spectrometers perform across a variety of acquisition times under the same conditions, researchers cannot make an informed decision about which spectrometer design best suits their needs.

3.1.1 Methods and materials for spectrometer assessments

The performance of three Brillouin spectrometers were analyzed in this assessment: a scanning 6-pass TFPI with a single photon counter shown in Fig. 3.1 and two custom-built VIPA-based spectrometers shown in Fig. 3.3. The schematic of the VIPA design depicts that of both the 780 nm and 532 nm VIPA-based systems. The primary difference between the two, aside from the differences in central wavelength is that the 532 nm system makes use of an I_2 filter whereas the 780 nm system uses ^{85}Rb. These two systems are otherwise identical. The theory and development of each of these designs has been covered in great detail previously [62, 84, 121, 60, 122, 123, 124, 50, 125], therefore only a brief description of each spectrometer cataloging the most important properties is provided in this section.

3.1.1.1 Tandem 6-pass Fabry-Perot interferometer (TFPI)

Brillouin spectroscopy became much more widely available in the 1970's after J.R. Sandercock developed the multi-pass Fabry-Perot Interferometer (FPI)[60]. This spectrometer design has been considered the standard for acquiring Brillouin spectra and is still the only commercially available

system today. A FPI is an etalon, consisting of two closely spaced partially reflective optical flats a distance (d) apart. Since the surfaces have high but not perfect reflectivity part of the light is transmitted each time the light reaches the second surface of the reflecting cavity. The resulting transmission is thus multiple projections of slightly offset beams which interfere with each other. The FPI acts as an optical resonator cavity. The reflections from the two surfaces then cancel each other such that photons can pass through the optical cavity only when they are in resonance with it. The angle of the FPI can then be adjusted to to control the resonance frequencies, and can therefore be used to treat the FPI as an adjustable optical filter, enabling extremely high resolution spectroscopic measurements. This can be further enhanced by using a multiple etalon arrangement.

The transmissions allowed from a FPI are given by

$$d = \frac{1}{2} n \lambda_t \tag{3.1}$$

where d is the flat separation distance, λ_t the wavelength of the transmitted photons, and n is simply an integer multiple. When two interferometers are used together, with differing flat separations, the conditions is such that:

$$\frac{2d_1}{n_1} = \frac{2d_2}{n_2} = \lambda_t \tag{3.2}$$

where again, d and n are separation distances and integer multiples. The transmission through multiple etalons serves as an additional filter to eliminate nearby peak orders and thus serves to expand the effective free spectral range of the spectrometer. TFPI plates are scanned by small displacements given by

$$\frac{\delta d_1}{\delta d_2} = \frac{d_1}{d_2} = \frac{\delta \lambda_t}{\lambda_t} \tag{3.3}$$

where δd_1 and δd_2 are the displacements of the individuals scanning plates of the first and second FP etalon, respectively.

When using two FP etalons, to ensure the scanning displacements δd_1 and δd_2 are moved in sync, they are arranged such that each of the two etalons have one of their plates, or flats, on a common translation stage which is scanned using a deformable parallelogram construction [60].

The corresponding FP plate separations $d_1 = d_2 = \cos(\theta)$, where θ is the angle between the optical axes of the two FP etalons. This arrangement is labeled as the "scanning stage" in Fig. 3.1.

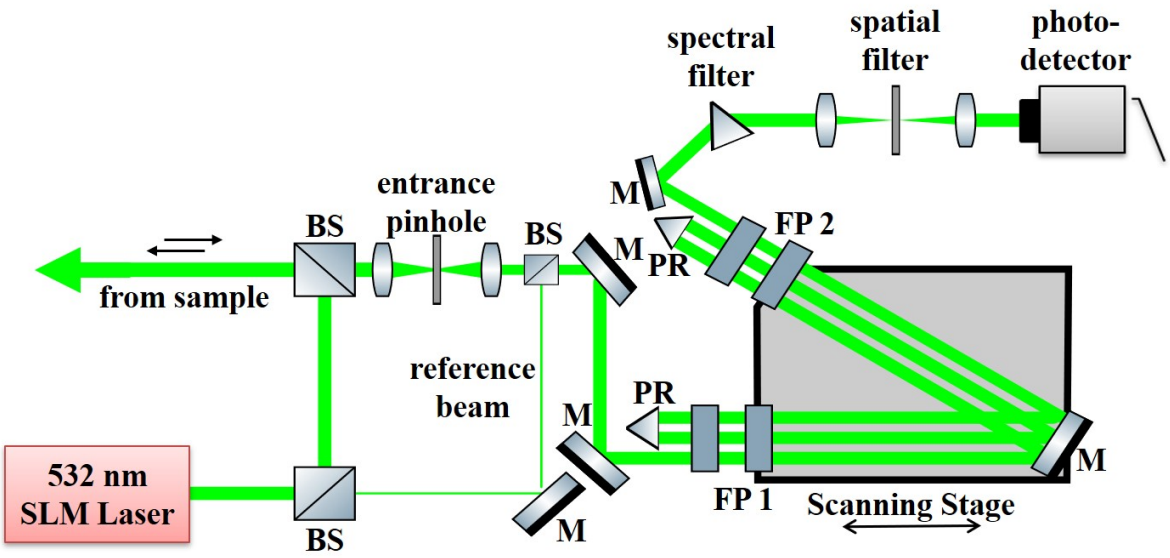

Figure 3.1: Schematic diagram of 6-pass tandem Fabry-Perot based micro-Brillouin spectrometer. Abbreviations: BS beamsplitter; PR prism, FP 1 & 2 Fabry-Perot cavity, M mirror.

The scanning 6-pass TFPI used for our assessment was equipped with a single photon counter and 1024-channel multichannel analyzer. This system was used to collect two separate data sets for assessment. Different scanning parameters and laser sources demonstrate measurement sensitivity dependence on laser stability and dispersion optics finesse ($\mathcal{F}$), or free spectral range (FSR). The first data set was acquired using a single longitudinal mode (SLM) laser with 532 nm wavelength (Torus 532, Laser Quantum). We set the total scan amplitude to 93.92 GHz, i.e. approximately twice that of the interferometers tuned FSR of 50 GHz, effectively scanning $\pm$ 49.96 GHz from incidence. The inter-channel frequency resolution, determined by the scan amplitude divided by the total number of channels, was 91.7 MHz. For the second data set, the excitation source was another SLM laser of wavelength 532 nm (Verdi G2, Coherent Inc) and we tuned TFPI for a total scan amplitude of 16.57 GHz and FSR of 8.285 GHz. The inter-channel frequency resolution for

the second data set was then 16.18 MHz. We used a 10x 0.25 NA microscope objective to focus the incident light, and to collect the Brillouin back-scattered light from the sample. Examples of each raw spectra and Lorentz fits from the TFPI and VIPA-based spectrometers are provided in the discussion on spectral acquisition and analysis.

3.1.1.2 The virtually imaged phase array (VIPA) dispersion optic

The key component of modern non-scanning spectrometers is the VIPA etalon, a depiction of which is provided in Fig. 3.2. A VIPA is a special type of Fabry-Perot etalon with parallel sides; one with a total reflective coating (R $>$ 99.9%) and one with a partially transmitting coating (R $\geq$ 95%). Light is typically introduced into the VIPA at a small angle (θ), through a small anti-reflective coated window on the totally reflecting side. The VIPA is then slightly tilted so that the beam reflected from the partially reflecting surface is fully incident on the totally reflective first VIPA surface. After the beam reflects for the first time (off of the second VIPA surface, i.e. the partially reflective surface), the beam undergoes sequential reflective round trips between each of the two surfaces. As one side of the VIPA is partially transmissive, a small portion of the beam is transmitted through this surface upon completion of each round-trip within the VIPA etalon. Therefore, a single input beam is converted to a series of parallel output beams of gradually decreasing intensity. This output is partially where the VIPAs name is derived, as the output is like that of multiple virtual sources. These beams then constructively interfere at an angle, dependent upon their wavelength. Each subsequent transmitted beam has a precise increase in phase and fixed lateral displacement and produces an array of projected beams, hence the name Virtually Imaged Phase Array. This wavelength dependent angular dispersion is what makes the VIPA etalon so desirable for Brillouin spectral acquisition, as it removes the need for the relatively slow scanning processes required by TFPIs.

The parameters that define the VIPA performance are its optical thickness, the reflectance of the output or partially transmissive side, and the internal light propagation angle. The optical thickness of a VIPA is determined as

$$D_O = 2nt\cos(\theta) \tag{3.4}$$

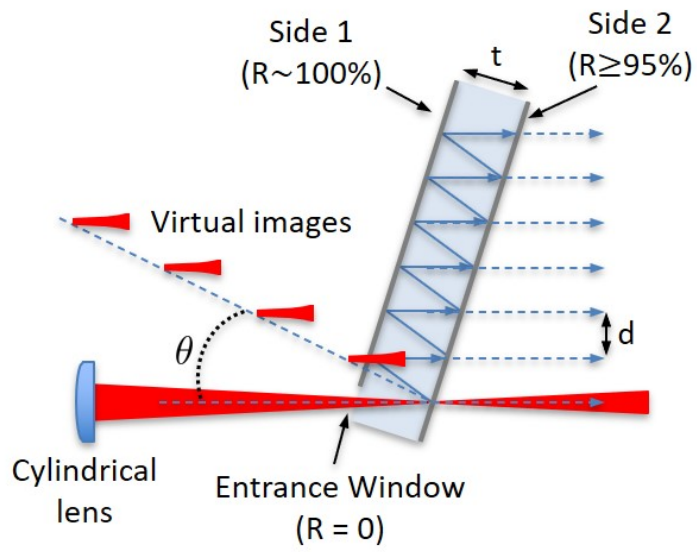

Figure 3.2: Basic diagram for a VIPA etalon as used in our custom spectrometer. The input beam is focused to the second VIPA surface ($\geq$ 95%) through the anti-reflective coated window with an incident angle θ. The beam then undergoes multiple reflections inside the cavity as in a normal FP etalon and is transmitted through toward an imaging lens and detector.

where n is the refractive index of the VIPA material, t is the thickness of the entire VIPA etalon, and θ is the angle from normal within the VIPA. From the optical thickness, the free spectral range (FSR) is approximately c/D_O, where c is the speed of light. For example, an etalon with thickness of 1 cm would have $FSR = c/0.01\ m = 29.98\ GHz$. The angular dispersion of the VIPA output will repeat every time the input frequency (or wavelength) increases by one full integer value of the VIPA FSR, exactly like that of a regular FP etalon. In principle, a higher surface mirror reflectance can be used to increase the total resolving power of VIPA etalons. In the ideal case, the partially reflective surface should be optimized for a specific wavelength range to maximize finesse. The finesse is measured as a ratio of the etalon FSR and transmission FWHM linewidths from a single mode, single-frequency input wave. A high finesse is ideal for optical spectral analysis, as it can provide for a large FSR, compared to a small bandwidth. A VIPA spectrometer with a finesse of 50 should therefore be able to distinguish wavelengths separated by 1/50th of the etalon FSR. An example of the FSR and linewidth measurements are provided in the discussion of spectral

analysis. The finesse can be approximated by the total number of round trip within the etalon through a simple relationship:

$$\mathcal{F} \simeq \pi N_{rt} \tag{3.5}$$

A final note regarding VIPA performance and design is that the angle normal to the VIPA surface dictates the angular dispersion of the output projections. A smaller incident angle can be used to increase the angular dispersion, but there is a physical lower limit this angle, as the first reflection from the second surface of the VIPA must be fully incident on the first surface, and thus the lateral offset of the reflected beam must be greater than the width of the input beam plus the width of the coating anti-reflective/reflective coating transition. This condition is generally met when the beam waist is located at the second (partially reflective) VIPA surface. For a more in-depth discussion on VIPA design and optimization, the reader is referred to Shirasakis description of the angular dispersion and filtering characteristics of VIPAs [66, 67, 123], and report on optimization procedures for signal collection of VIPA-based spectrometers by Meng and Yakovlev [126]. An excellently detailed discussion on optical cavities and resonators is also provided by Ismail, et al. in 2016 [127].

3.1.1.3 VIPA-based spectrometer with 780 nm wavelength

The first of the two VIPA-based Brillouin spectrometers was designed around an excitation source centered at 780.24 nm, with a single isotope ^{85}Rb absorption cell (Opthos Instruments, Inc.) acting as a narrow-band notch filter, a 10x 0.25 NA objective, and VIPA with FSR of 20.43 GHz. The VIPA had an anti-reflection coating optimal for the 780 nm wavelength and net finesse of approximately 40 (with roughly 84 round-trip passes to 1% intensity). The theoretical bandwidth at the output of the VIPA, based on the incident beam parameters and VIPA design was 0.45 GHz (Light Machinery, Inc.). A spherical lens focused the Brillouin spectra output from the VIPA onto a CMOS camera (Neo 5.5 sCMOS; Andor Technology, Inc.). Like the TFPI, two 780 nm laser sources were used to investigate the importance of laser stability on spectral resolution and overall sensitivity and accuracy of measurements. The first excitation source was an extended cavity diode

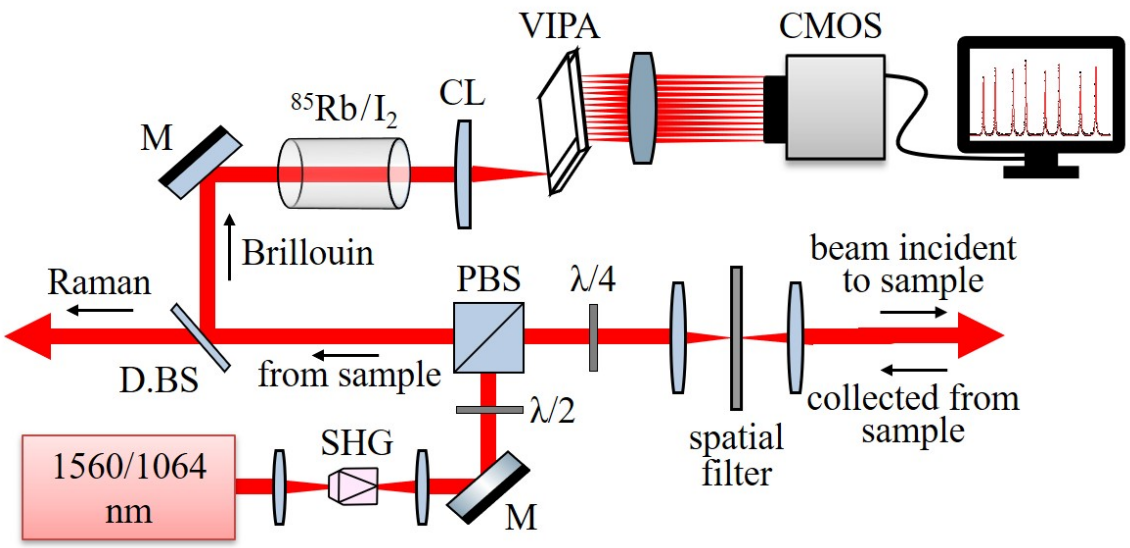

Figure 3.3: Schematic diagram of VIPA-based micro-Brillouin spectrometer, representative of both 780 nm and 532 nm spectrometer systems. Abbreviations: (P)BS (polarizing) beamsplitter; D.BS - dichroic beamsplitter, L lens, $^{85}Rb/I_2$ single-isotope rubidium, or Iodine-filled cell; CL cylindrical lens, M mirror, and CMOS - camera for spectral imaging.

laser (ECDL) centered at 780.24 nm with output power of ∼100 mW (Sacher Lasertechnik; Lion series). An electronic feedback loop and locking device controlled the piezoelectric transducer and thus the output wavelength of the laser. The second source was based on an integrable tunable laser assembly (iTLA) (PurePhotonics; PPCL300) tuned to a central wavelength of 1560.48nm and a MgO-doped PPLN second harmonic generation (SHG) crystal (MSHG1550-1.0-20; Covesion, Ltd) to generate an output wavelength of 780.24 nm with output power up to 100 mW. The SHG technologies and a fiber amplifier provided a very stable narrow-band, tunable excitation source, greatly simplifying the system.

3.1.1.4 VIPA-based spectrometer with 532 nm wavelength

The second VIPA-based Brillouin spectrometers was designed around a single-frequency laser (NKT Photonics.; Koheras BOOSTIK Y10) with 1064 nm center wavelength and 2 W maximum output power. We used a SHG crystal (MSGH1064-1.0-20; Covesion, Ltd.) to generate an output wavelength of 532 nm with output power up to 150 mW. Similar to the ^{85}Rb absorption cell

employed with the 780 nm spectrometer, an I_2 absorption cell (Opthos Instruments, Inc.) was used as the notch filter for the 532 nm VIPA-based spectrometer. The VIPA had an anti-reflection coating optimal for visible light wavelengths, and had FSR of 29.95 GHz, net finesse of 35 (with roughly 84 round trips to 1% intensity), and theoretical linewidth and spectral resolution of 0.86 GHz at VIPA output (Light Machinery, Inc.). Brillouin spectra were projected from the VIPA through a spherical lens onto a CCD camera (Newton 971; Andor Technology, Inc.). We note that the overall linewidth of the measured spectra is determined by three primary factors: the materials intrinsic linewidth for Brillouin peaks, dispersion relation and finesse of the VIPA, and spectral broadening/distortion effects caused by optical components (objective numerical aperture (NA), lenses, filters, etc.). The 532 nm VIPA-based system used a higher NA objective and VIPA with differing finesse than that of the 780 nm system, and thus we expect larger linewidth measurements. We used a 20x 0.4 NA microscope objective for this spectrometer, as opposed to the 10x 0.25NA objective used for the 780 nm spectrometer. The laser power at the sample for this spectrometer was set to 0.8 mW, a significantly lower power than the other spectrometers. This power level was chosen to avoid detector saturation at long acquisition times (greater than 10 s). While this incident laser power was acceptable for the longer acquisition times, it provided for poor resolution and low signal-noise ratio (SNR) at short acquisition times (less than 0.5 s). This power level was maintained for all spectra acquisition time to maintain uniformity throughout the experiment. Further discussion is provided in the Results section.

3.1.1.5 Sample selection and preparation

Acetone was selected as the sample material for spectrometer assessments. The Brillouin frequency shifts and viscoelastic properties of acetone are well known (speed of sound, viscosity, refractive index) [128]. Acetone has been used as a test sample in previous experiments [70] and is often used as a reliable calibration sample, and thus is optimal for characterizing the performance of these three spectrometers. Bulk samples were prepared in 20mL glass vials to avoid unwanted backscattered reflections from material boundaries, and all acetone samples were kept at room temperature with their respective spectrometer to ensure thermal equilibrium during mea-

surements. Room temperature was dependent on centralized building controls, and thus could not be accounted for during experiments. The change in ambient temperature resulted in some discrepancies at very-long acquisition times as some studies were carried out during the day, while others were conducted overnight. These discrepancies are represented by the large standard deviations shown in Fig. 3.7(a) and 3.7(c).

3.1.1.6 Brillouin spectra: acquisition and analysis

Spectral analysis for spectra acquired by all spectrometers was completed using custom batch processing scripts in OriginPro [129]. All spectra were processed using partial-least-squares background subtraction and Lorentz fit methods. Brillouin peak positions (weighted centers) and Brillouin peak linewidths (FWHM) were determined accordingly.The distance between Stokes and anti-Stokes peaks corresponds to twice the Brillouin frequency shift, so by measuring spectral peak locations we can extrapolate the magnitude of the Brillouin frequency shifts with high accuracy and precision. This analysis allows for a direct look at the performance of each spectrometer against acquisition time, with a focus on accuracy and precision of measurements and spectral resolution. Though we applied the same background subtraction and Lorentz fit to all spectra, we could not use the same batch processing script for spectra acquired across all three spectrometers. The TFPI spectra contain only three peaks and all detector-pixels are defined with set frequency spacing, making analysis straightforward. An example of the spectra acquired from the TFPI-based spectrometer is provided in Fig. 3.4. The VIPA-based spectra are more complex, composed of multiple non-linearly spaced projections from VIPA to detector. To account for the angular-dispersion nature of the VIPAs and nonlinear spacing of projected Brillouin peaks, we applied a scaling algorithm to normalize the Brillouin peak positions across FSR iterations and accurately fit peaks to their respective frequency values [121]. The algorithm starts by finding each peak location and fitting each peak to a Lorentzian curve profile. After each peak location has been identified, a heuristic polynomial fit method is used to fit the locations of either the Stokes or anti-Stokes Brillouin peaks (defined by the first, third, fifth, and seventh peak locations by peak center, and stokes or anti-stokes identity assigned by the user) to the sequential projections of the VIPA, with

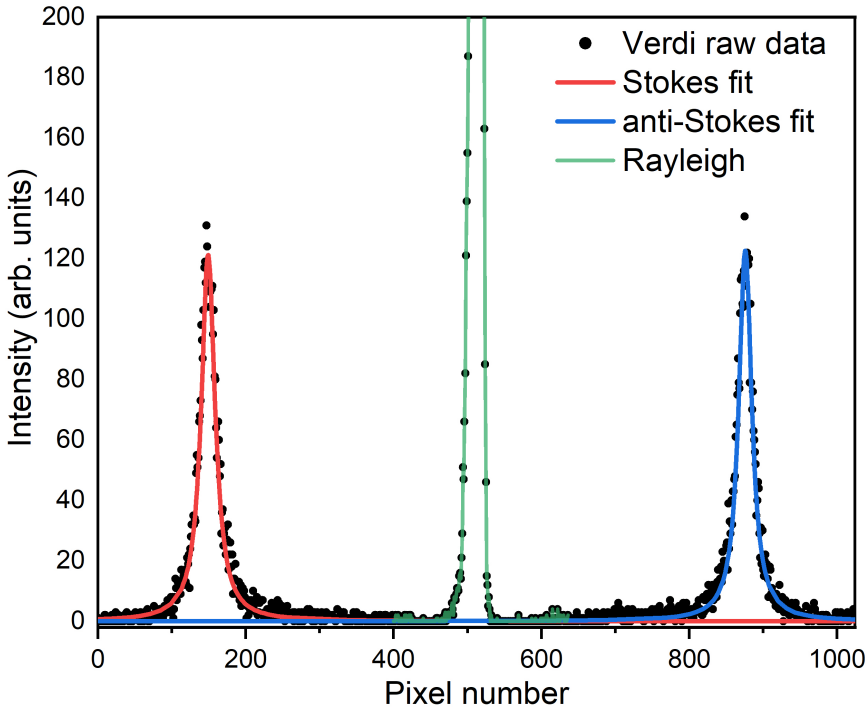

Figure 3.4: Raw spectra acquired from spectrometer (using Verdi G2 laser) and the Lorentzian fit examples for TFPI spectra. The pixel number along the x-axis has a set frequency conversion determined by FSR of the TFPI, as determined by the spacing TFPI optical flats.

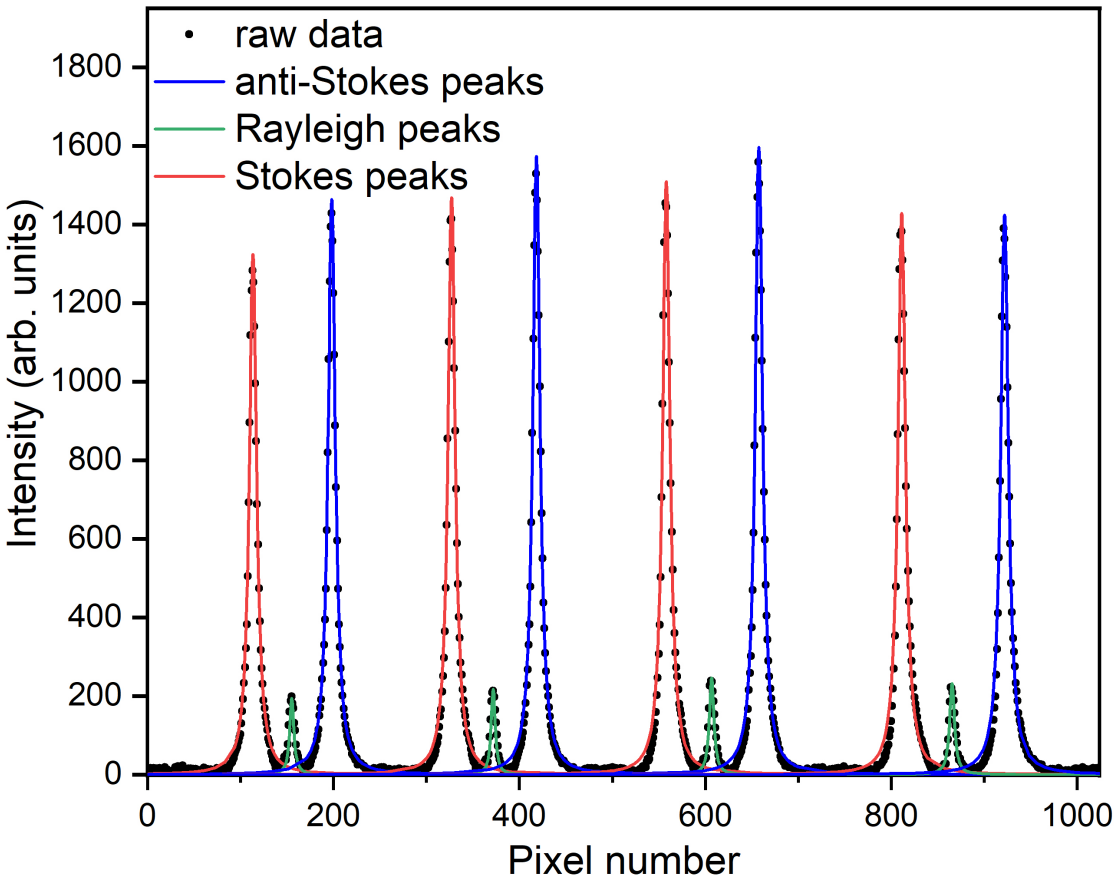

Figure 3.5: Example of raw spectral data and respective Lorentzian fit for each spectral peak, including Stokes, anti-Stokes, and Rayleigh peak for each of four FSR iterations across the detector from the VIPA. The x-axis is initially recorded as pixel number, relative to the position of the image on the CCD detector, and is later converted to GHz frequency through a polynomial fitting algorithm.

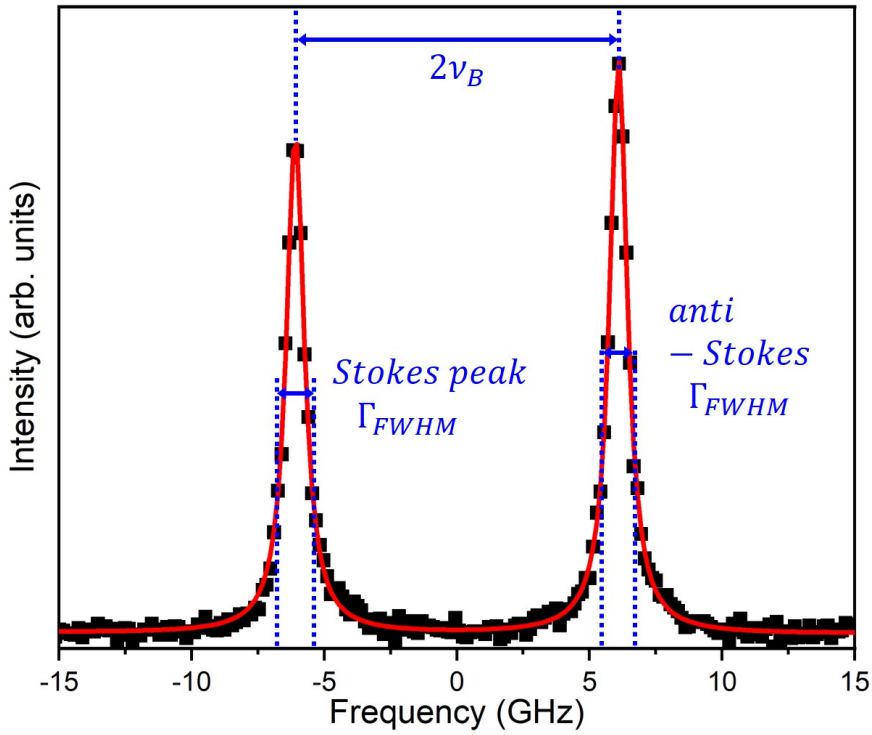

Figure 3.6: Raw data and respective Lorentzian fits from a single Brillouin spectral pair as acquired across one FSR of the VIPA-based spectrometer. The x-axis, provided in GHz frequency, has been converted from pixel position (location) using the polynomial fit method mentioned in the discussion of spectral analysis. Blue arrows, dash lines, and lettering indicate the distance between peak centers (twice the Brillouin frequency shift ν_B) and each peaks respective linewidth measurement (Γ_{FWHM}).

separations defined by the VIPA FSR. This fit method generates a curve by which the x-axis can be converted from pixel number and location to respective GHz frequency. The separation of each sequential Stokes or anti-Stokes peak iteration is assumed to match that of the VIPA FSR. Thus the scaling fit provides the respective Brillouin frequency shifts for each peak at their respective position across the detector. An example of the spectra collected and respective Lorentzian fits for each of the Stokes, anti-Stokes, and Rayleigh peaks from the VIPA-based spectrometers is provided in Fig. 3.5. Due to the strong absorption lines in the molecular absorption filter, the Rayleigh peaks are usually absent from the acquired spectra. They are visible in Fig. 3.5 as the laser wavelength was tuned very slightly off the absorption line, to allow for visualization of the elastically scattered Rayleigh peaks. Spectra and their analysis are discussed further in the results section of this

chapter. A typical Brillouin spectral peak pair is shown in Fig. 3.6, with x-axis pixel:frequency conversion and the excitation wavelength properly tuned to match an I_2 absorption line.

We repeated each acquisition cycle 50 times per trial with acquisition times ranging from 0.01 second to 100 s for the 780 nm VIPA-systems and from 0.512 to 102.4 s for the 532 nm TFPI and VIPA systems. The average Brillouin frequency shift ν_B and average Brillouin peak linewidth measurements Γ_{FWHM} were then determined for each data acquisition set.

3.1.2 Experiment summary and results

We analyzed Brillouin spectra acquired from three modern Brillouin spectrometers. Our analysis process involved using the same analysis methods across all data sets to eliminate any extra variables between system types. The results of the spectral analyses is presented and discussed in the following sections. While the purpose of this analysis was not intended to provide a statistics-based comparative analysis, the reader may be able to draw specific conclusions regarding instrument performance comparison from the information provided. Specific Brillouin frequency shift and Brillouin peak linewidth (FWHM) measurements are provided during the discussion of each system results. The values provided are specific to 0.5 second acquisition time for the 780 nm VIPA-based spectrometer and 0.512 seconds acquisition time for the 532 nm TFPI and 532 nm VIPA-based spectrometers. These specific values are provided to give a quantifiable look at the performance of each spectrometer and their individual performances at a specific acquisition time, i.e. the fastest acquisition time that we could achieve with the scanning TFPI and the 532 nm VIPA-based spectrometer at very low power. We determined the optimal acquisition time for each system as the fastest time at which the systems could achieve either the best precision spectral resolution, or the fastest speed that the system could acquire data while remaining within range of the desired spectral precision as measured by the standard deviation of ν_B over 50 measurements ($\leq$ 10 MHz).

3.1.2.1 Results: Tandem 6-pass Fabry-Perot interferometer (TFPI)

The 6-pass scanning TFPI system recorded a reference beam along with the Brillouin spectra. This reference beam allows for system stabilization during signal acquisition and provides a clear indication for the location of the known Rayleigh frequency line. The results of spectra analysis for the TFPI system are presented alongside the spectra analysis from the VIPA-based systems in Fig. 3.7(a) and 3.7(b). The spectra acquired using 532 nm incident wavelength are combined into a single graph to allow for a direct look at their performance. Likewise, since two laser sources were used for the TFPI and 780 nm VIPA-based spectrometers, plots from the same system with different lasers are set in overlay, for direct comparison.

The first data set for this assessment was acquired with the TFPI system and Torus 532 laser. Power measured at the sample was approximately 30mW. The averaged Brillouin frequency shift for acetone was measured as $\nu_B^{TFPI} = 5.94 \pm 0.04 GHz$ at 0.512 s acquisition time. The averaged Brillouin peak linewidth was measured to be $\Gamma_{FWHM}^{TFPI} = 678 \pm 35\ MHz$. These measurements are in agreement with the expected theoretical value of $\nu_{B,th} = 5.936\ GHz$ [128]. The TFPI-based spectrometer was set with the mirror spacing corresponding to a FSR = 50 GHz and an inter-channel resolution of 91.7 MHz for each scan in the first assessment. This mirror spacing gives poor spectral resolution and what appears to be very high precision in measurements. We repeatedly measured peak positions to be in the same position across multiple or even all scan iterations. However, what appears to be an exceptionally low standard deviation in measurements is simply the result of the poor spectral resolution. With this specific mirror spacing, any variance in peak position below $\sim$180 MHz ($\pm$90 MHz) is essentially undetectable.

The issue of poor spectral resolution is easily addressed, however, as a major benefit of TFPI systems is that the mirror spacings for cavities are tunable, and thus can be adjusted to improve FSR and spectral resolution. The trade-off being that the signal acquisition time must increase to maintain accuracy. Analysis suggests that the optimal acquisition time for this system with these settings is between 6 and 8 s. Count rates at the Brillouin peaks were found to be $\approx$ 2.44 counts/s per mW of incident optical power at the sample. Clearly, the low spectral resolution along

with less than ideal laser performance was cause for alarm. Therefore, a new SLM laser source (Verdi G2, Coherent Inc.) was used to replicate the experiment with the TFPI mirrors tuned to a more appropriate scan range with FSR = 16.57 GHz and inter-channel resolution of 16.18 MHz. While the original laser source itself may not have been performing well during this experiment, we acknowledge that the primary source for poor spectral resolution was the tuning of the TFPI mirrors, and less-so the performance of the original laser.

Power recorded at the sample with the new SLM laser was approximately 29 mW. The averaged Brillouin frequency shift for acetone was measured to be $\nu_B^{TFPI_2} = 5.92 \pm 0.007\, GHz$ at 0.512 s acquisition time. The averaged Brillouin peak linewidth was measured to be $\Gamma_{FWHM}^{TFPI_2} = 394 \pm 29\, MHz$. Optimal acquisition time was determined to be between 2 and 3 s. This is a significant improvement over the previous results, indicating a severe dependence on the light source stability and laser line width, as well as the finesse and FSR of the TFPI cavities. While these dependencies are well known, this procedure allowed us to diagnose and significantly improve our TFPI system and to further assess the limits of our spectrometer design with less emphases on individual component limitations.

3.1.2.2 Results: VIPA-based spectrometer at 780 nm with ^{85}Rb absorption cell

The first VIPA-based spectrometer, designed around excitation wavelength of 780 nm, was also tested with two laser sources (ECDL and iTLA). With the ECDL laser source, the averaged Brillouin frequency shift for acetone was measured as $\nu_B^{780} = 4.09 \pm 0.003\, GHz$. The Brillouin peak linewidth was measured to be $\Gamma_{FWHM}^{780} = 692 \pm 5\, MHz$. These measurements are in agreement to within 1% of the expected value of $\nu_{B,th} = 4.039\, GHz$ as calculated from the average index of refraction and speed of sound in acetone [130, 131]. Laser power at the sample was approximately 28mW. Photon count-energy ratio of the ECDL VIPA-based setup was found to be 10.38 counts/s per mW of incident optical power at the sample, with the reported 0.5 s acquisition time. The optimal acquisition time for the 780 nm VIPA-based system with ECDL source was between 70 and 100 ms. Spectra were obtainable at faster acquisition times; however, the SNR began to degrade significantly from roughly 10 dB at 100 ms to almost 1 dB at 20 ms.

Acquisition times longer than 100 ms were determined not to provide for improved measurements, but rather served to increase risk of external and environmental disruptions and of laser drift. These undesired effects are demonstrated by the remarkable increase in standard deviation in Brillouin peak linewidth measurements shown in Fig. 3.7(d) for the two longest acquisition times with the ECDL. We determined that the drastic increase in standard deviation was likely due to instability in the laser source; i.e. the result of drift in laser wavelength, or the result of a laser mode hop.

We installed the iTLA source for the 780 nm VIPA-based system to overcome the instability experienced with the ECDL source and to eliminate the extra materials and electronic locking system needed to control the piezo device. Essentially, the iTLA laser was installed to simplify the system and provide a more reliable and more narrow-band excitation source. With the iTLA source, we repeated the experiment for acquisition times up to 1 s. The results of analysis are presented in Fig. 3.7(c) and 3.7(d) in overlay with the previous ECDL results allowing for a quick look and direct comparison. Longer acquisition times were omitted, since previous experiments and analysis had proven that longer acquisition times were of no benefit and the overall goal was to evaluate the spectrometer performance at faster acquisition times.

With the iTLA source at 0.5 s acquisition time, the averaged Brillouin frequency shift for acetone was measured as $\nu_B^{iTLA} = 4.10 \pm 0.003\, GHz$. The Brillouin peak linewidth was measured to be $\Gamma_{FWHM}^{iTLA} = 511 \pm 5\, MHz$. These results are within $\sim$1.5% the expected value of $\nu_{B,th} = 4.039\, GHz$. Optimal acquisition time for the 780 nm VIPA-based system with iTLA source was between 20 and 50 ms, faster than any previous reports for single-point acquisition for spontaneous Brillouin at the time of these measurements. In fact, longer acquisition times than this did not provide for any improvements in accuracy, precision, or spectral resolution. The iTLA technology is based on lasers used in the Telecom industry, modified by the manufacturer to meet the stringent requirements of high SNR applications like those in a spectroscopy laboratory setting. As with the TFPI results, we see a strong dependence on laser source when looking at the linewidth measurements between the ECDL and iTLA lasers. This iTLA laser has excellent stability and more narrow-band output than the ECDL laser that was originally used, and thus provides

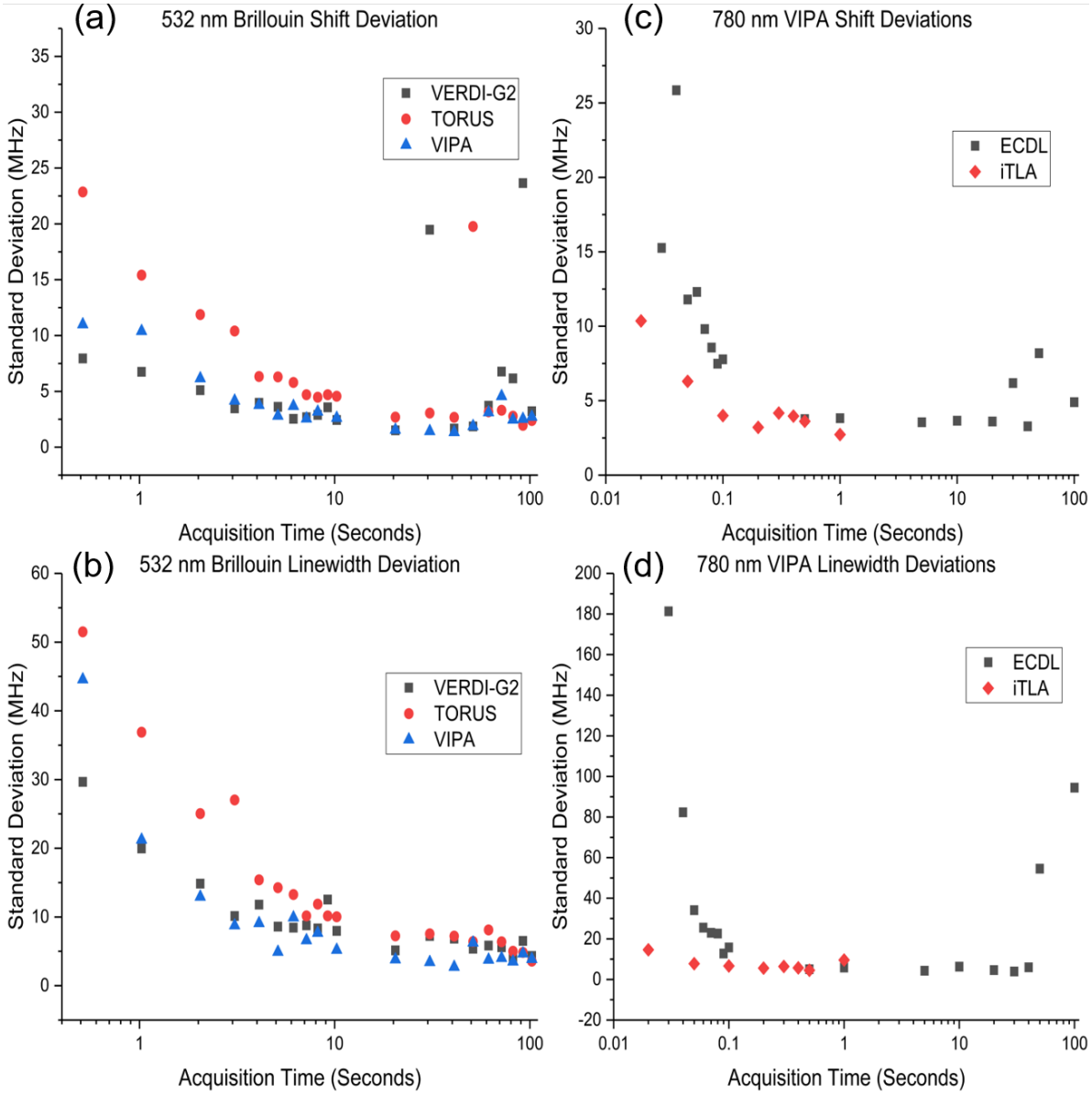

Figure 3.7: Standard deviations for average Brillouin frequency shifts (a) and linewidths (b) as measured by the 532 nm TFPI, with black squares (Torus) and red circles (Verdi) representing the two laser sources used. Blue triangles represent the results from the 532 nm VIPA-based spectrometer. Results from the 780 nm VIPA-based spectrometer are provided with standard deviation of the average Brillouin frequency shifts (c) and linewidths (d), with black squares representing the original ECDL laser and red diamonds representing the new iTLA-based laser setup.

for much better results.

3.1.2.3 Results: VIPA-based spectrometer at 532 nm with I_2 absorption cell

The second VIPA-based spectrometer matched the 532 nm excitation wavelength of the TFPI spectrometer, and analysis results are shown in overlay with TFPI results in Fig. 3.7(a) and 3.7(b). The spectral resolution of the 532 nm VIPA-based spectrometer was determined by measuring the VIPA-output of the source laser linewidth at very low power and with minimal I_2 absorption. The resolution was measured to be $\delta\nu = 485 \pm 12\, MHz$, and a visualization of the VIPA output and resolution measurement is provided in Fig. 3.8.

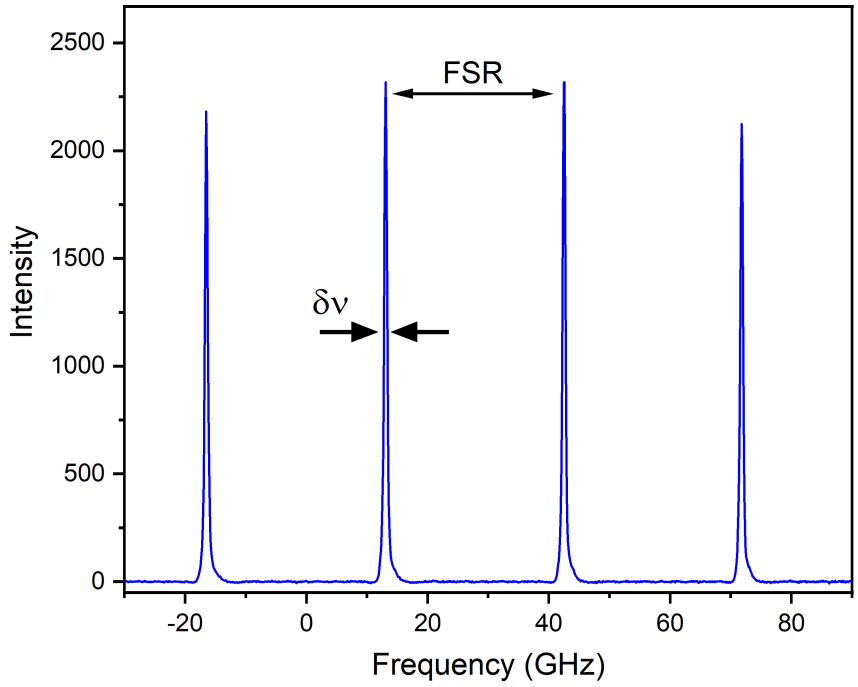

Figure 3.8: Brillouin spectral resolution. The narrow spectral lines from the 532 nm probe laser at the spectrometer camera with 4 iterations of the VIPA FSR captured. Individual peaks were resolved from the measure of the peak FWHM. The spectral resolution was determined to be $\delta\nu = 485 \pm 12\, MHz$.

The averaged Brillouin frequency shift for acetone measured by the 532 nm VIPA-based spectrometer was $\nu_B^{532} = 6.05 \pm 0.004\, GHz$, with a peak linewidth of $\Gamma_{FHWM}^{532} = 791 \pm 12\, MHz$ at an acquisition time of 0.512 s. These results are within 2% of the expected value (again,

$\nu_{B,th} = 5.936\ GHz$). As shown in Fig. 3.7(b), the precision of Brillouin peak linewidth measurements from this system are much greater than that of the TFPI system. The difference in linewidth recorded is in-part due to the high NA of the microscope objective used, and the properties of the VIPA for this spectrometer. Likewise, a recent report and our own analysis has pointed to a potential for further optimization of the cylindrical lens leading to the VIPA input, and the position and angle of the VIPA to the spherical lens and detector to improve linewidth measurements and spectral resolution [114, 126, 118]. Optimal acquisition time for this spectrometer was determined to be between 0.05 and 0.2 s. It is possible for this spectrometer to achieve results equal to and even greater than this at faster acquisition times. However, since incident laser power was set very low to allow for detection at longer acquisition times, spectra from acquisition times faster than this were sub-optimal and noisy with too low a SNR to analyze effectively.

3.1.3 Additional discussion

In summary, we have assessed the performance of three modern Brillouin spectrometers of two different designs and excitation wavelengths, and report the fastest spontaneous Brillouin measurements to date. The spectrometers evaluated were a conventional scanning 6-pass TFPI system at 532 nm and two custom-built VIPA-based spectrometers with atomic absorption-based notch filters at 532 nm and 780 nm respectively. Brillouin spectra were acquired from acetone, a common standard for Brillouin measurements often used as a calibration sample. Throughout the investigation, we were successful in using our analysis to evaluate and diagnose potential issues with our spectrometers. We clearly demonstrated the dependence of measurement reliability on excitation source quality, a critical issue with Brillouin spectrometer design. Our analysis showed the scanning 6-pass TFPI system (with the new SLM laser) had its most reliable measurements, with lowest standard deviation in Brillouin frequency shift, linewidth as well as greatest accuracy, at acquisition times between 2 and 3 s. While this is significantly faster than the acquisition times of older systems, total scan times still broach on several minutes for a complete sequence of 50 iterations. However, a primary strength of this design is that spectral resolution of a TFPI is determined by an inverse relationship with finesse ($1/\mathcal{F}$) of the Fabry-Perot cavity, and thus can be fine-tuned

to meet the needs of the sample and individual situations.

With the 532 nm VIPA-based spectrometer, we maintained a significantly lower laser power at the sample 0.8 mW, compared to the other spectrometers. Though lower than desired, this power level was maintained for all spectra acquisition times to maintain uniformity throughout the experiment. As stated previously, this power level was chosen to avoid detector saturation at long acquisition times (greater than 10 s). This low laser power provided for poor resolution and low signal-noise ratio (SNR) at fast acquisition times (less than 0.2 s). Since both 532 nm and 780 nm spectrometers follow the same design and quantities of interest in Brillouin measurements are often sound velocity and stiffness tensor elements, our primary focus for discussing the VIPA-based spectrometer performance is that of the 780 nm spectrometer. This is due in part to the low incident power of the 532 nm system, but also because sound velocity scales directly with wavelength, thus a small uncertainty in frequency shift measurements at 780 nm would be more significant than at 532 nm.

The most reliable measurements for our 780 nm VIPA-based design were determined to be at acquisition times between 20 and 50 ms. At the time of this assessments publication, the fastest single-point acquisition times that had been reported for spontaneous Brillouin measurements were at 50 ms, since below 100 ms, SNR is often too low for reliable measurements. Here, we report measurements as fast as 20 ms acquisition time, more than two times faster than the fastest times previously reported [110]. Since VIPAs are made of a single prism of fixed dimensions, a potential approach to achieving greater spectral resolution, would be to design an interchangeable stage with multiple VIPAs of different FSR, chosen based on the needs of each experimental. The closer the FSR is to the expected Brillouin frequency shift, the greater accuracy and resolution one can expect.

Laser stability and the quality of optical components are the primary factors in determining the overall quality, accuracy, and spectral resolution of Brillouin spectrometer measurements, and spectrometer design has the most significant impact on acquisition speed. The accuracy of Brillouin measurements is influenced by spectra signal-to-noise ratio, which is determined by input

laser power, scattering efficiency (wavelength dependent), throughput of the spectrometer, sensitivity of the detector, quality of optical components, and a variety of other factors. Basically, since modern custom-built spectrometers (such as Brillouin spectrometers in research laboratories) are designed around a wide range of available laser sources and optical components this means that each spectrometer should have its own optimal acquisition time "sweet-spot" for achieving high accuracy and spectral resolution [114, 118, 132]. External conditions such as environment temperatures and mechanical vibrations can also play a role in determining how well spectrometers perform, but these conditions are not critical to spectrometer design and can be accounted for by sample isolation or through corrections in data analysis.

Finally, we note that acetone - the sample selected for this experiment, is often used as a calibration sample for Brillouin spectroscopy and does not present the same challenges that more turbid or opaque samples may present. In this regard, the more conventional TFPI systems have historically been more reliable and accurate for Brillouin spectroscopy measurements. Recent developments in VIPA-based spectroscopy related to increased elastic extinction ratios and background subtraction have led to significant advances [70, 120, 133], and future studies relating the performance of such systems with turbid and highly-scattering samples may provide further insight along with the data presented in this study.

3.2 Conclusion

By evaluating the performance of our spectrometer design, we were successful in identifying and correcting for specific issues and achieved improvements in overall performance, even reporting the fastest signal acquisition times to date for a single-point acquisition of Brillouin spectra. We hope to use the information gathered from this experiment to guide future designs and development of Brillouin spectrometers and hopefully provide direction for overcoming limitations inherent to each spectrometer design. The following chapter provides details of how we investigated the impact of an external stimulus on cellular and subcellular biomechanics using our VIPA-based spectrometer design.

4. BRILLOUIN SPECTROSCOPY: CELLULAR AND SUB-CELLULAR BIOMECHANICS AND RESPONSE TO EXTERNAL STIMULI

Here, we provide detail about how we combined recent advances from Brillouin spectroscopy literature to achieve a series of firsts: 1.) the first non-contact recording of subcellular biomechanical changes in response to a non-specific external stimulus 2.) the first reporting of sub-second biomechanical changes using spontaneous Brillouin spectroscopy, and 3.) the first reporting of sub-second dynamic biomechanical changes with location specificity in each of the cytoplasm, nucleoplasm, and nucleolar compartments of cells. To realize these accomplishments, we built a custom confocal Raman and Brillouin microscope capable of simultaneously recording chemically- and mechanically specific information from intracellular compartments. We then used this microscope to target several areas inside cells from the CHO-K1 cell line to record Raman and Brillouin spectra and observe the changes induced by exposure to a brief, but intense 600 ns electrical stimulus (herein referred to as nsPEF), which is known to disrupt several key components of the cell cytoskeleton. Disruption of these cytoskeletal components should induce biomechanical alterations in living cells which, we sought to measure using Brillouin spectroscopy. The following sections couple spectroscopy data with fluorescence microscopy time series imaging of observing cell plasma membrane and cytoskeleton disruption to further explore and explain our results.

We demonstrate the applicability of Brillouin spectroscopy as a means for observing immediate changes in viscoelastic properties of cells and subcellular components in response to an external stimulus. Additional information is provided in the discussion section of this chapter as to why we expect this technology to be particularly useful for not only basic-level biomedical sciences, but also for a wide range of clinical and research applications for diagnostic, progression monitoring, and treatment of various diseases across a range of fields from oncology [134, 135, 136], cardiology [137], ophthalmology [95, 138], and neurology [139, 140], to name only a few.

4.1 Introduction: Brillouin spectroscopy for investigating biomechanics

Cellular biomechanics have been implicated in a wide variety of cellular processes and disease states. Changes in a cells mechanical properties can have a profound impact on the cells behavior and function [141, 142, 143]. The relationship between cell function and microscale mechanical properties has become evident through decades of research on disease and cancer development. Cell mechanical and viscoelastic properties have been linked to cancer development, viral infections, chronic illnesses like asthma, and even ageing. For example, Glaucoma is associated with both changes in the optic nerve extracellular matrix, which drives tissue fibrosis and stiffening [144], and with increased intraocular pressure driven by changes in endothelial cell viscoelasticity [145]. Likewise, changes have been observed in the viscoelastic properties of tissues and cells after viral infection [146, 147, 143], and in cases of oncology, where the mechanical properties of both tissues and cells have become a topic of intense focus [148]. Recent oncological studies have shown that cells become more compliant during tumorigenesis and a decreases in cancer cell stiffness are linked to cell reprogramming before tumorigenesis [149]. Loss of plasticity and reduced stiffness has recently been identified as a biomarker for potential diagnostics and prediction of metastatic potential in thyroid, ovarian, and breast cancer [150]; and tissue stiffening has been shown to lead to collective migration and coordination of morphogenesis in the beginning stages of tumorigenesis [151]. Further examples and more detailed information can be found in extensive review articles covering the links between cell and tissue mechanical properties as related to both disease development [152, 153] and medical applications [154, 155].

Biomechanics research has demonstrated that measuring the viscoelastic properties of tissue and cells *in situ* can provide researchers and clinicians with critical information related to cells, tissues, their environments, disease pathology, and their general wellness conditions. As such, viscoelastic properties are of great interest to investigators and many experimental techniques have been developed or used for biological applications. Atomic force microscopy (AFM) [156, 157], profile microindentation [158], magnetic twisting cytometry [159], particle tracking microrheology [160], and optical stretching [161] are only some of the methods used to investigate cell and tissue

biomechanics.

A challenge in modern biomechanics investigations is that nearly all modern investigative methods are highly destructive or mechanically invasive, altering or destroying the sample during the measurement. Optical rheological techniques circumvent this issue by providing non-contact, non-destructive testing of biologic samples. Less invasive optical techniques such as optical coherence elastography have shown promise and become more prevalent for non-destructive tissue-level studies, but still require mechanical excitations and are limited to a much larger spatial resolution [162]. A recent review by Steelman, et al. provides a comprehensive overview regarding these optical-based measurements for tissue diagnosis [163]. Eldridge, et al. demonstrated a novel non-contact quantitative phase imaging approach in 2017 that relates variances of refractive index to disorder strength, a parameter linked to cell stiffness [164]. Their results are promising; however, they rely on a derived parameter which correlates with mechanical behavior through a mechanism that is poorly understood, and their technique cannot be translated to most *in vivo* studies as their method requires light transmission through the sample. As the search for viable cellular and subcellular-level measurement technologies continues, a new laser-based alternative has emerged as a viable tool for mechanobiology: Brillouin spectroscopy [84, 47, 90, 165].

Brillouin spectroscopy is an all-optical, non-invasive, label-free technique that had previously been limited to mostly traditional materials science investigations due to weak signal strengths and slow scanning times. New Brillouin spectrometer designs have recently initiated a phase of rapid development [50, 58] and evolution of the technology. As discussed in Chapter 2, a plethora of new instrumentation and application ideas have since allowed for a Brillouin-renaissance in recent years, and have established Brillouin spectroscopy and microscopy as a powerful tool for biomedical sensing and imaging applications [110, 84, 90].Researchers have recently demonstrated tissue, cellular, and even nucleus level measurements using Brillouin spectroscopy and microscopy [166, 133, 111, 49, 102, 106, 167]; however, its utility for measuring fast (sub one-second) dynamic intracellular changes in response to external stimuli has not yet been explored, particularly at subcellular levels or from within cell nuclei and nucleoli.

4.2 Materials, methods, and experimental design: cellular response to nsPEF

Mammalian cells are complex dynamic systems that develop and change in response to their environment. Cells constantly respond to stresses through means of chemical signaling and pathways. Cells also feel and respond to forces through means of mechanotransduction [168, 169, 170]. The pulling, compression, and torsion of muscle movements and contractions, or shear stress as blood flows are simple examples of forces that cells experience in the human body. In a laboratory setting, scientists apply a wide range of stimuli and insults to cells in the process of developing fundamental theories and understandings of basic functions and reactions. Figure 4.1 provides an illustration of some stresses and stimuli that cells may be subject to, along with examples of both cellular responses (membrane and cytoskeletal filament disruptions) and the imaging modalities used for investigating cellular behavior.

4.2.1 Custom multi-modal microspectroscopy system

We used the custom multi-modal microscopy system described in Chapter 3. This system is capable of both Raman and Brillouin spectral measurements and uses a Brillouin spectrometer following a VIPA-based design. The system follows the same schematic as provided in Fig. 3.2. In brief, the system used a tunable, ultra-narrow ($<$ 1 kHz) single-frequency laser (Koheras ADJUSTIK/BOOSTIK Y10; NKT Photonics) with 1064 nm center wavelength and 2.1 W maximum output power. A second harmonic generation (SHG) crystal (MSGH1064-1.0-20; Covesion, Ltd.) was used to generate an output wavelength of 532 nm with 150 mW maximum output power. The laser was coupled into the rear port of an inverted microscope (IX73; Olympus Corp.) and focused to the sample using a 1.42 NA 60X objective lens (UPLXAPO 60XO; Olympus Corp.). The spatial resolution of Brillouin spectral imaging is primarily limited by the mean free path of vibrational wavelengths and the numerical aperture of the objective lens; in our confocal setup, the lateral and axial resolution of Brillouin imaging system was estimated to be approximately 500 nm $\times$ 500 nm $\times$ $\sim$1 μm, respectively as determined by measuring the Brillouin spectra across material interfaces and substrate reflections. Additional information relating to the mechanical resolution

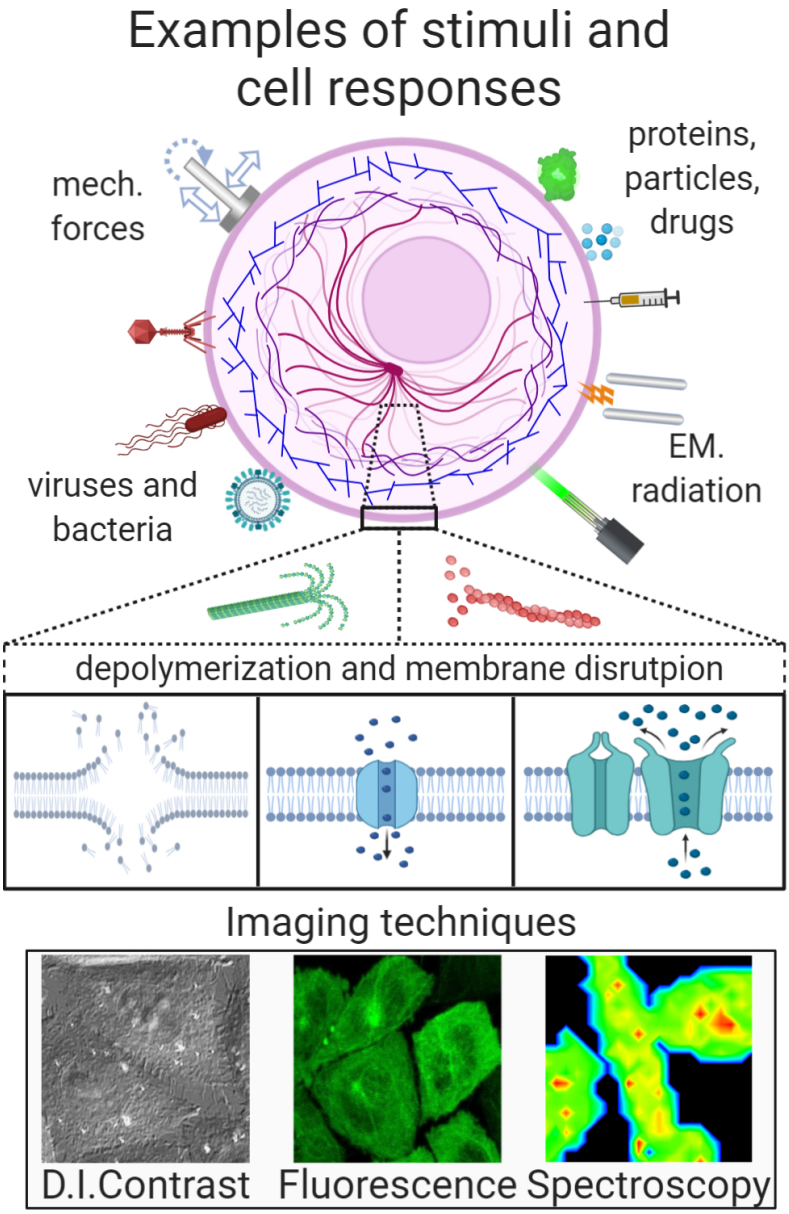

Figure 4.1: Conceptual idea – monitoring cell stimuli, stresses, and responses. Illustration of potential external stresses and stimuli cells may be exposed to, a generalized concept of membrane and cytoskeletal filament disruption, and examples of imaging techniques (DIC imaging, Fluorescence imaging, Spectroscopic imaging) for observing and monitoring cellular response. Figure created with BioRender.com

of Brillouin microscopy systems is provided in the discussion, with more specific detail given in Chapter 2. The axial resolution for the Raman acquisitions was expected to be approximately 25% larger than that of the Brillouin spectra, as the confocal pinhole for Raman photons was selected to be slightly larger than the diffraction limited airy disk pattern for increased signal strength. Light was collected from the sample in a 180° back-scattered (epi-illumination type) configuration by the same objective and separated into respective Raman and Brillouin spectral paths by a dichroic beam splitter (RazorEdge LPD02-532RU; Semrock). Appropriate pinholes were placed in each path to provide confocal gating of the scattered photons. Raman signal was passed through a narrow band notch filter, and directed into a spectrometer (Shamrock 303i, Andor Technology Ltd.) where it was dispersed by a 600 line/mm reflective grating and collected by a CCD camera (iDus 420, Andor Technology Ltd., cooled to 50 °C). Brillouin signal was passed through an I_2 absorption cell (GC19100-I; ThorLabs, Inc.) to a virtually imaged phase array (VIPA)-based Brillouin spectrometer and collected by an EMCCD camera (Ixon Ultra 888; Andor Technologies Ltd., water cooled to 100 °C). This Brillouin spectrometer arrangement uses the I_2 cell as an ultra-narrow absorption-based notch filter for removing background Rayleigh scattered light that would otherwise saturate the detector and cover the much weaker Brillouin peaks [70, 171], as mentioned in Chapter 3. The VIPA used in our spectrometer had a free spectral range (FSR) of 29.95 GHz, a net finesse $\sim$60, and a theoretical bandwidth of 0.84 GHz (OP-6721-3371-2; Light Machinery, Inc.). We determined our Brillouin spectrometer to have spectral contrast of -80 dB, spectral resolution $\delta\nu = 485 \pm 12\ MHz$, and sub 10 MHz spectral precision, as specified in Chapter 3.

4.2.2 Nanosecond pulsed electric fields (nsPEF) system and cell stimulus

The external stimulus applied to the cells was a 600 ns duration electrical impulse driven by a high-power pulse generator (Model 350, Velonex, Inc.) and delivered via a custom microelectrode arrangement [172, 173, 21]. A pair of tungsten electrodes, 125 μm in diameter spaced approximately 200 μm apart, were placed on opposite sides of target cells approximately 50 μm above the petri dish cover slip at a 45° angle using a micromanipulator (MPC-200; Sutter Instruments). A digital delay pulse generator (DG535; Stanford Research Systems, Inc.) was used to first trigger

the start of spectral measurements, and then, after a preset delay of 10 seconds, trigger a single nsPEF pulse. Each nsPEF pulse delivery was monitored and recorded (pulse amplitude and width) using a 100× voltage probe (P5100A; TekTronix) coupled to an oscilloscope (TDS3054C; TekTronix)[1]

4.2.3 Cell culture and sample preparation

CHO-K1 cells (ATCC® CCL-61™, Chinese hamster ovary) were cultured and maintained following the recommended protocol. Cultures were maintained at 37 °C with 5 % CO_2 in air with 95% relative humidity, and propagated in Kaighn's Modification of Ham's F-12 Medium (F-12K Medium, ATCC® 30-2020™) supplemented with 10 % fetal bovine serum (FBS, ATCC® 30-2020™), 2 mM L-glutamine, and 1% volume 100 U/mL penicillin/streptomycin (ATCC® 30-2300). 20,000 – 30,000 cells were seeded onto an imaging dish with polymer coverslip (μ-Dish 35 mm, low Grid-500; ibidi GmbH, Martinsried, Germany) to prepare samples for imaging. The following day, culture media was replaced with fresh media 30 minutes prior to imaging. Brillouin imaging was performed in cell culture media as opposed to standard imaging buffer solution because the proteins in cell media can help to inhibit cell swelling. The protein-induced swelling reduction helps to reduce the likelihood of any observed changes being due to cell swelling, rather than disruption of the cytoskeletal structures.

4.2.4 Subcellular Raman and Brillouin spectral measurements and signal acquisition

Single cells were located via bright field microscopy and positioned such that the target region was centered about the focal volume of the laser. Cell position could be determined by opening the microscopes rear-port shutter and visually comparing the cells location to the position of the laser spot reflected off of the glass substrate. Additionally, a small portion of the laser light reflected from the glass could be seen on the bright field camera and captured in the camera software (Pylon 6.2.0 Camera Software Suite for Windows; Basler AG, Ahrensburg, Germany). The camera software also allows the user to generate an on-screen cross hair with manual positioning, which

[1]This pulse delivery system matches that as described in Chapter 5. Additional detail on the nsPEF delivery system is provided in Appendix C.

we used for targeting and periodically verifying laser positioning between experiments. Specific regions of the cells were targeted using differential interference contrast (DIC) imaging. Once a target location was selected, the DIC optics (polarizer, Nomarski prism, and analyzer) were removed so that signal acquisition could begin.

Cells are living systems and dynamic in nature and thus may move during data acquisition. Therefore, bright field images of cells were recorded both before and after exposures. Images from before and after each exposure and recording session were visually inspected to ensure that no significant movement had occurred during the acquisition and that the laser was still focused in the target structure of the cell. If the images indicated that the intended target region had moved more than $\sim$15% with respect to the laser focus, the data set was discarded. The simultaneously acquired Raman spectra were also useful for indicating axial focal drift, and, therefore, were used as part of an exclusion criteria along with checking sample movement through images. The cell culture growth media contains the dye phenol red, which presents a large fluorescence signal that became immediately visible in the Raman spectra if axial drift led to the focus exiting the cell body. This also meant that the fluorescence of the growth medium served as a valuable tool in further ensuring proper placement of the focal zone before experiments. A representative example of Brillouin and Raman spectra acquired from within a cell is provided in Fig. 4.2). Examples of the Raman spectra collected from each of different regions within the cells and the surrounding media, after background subtraction, are presented in Fig. 4.3.

Raman and Brillouin spectra were acquired from randomly selected cells across several days, with individual cells selected per exposure, per target region, such that no two measurement series were recorded from the same cell. Spectra were acquired for a period of 100 seconds. nsPEF was applied at t = 10 seconds such that all trials had an initial 10 second baseline measurement in increments of Δt = 0.5 seconds. Signal acquisition continued for the following 90 seconds post-exposure to allow for observation of any changes in the mechanical properties of the target region immediately following the stimulus. All Brillouin measurements were standardized to the average of their own 10 second baseline measurements for comparison. All time-series measurements are

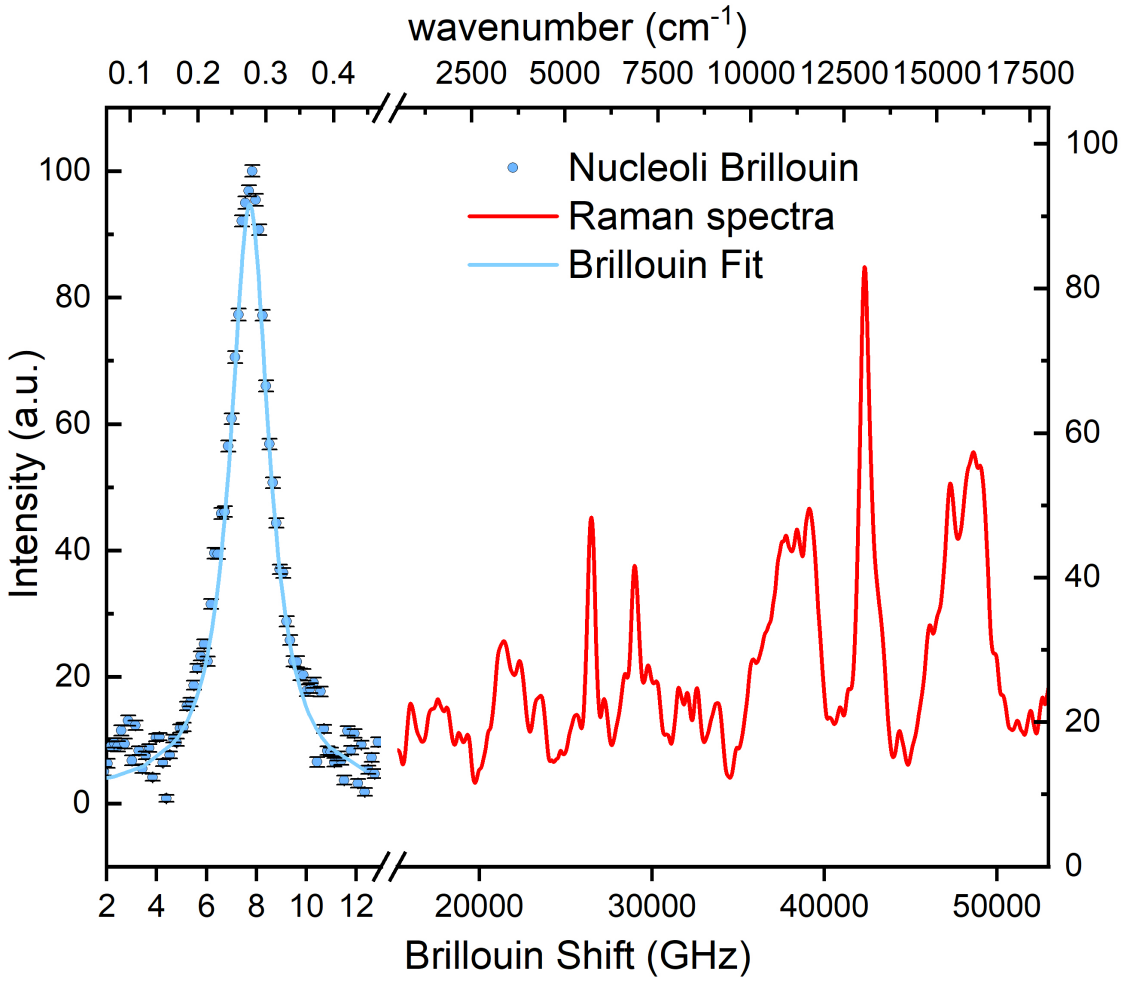

Figure 4.2: Example of raw Brillouin spectral data and respective Lorentzian fit for signal collected within a cell nucleolus, alongside the respective Raman spectra (after background subtraction). Top and bottom X-axis labels indicate the respective wavenumber (top) and frequency shift (bottom) of each spectra.

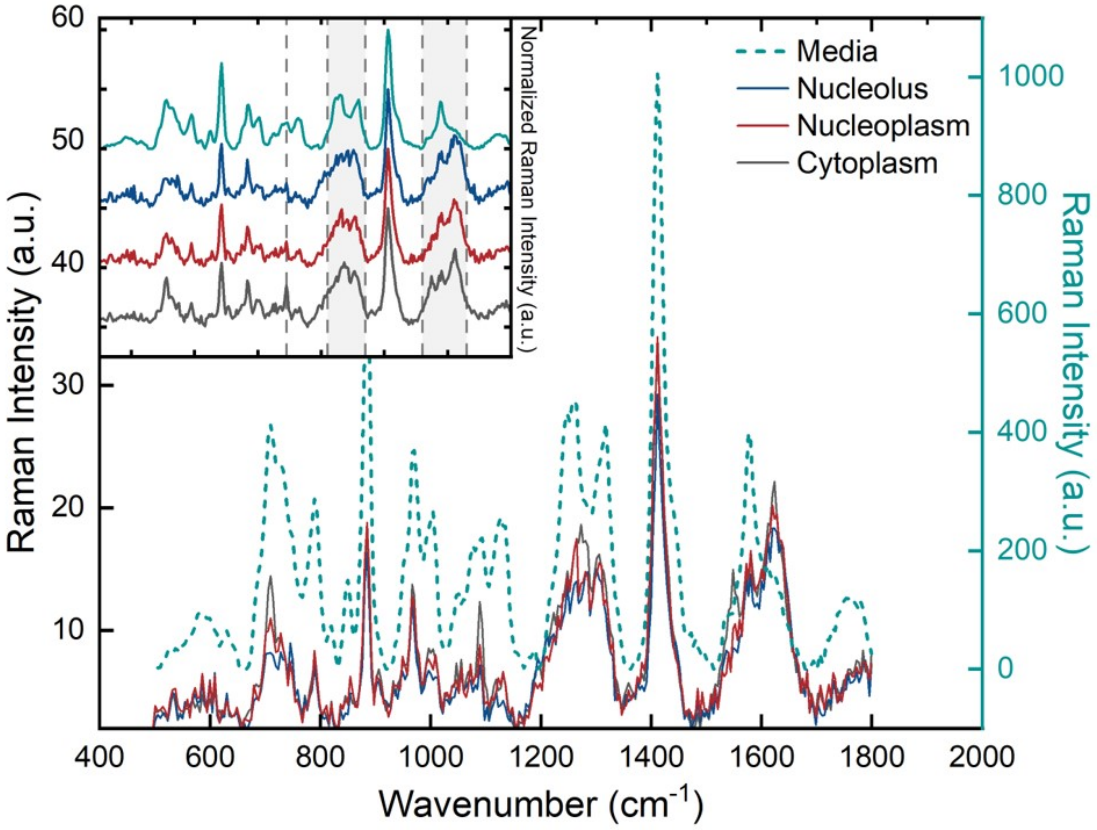

Figure 4.3: An example of Raman spectral data from each of the target regions within CHO-K1 cells and cell culture growth media after background subtraction. Without background subtraction, the fluorescence from the growth media overwhelms the spectral peaks which provided an excellent indication for if the focal volume drifted out of the cell body.

presented here as percent change, or percent value from the 10 second baseline average.

Laser power at the sample was kept below 4 mW to avoid localized heat damage and phototoxicity to the cells. A preliminary study showed that no morphological changes or cell blebbing were present near the focal volume in cells after a continuous 5-minute exposure at this power level. Each nsPEF exposure-response trial consisted of a 200 second laser exposure, for a total 240 spectral measurements (200 Brillouin and 40 Raman), with the nsPEF exposure occurring at frames 20 and 5 for Brillouin spectra and Raman spectral acquisitions, respectively. Acquisition times were 0.5 seconds for Brillouin spectra and 5 seconds for Raman spectra.

Spectra were plotted using OriginPro 2020b (OriginLab, Northampton, MA.)[129]. Brillouin spectral analysis was performed using a custom Python script [174]. Similar to the fitting algorithm discussed in Chapter 3, each Brillouin scattered peak location is found through a single peak Lorentzian fit with a least-squares fitting protocol. The location of each first peak for the four Brillouin frequency shift peak-pairs was then assigned a value equal to an arbitrarily assigned integer value, plus a multiple n = 1, 2, 3 times the full FSR of the VIPA. For instance, a VIPA of 29.95 GHz FSR could have the first, third, and fifth peaks assigned an initial arbitrary value of 0, 29.95, and 59.9 GHz, or any other series separated by the same 29.95 GHz FSR value. These newly defined peak location values were then used for a polynomial fit algorithm that provided for a pixel-to-GHz conversion for the entire acquired spectrum. The average Brillouin frequency shift for each spectral acquisition was then determined by the distance between each of the two peaks of visible Brillouin peak pairs. Raman spectral background subtraction was completed using a custom Matlab [175] code based on the modified polynomial fit method presented by Lieber and Mahadevan-Jansen [176]. Following background correction, Raman spectra from before exposure and 90 seconds after were compared to check for any changes in peak intensities and relative peak height ratios.

4.2.5 Fluorescence microscopy

Fluorescence microscopy investigations were carried out to observe and monitor three known cytoskeleton-related systems and changes induced by cell response to nsPEF exposure. The first, a

dye-uptake study that indicates destabilization or disruption of the plasma membrane. The second, a time series study of α-actinin labeled proteins to assess changes in the cell actin structure and network immediately following nsPEF. The third, another time series study with green fluorescent protein (GFP) labeled tubulin for observing changes to the microtubule network within the cells.

4.2.5.1 YO-PRO-1 dye uptake

YO-PRO-1 is a dye that is commonly used for nsPEF-based membrane permeabilization and nanoporation experiments. YO-PRO-1 dye is generally excluded from cells with intact membranes; however, the dye can permeate through the plasma membrane upon disruption or destabilization and thus allows for visualization of membrane damage. Increased intracellular fluorescence emission from YO-PRO-1 dye following nsPEF stimulus corresponds to cellular uptake of YO-PRO-1 dye and provides a measure of the extent of cell membrane damage induced by the exposure [177, 26, 178, 179]. Membrane disruption by nsPEF application not only indicates that the cell membrane itself has been damage, but also can lead to several reactions within the cell. One such reaction that has a strong impact on the cytoskeletal structures of interest in this study is a release of intracellular calcium stores from the mitochondria and the endoplasmic reticulum. This influx of calcium has been demonstrated to cause disruption of both actin and microtubule networks [180, 24]. In our preliminary investigation, dye uptake also provided an additional rather obvious but useful benefit in that it demonstrated effective delivery of the nsPEF to the cells, i.e. that there were no electrical shorts within the electrode housing that the oscilloscope could not detect. All dye uptake studies were performed over a total of 5 minutes and 10 seconds. The first 10 seconds were prior to application of nsPEF to allow for a baseline and background fluorescence measurement in each image series. The following five minutes of image acquisition were to provide a relatively long-term study of dye uptake to see if membrane recovery occurred within the time frames we were interested in. Membrane permeabilization and dye uptake experiments were conducted over a range of nsPEF intensities from 0 kV/cm to 20 kV/cm.

4.2.5.2 Fluorescence microscopy: observing actin and microtubules

The cytoskeleton of eukaryotic cells is made of filamentous proteins and provides mechanical support to the cell and its cytoplasmic constituents. There are three major classes of cytoskeletal elements: microtubules, intermediate filaments, and actin filaments. Therefore, disruption of any one of these types of filaments should lead to changes in the cell mechanical properties [181, 182, 183, 184]. Microtubules provide the base level organization of the cell cytoplasm and organelles. Actin filaments are abundant in eukaryotic cells and are typically found beneath the plasma membrane, where the actin cortex network provides mechanical support, allows for cell motility and movement, and help to determine the overall cell shape [185, 186].

We used two separate CHO-K1 cultures to investigate the changes in the cell cytoskeleton. One culture was transfected with GFP mEmerald-labeled tubulin and allowed for the observation of microtubule filaments. The second culture was labeled with RFP α-actinin, and allowed for observation of actin structures. Fluorescent images were acquired as a time series, recording ten seconds prior and up to five minutes post application of nsPEF stimulus. Additionally, z-stack image series were acquired pre- and post-nsPEF application to check for any major morphological changes or redistribution of the fluorescent labeled structures. Images were post-processed using ImageJ software (Version 1.53) [187]. Cell borders were manually selected, and cell mean fluorescence, relative fluorescence ($\delta F/F_o$) for time series, fluorescence standard deviations, and corrected total cell fluorescence (CTCF) was calculated by measuring the integrated fluorescence density minus the background average, multiplied by the total area of the cell volume [188]. Fluorescence background subtraction was taken from a standard normal distribution of each time series image. This procedure was used for each cell across every time point. Additionally, the standard deviation of fluorescence was used as an indication of changes in diffuse and non-diffuse structures from within microtubule and actin labeled cells. The values of CTCF are not reported; upon closer inspection, the trends and behaviors matched those of relative fluorescence, but with far less comprehensible numbers. Therefore, all fluorescence intensity values mentioned in this chapter are reported in terms of relative fluorescence, with respect to the initial fluorescence measurement

of each cell.

4.3 Results

4.3.1 Instrument validation and subcellular measurements

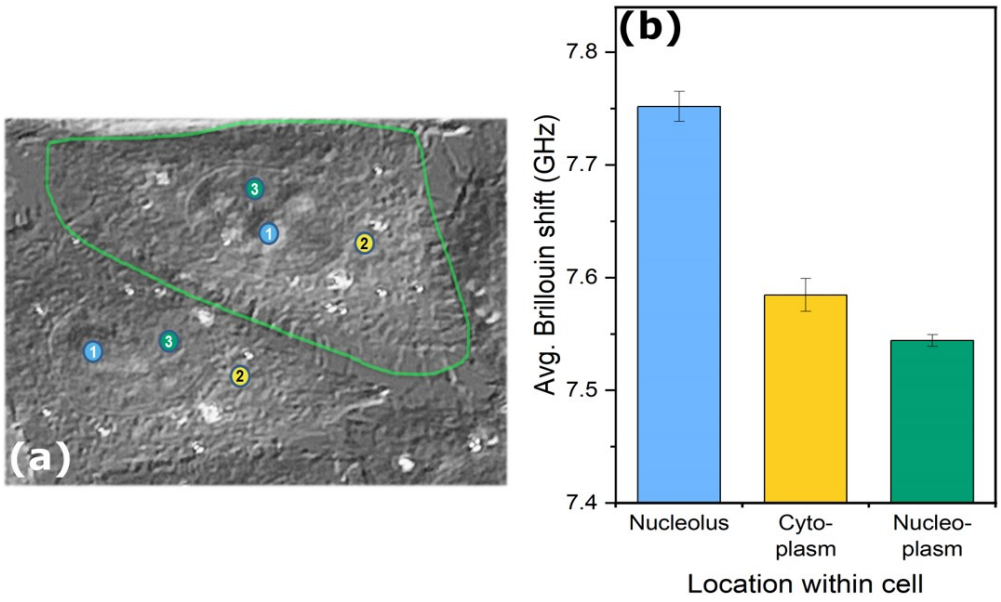

Figure 4.4: Cellular components and Brillouin frequency shifts. (a) DIC image of CHO-K1 typical cells with indicators for (1) nucleolus, a very dense DNA-rich environment that is mostly isolated from the rest of the cell, (2) cytoplasmic region that is strongly related to cell mechanics and stability, dense with complex micro and nano scale structures, and (3) a "middle ground" between the (1) and (2) inside the cell nuclear envelope, and the targeted "nucleoplasm" region. (b) The average Brillouin frequency shift ν_B measured from each of the three subcellular component targets.

The confocal Raman-Brillouin microscopy setup allowed for spectral measurements with sub-micron scale resolution, providing observations of time-resolved changes at the subcellular level. The subcellular imaging capabilities are demonstrated in the bottom panel of Fig. 4.1 as well as Fig. 4.6. Spectra were collected from three target regions within CHO-K1 cells to verify the system capability for distinguishing between individual subcellular components. The three target regions were a generalized cytoplasmic region (anywhere within the cell membrane that was outside of the

perinuclear region), a nucleoplasmic region (inside the nuclear membrane excluding nucleoli), and finally the nucleoli. An initial comparison showed that all components within the cell had a greater Brillouin frequency shift as compared to the surrounding media. Furthermore, the peak linewidth, measured as full-width half-maximum (FWHM) of the Lorentzian fit exhibits a broadened shape caused by phonon damping processes that is expected in spectra acquired from microscale heterogeneous materials such as cells [49, 90, 47, 167]. The mean Brillouin frequency shift of each region across all cells measured was found to be 7.723 $\pm$ 0.011 GHz, 7.583 $\pm$ 0.007 GHz, and 7.518 $\pm$ 0.012 GHz (N = 19, 35, 23) for cell nucleoli, cytoplasm, and nucleoplasm regions respectively, with error presented as standard error of the mean (SEM). The average linewidth across sample volumes measured 1.909 $\pm$ 0.017 GHz 1.820 $\pm$ 0.017 GHz 1.718 $\pm$ 0.011 GHz respectively, indicating that the individual components also have measurably different viscosity. The nucleoli were measured to have significantly higher Brillouin frequency shifts than the other primarily-protoplasm areas. A DIC image of a typical CHO-K1 cells with indicators for the targeted regions are shown in Fig. 4.4 alongside a bar plot of the averaged Brillouin frequency shift measurements from each component.

Raman spectra were acquired during all trials to provide validation of cell targeting and to monitor the focal volume during experiments. A comparison of the first Raman spectra with the last of each sample also provided a means of analyzing any major chemical changes within the measured area as result of the external stimulus. After background subtraction, spectral comparison between an average of the first and last three spectra from select samples revealed no noticeable differences in Raman peak intensities or peak ratios within the fingerprint region across all compared spectra. Examples of the Raman spectra collected from the three subcellular target regions are provided in Fig. 4.5

Finally, we performed a small section raster scan in the two lateral dimensions to generate a two-dimensional Brillouin map of cell mechanical properties. A resultant Brillouin mapping image, shown in Fig. 4.6, provides a good indication that the measurements from individual component shown in Fig. 4.4 are correct, as the 2D map provides clear visual confirmation of the

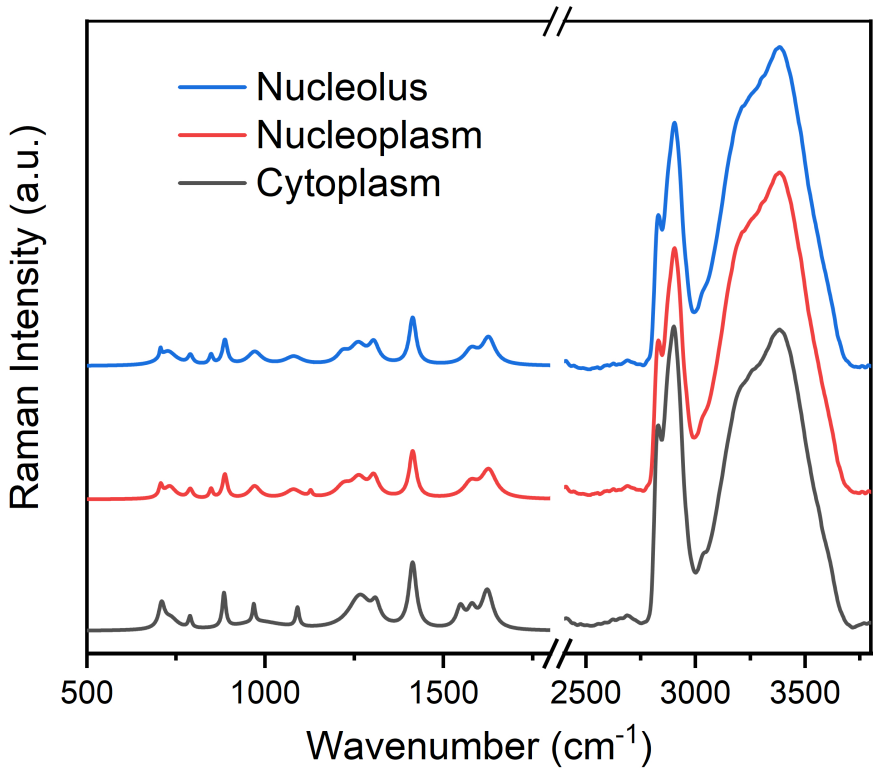

Figure 4.5: Individual examples of Raman spectra collected from the different target regions within CHO-K1 cells. A five-point moving average filter has been applied to spectra in this plot for presentation purposes.

relative Brillouin frequency shifts and intracellular heterogeneity. Most notably, we can see the boundary created by the nuclear envelope that separates the nucleoplasmic and cytoplasmic regions of the cells. Furthermore, our data and mapped image agree with recent reports regarding the relative densities of cells and their subcellular components [164, 189].

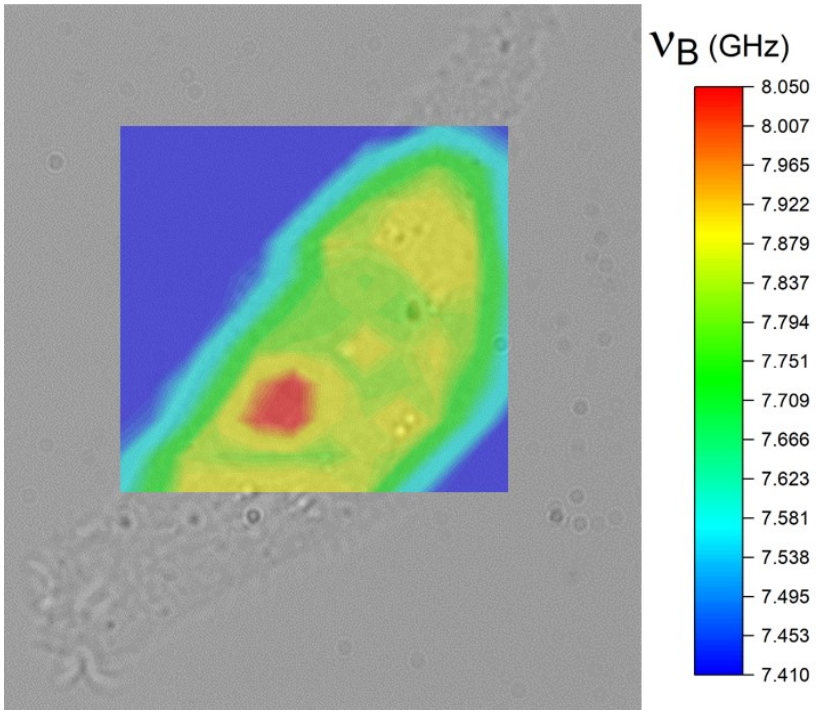

Figure 4.6: 2-Dimensional mechanical mapping with Brillouin spectroscopy. 10×10 μm mechanical properties map from CHO-K1 cell, cropped from a 20×20 μm image generated by X-Y axes raster scan with 1μm step size. Brillouin image was generated using OriginLab contour plot feature using ν_B magnitude at each point per individual pixel. Cell nuclear envelope is distinguishable from surrounding cytoplasm with a clearly defined nucleolus.

4.3.2 Fluorescence microscopy: membrane and cytoskeletal disruption

4.3.2.1 Membrane permeabilization and YO-PRO-1 uptake

YO-PRO-1 uptake was observed for various nsPEF intensities to verify membrane permeabilization. YO-PRO-1 uptake is indicated by an increased fluorescence emission from within the cells, an example of which is shown in Fig. 4.7. We observed a dose-dependent response for YO-PRO-1 uptake with increasing nsPEF intensity. Minimal nsPEF threshold for YO-PRO-1 uptake was observed to be $\sim$3 kV/cm. While we did not acquire images long enough to see a complete plateau of fluorescence intensity and membrane resealing and recovery, we did observe an asymptotic behavior. These results are as expected and indicate that the cell membrane is being disrupted by the nsPEF stimulus [26, 179]. Likewise, there is a direct correlation between field intensity and cell membrane permeability as indicated by dye uptake.

4.3.2.2 nsPEF induced cytoskeleton change: actin and microtubules

DIC and fluorescent image series were acquired over a period of five minutes following exposure to nsPEF. Accompanying z-stack images were acquired both before and after the time-series acquisitions. Fluorescence intensity and standard deviation measurements were acquired from randomly selected cells following application of a single nsPEFs stimulus. Cells were randomly selected with no preference for morphology or size and exhibited a wide range of visible changes in response to nsPEF stimulus (some cells responded very violently, developing large bleb formations and extreme swelling, while others appeared to contract). We did not attempt to characterize the volumetric changes from cells during this study, but rather exempted cells with extreme swelling and blebbing from further signal processing and data analysis and excluded them from this study. Such cells often had large fluctuations in their Brillouin frequency shift measurements due to cell motion and respective measurements being across membrane or bleb interfaces. Less than 10% of cells were excluded by these criteria. Anecdotally, we observed that cells with more rounded features appear more susceptible to morphological changes such as blebbing and swelling. Additionally, of the cells that exhibited visibly apparent contractility, most were observed contracting

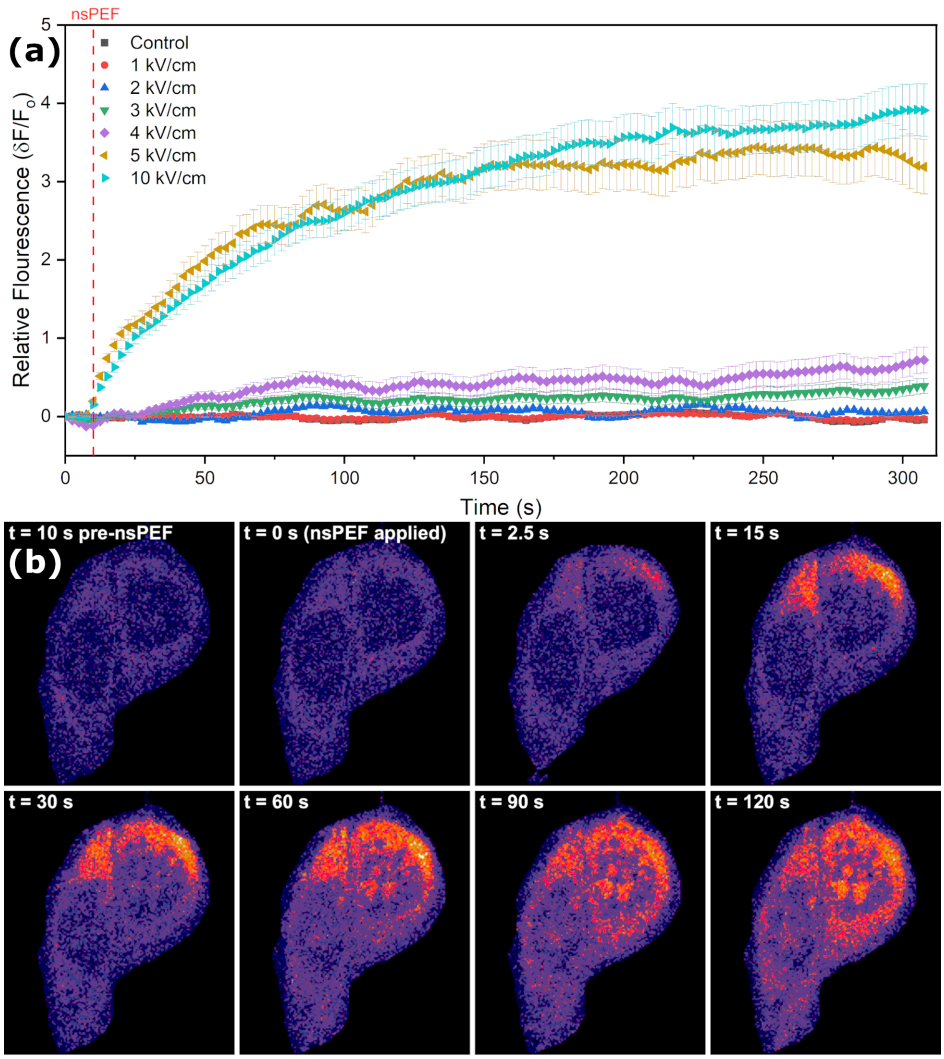

Figure 4.7: YO-PRO-1 dye uptake. (a) Relative fluorescence measurements against time after exposure from YO-PRO-1 dye uptake in cells exposed to nsPEF intensities from 0 kV/cm to 10 kV/cm. (b) Example image series of dye uptake, showing time evolution of dye influx into the cell. Dye influx shows a strong indication toward the cathode side of the electrode (toward the top of the image).

along the basal layer of cells with a more elongated structure as those cells began to swell vertically.

The most notable observation from fluorescent imaging investigations came from the α-actinin fluorescence series. Figure 4.8(a) provides an example of frames from a time series recording with DIC and respective fluorescence images from α-actinin labeled CHO-K1 cells. The first frame provided was the image acquired immediately after nsPEF stimulus. Further frames extend to four minutes following nsPEF stimulus. Frames from the initial ten seconds prior were omitted, as

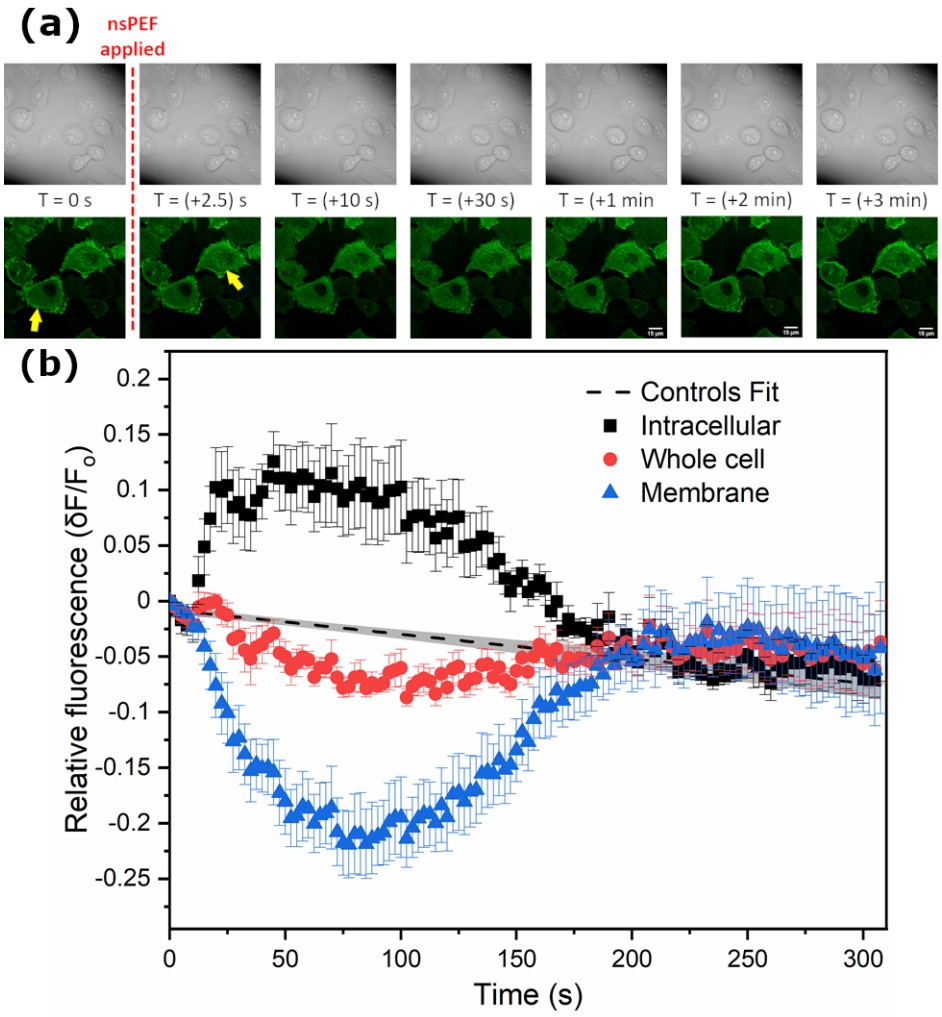

Figure 4.8: Fluorescence time series: α-actinin. (Top – a) DIC and fluorescence time series images of cells. Yellow arrows indicate locations where membrane and intracellular fluorescence change is easily visualized. (Bottom – b) Average relative fluorescence $\delta F/F_o$ measured from the whole cell (region of interest (ROI) encompassed entire cells, tracing along the outside of cell membranes), the cell excluding the membrane (ROI traced along inside of cell membrane), and the cell membrane only (annular ROI, allowing measurement between the first two traced regions). Data series depicts the decrease in membrane bound cortical actin with correlated increase in intracellular misaligned actin.

they provided no additional information. Analysis of images taken just above the cell basal layer showed a rapid decrease in cortical actin fluorescence as well as an increase in intracellular fluorescence from what is presumed to be diffuse, misaligned, and fragmented fibers that moved toward the center of cells immediately following nsPEF stimulus. Image series indicate that a reduction

in cortical actin fluorescence started as early as 2.5 seconds after nsPEF application. Most cells showed a sudden and substantial reduction in membrane fluorescence, with a noticeably higher fluorescence intensity from diffuse actin throughout the whole cell. The observed average change in fluorescence intensity reached its maximum over the 30 to 45 seconds following nsPEF application, after which the fluorescence distribution began to return to previous arrangement, leaving bright actin spots throughout parts of the cell. Figure 4.8(b) provides an example of the relative fluorescence ($\delta F/F_o$) measurements recorded from intracellular actin and membrane actin following application of a 15 kV/cm stimulus. The observed process indicates that a rapid change occurs in the actin network of cells immediately following application of the nsPEF stimulus and provides a reasonable expectation that the mechanical properties of the cell are changing. Stress fibers could be visually inspected along the basal layer of the cell at the glass substrate interface. The basal layer showed a reduction in fluorescence intensity following the same trend as when focused further above, however, the stress fibers can be seen to remain intact and mostly unchanged.

Time series images of microtubule fluorescence revealed an overall decrease in fluorescence intensity following nsPEF stimulus, likely attributable to depolarization. This attribution is drawn through comparisons of z-stack image series acquired pre- and post-exposure, and because no changes were readily observable in the microtubule network following nsPEF exposure. The z-stack images did indicate some cell swelling and microtubule rearrangement; however, the changes in the microtubule network took much longer than all other processes ($\geq$ 10 minutes). Microtubule rearrangement was most commonly indicated by a change in fluorescence intensity (microtubule density) moving from the lower half of the cell toward the top of the cell as the cell swelled. An X-Y axis view of cells before, and 10 minutes after nsPEF exposure is shown in 4.9(b). Furthermore, an image subtraction using Z-projection of brightest points with that of 5 minutes post-exposure from pre-exposure, shown in Fig. 4.9(a), indicates little to no loss of microtubule filaments. Differences between these two images are likely that of standard microtubule motions within active cells. In some more extreme cases, following the greater intensity $\geq$ 15 kV/cm electric field stimulus conditions that led to severe cell swelling, the microtubule structures sometimes appeared to

depolymerize or fragment. This particular response, however, was inconsistent and could not be directly attributed to nsPEF exposure itself rather than severe cell swelling.

The drastic changes and redistribution of actin fluorescence, alongside the minimal differences observed in microtubule fluorescence indicate that, within the time frame of our Brillouin spectroscopy investigations ($\leq$ 90 seconds following nsPEF exposure), any changes observed in cell mechanical properties are likely a result of actin filament and network disruption, not changes in microtubule structures.

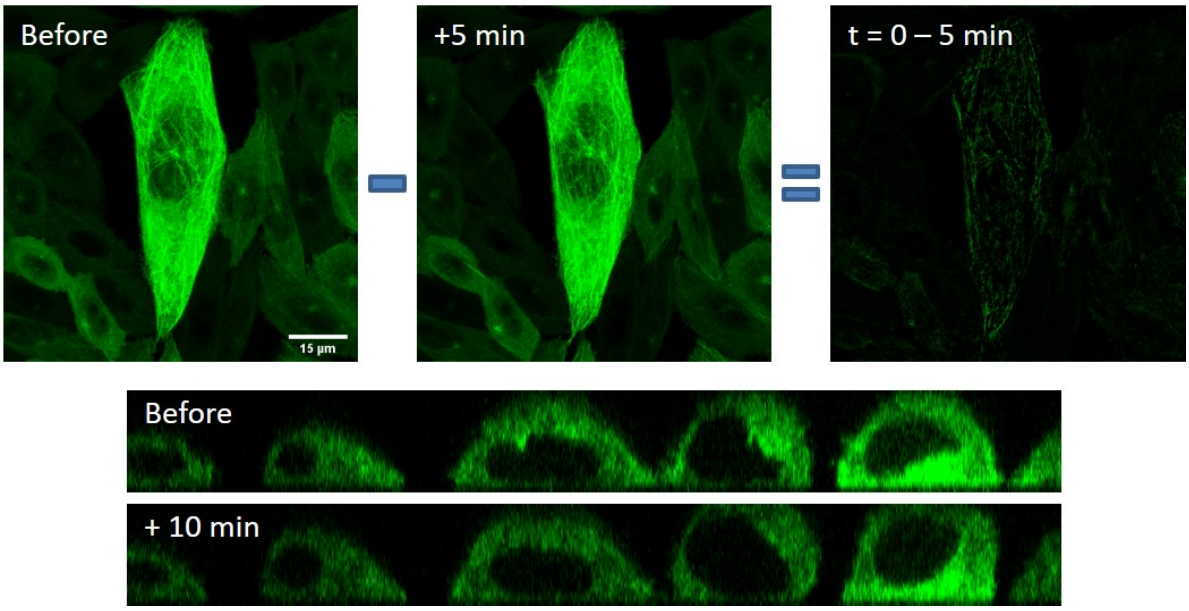

Figure 4.9: Fluorescence imaging: microtubules. (Top) Z-projection of brightest points generated using ImageJ for pre-nsPEF exposure (left) and 5 minutes post-exposure (middle), with image subtraction of post exposure from pre-exposure (right) to indicate differences in microtubule structures. (Bottom) Orthogonal X-Z image slice from cells before, and 10 minutes post-nsPEF exposure indicate cell swelling and microtubule rearrangement.

4.3.2.3 Cell mechanical properties and response to nsPEF

Results of the Brillouin spectral time series measurements from the cytoplasm, nucleoplasm, and nucleoli regions of cells are shown in Fig. 4.10(a). All cases exhibit a distinct asymptotic

decreasing trend in Brillouin shift magnitude following application of the nsPEF stimulus. Analyzing the chart, we notice changes in the Brillouin frequency shift, and thus longitudinal modulus almost immediately following the nsPEF stimulus (red dash line). The graphs provided in Fig. 4.10(b-d) depict the mean percent change in the Brillouin shift measured from each of the three regions after nsPEF stimulus at intensities of 10, 15 and 20 kV/cm and 0 kV/cm control. Not only did the nucleoli present the overall greatest magnitude Brillouin frequency shift of the three target regions, but the nucleolus also exhibited the smallest overall change in magnitude after the external stimulus was applied. We observed an average reduction in Brillouin shift magnitude of $\Delta\nu_B$ = 2.168 $\pm$ 0.119, 1.664 $\pm$ 0.160, and 0.771 $\pm$ 0.360 percent for cytoplasm, nucleoplasm, and nucleolus, respectively at our greatest nsPEF intensity of 20 kV/cm. The reduction in Brillouin shift corresponds to an overall increase cell mechanical compliance (reduction of longitudinal modulus) [111] and is consistent with expectations derived from previous AFM measurements showing a reduction in Youngs modulus of CHO-K1 cells after nsPEF exposures [22]. Furthermore, the respective difference in magnitude of Brillouin frequency shifts from pre- and post- nsPEF exposure shows a direct relationship to each position within the cell. This indicates that the intra-cellular regions may exhibit different susceptibilities to various parameters of this stimulus, and thus exhibit less of a change under this specific exposure. Alternatively, this difference in Brillouin frequency shift reduction could simply be a result of the various cytoskeletal connections, as the cytoplasm region measured would likely be more strongly impacted by membrane-level and actin disruptions, as the actin cortex has already been shown to undergo significant changes in the previous section. A discussion relating cytoskeletal disruption and reduction in magnitude of Brillouin frequency shift is addressed further in the following discussion section of this chapter.

4.4 Summary and discussion

Measurement of cell and subcellular mechanical properties and their changes in response to a non-specific external stimulus were demonstrated. These results provide further support for Brillouin spectroscopy as a potential tool in biomedical studies and clinical applications. Brillouin and Raman spectra were simultaneously recorded from three subcellular regions within CHO-K1

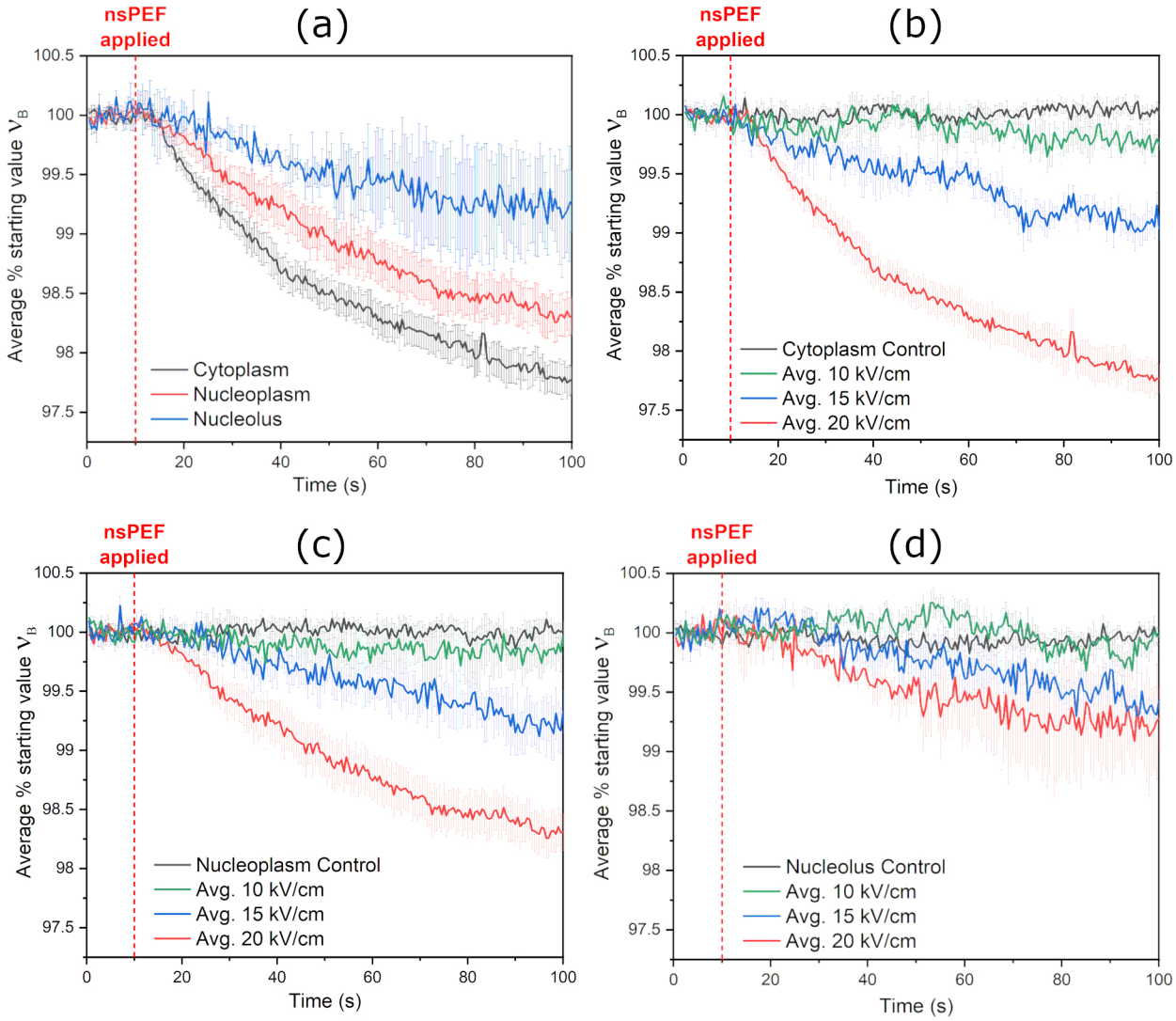

Figure 4.10: Changes in cell mechanics: Brillouin spectral time series measurements. (a) Results of the averaged Brillouin spectral time series measurements from each of the three regions at the most extreme nsPEF intensity used (20 kV/cm), indicating that the cytoplasm shows the greatest change in response to nsPEF. (b)-(d) Results for cytoplasm, nucleoplasm, and nucleolus measurements, respectively, at nsPEF intensities of 10, 15 and 20 kV/cm against controls.

cells 10 seconds before and 90 seconds immediately following application of a short duration (600 ns) electrical stimulus.

nsPEF stimulus is known to induce a wide range of complex biophysical reactions with uncertain outcomes that chemical or drug treatments cannot provide. Furthermore, the field intensities

used in this study ($\leq$ 20 kV/cm) do not significantly alter the physiological environment (in this case, the surrounding culture media) of the cell [173]. Therefore, nsPEF provides a fast, non-specific, and transient stimulus ideal for testing our hypothesis that Brillouin spectroscopy could be used to measure and observe subcellular mechanical property dynamics. Finally, PEFs have become an important scientific and clinical tool, finding applications in several cancer treatment therapies [190, 191], gene electrotransfer techniques [192, 193], and even in food treatment and processing [194] indicating that our results could be of interest across a variety of fields.

Upon starting our investigation, our working hypothesis was that Brillouin spectroscopy could be used to measure and observe the dynamic changes in cell mechanical properties induced by such a stimulus, and that a reduction in Brillouin frequency shift, i.e., longitudinal modulus would follow stimulus application. Motivation for this study was derived from previous reports of nsPEF induced changes in the cytoskeleton [172, 195, 179], AFM-based reports of nsPEF-induced reduction of cell stiffness [22], and a recent publication relating cytoskeletal structure changes to cell nuclear mechanics [167].

Our hypothesis, that we would observe a decrease in magnitude of the Brillouin frequency shifts is supported by our data. An overall reduction in Brillouin frequency shift following nsPEF stimulus was observed across all three target regions of the cells with response having a direct dependence on the stimulus field-intensity. While subtle changes were observed in fluorescence images of both actin and microtubule structures, we conclude that changes in the actin network are the primary driver of this reduction in shift magnitude. Data provided in a recent report by Zhang et al. supports this conclusion [167]. These results lead us to believe that the primary mechanism driving the changes that we observed are that of actin disruption and rearrangement as well as cell swelling, not changes in the microtubule network.

4.5 Conclusions

The work presented in this chapter demonstrates the capability of Brillouin spectroscopy and microscopy to assess subcellular biomechanical properties and how they change in response to a fast, non-specific, transient external stimulus. The data presented here indicate that the indi-

vidual subcellular components measured: cytoplasm, nucleoplasm, and nucleoli exhibit not only characteristically different properties, but also different responses to the applied stimulus. For instance, stiffness of the cytoplasmic regions, as measured by Brillouin frequency shift, experienced a greater magnitude reduction than that from within the cell nucleus. By contrast, the nucleoli did not exhibit such significant changes in stiffness, even compared against measurements from within the rest of the nuclear envelope. Furthermore, we observe that the changes in mechanical properties occur quite rapidly following the nsPEF application but take between 2 and 5 seconds to be measurable beyond one standard deviation of the mean and are not instantly observable. The reduction in Brillouin frequency shift are, however, observable long before cell swelling can be seen via standard microscopic imaging techniques. This suggests that Brillouin spectroscopy is more sensitive to micromechanical changes than standard measurement and observation methods. These results are supported by fluorescence imaging time series that indicate a drastic reduction in cortical actin along the cell plasma membrane, as well as an increase in fluorescence from disordered and diffuse actin within the cytoplasmic region of the cell. This outcome is consistent with our expectations, as nsPEF stimulus has been shown to disrupt the cell membrane, which leads to further downstream disruption of other cytoskeletal structures in the actin cytoskeleton and microtubule network. Our results also agree with previous reports indicating that depolymerization of the actin network should lead to greater changes in the cytoplasmic region of cells as compared to the nucleus and nucleoli, where actin is not present [111], and as well that disruption of the actin cortex should lead to reduced stiffness from within the nucleus of cells [167]. These results validate Brillouin spectroscopy as a technique for *in vitro* investigation of cellular and subcellular mechanical properties, and their changes over time or in response to external stimuli.

Lastly, though we postulate that pulsed electric fields are felt by cells as mechanical forces, we have previously determined that nsPEF can produce mechanical pressure waves when submerged in cell solutions. We must decouple the mechanical from electrical insults to develop a full understanding of how each component impacts cell function and properties. Therefore, we engineered a system capable of producing laser induced breakdown, generating pressure waves that originate at

a specific distance from cells of interest. These pressure waves are then independent of an nsPEF, allowing us to isolate the impact of rapidly applied mechanical forces on the cell membrane. The following chapter discusses how we used this engineered system to discover an interesting synergistic behavior between nsPEF and ps optical pulses that allows for initiation of breakdown events at reduced optical pulse energies in biologically relevant liquids.

5. SYNERGY IN BREAKDOWN: OPTO-ELECTRICAL BREAKDOWN THRESHOLDS *

Optical breakdown phenomena and the ionization processes that drive it have been thoroughly investigated since first being described by Keldysh [197, 198] and have found use in a wide range of applications from investigative spectroscopy techniques to commercial micro-machining and nano-scale surgeries. Despite extensive experimental and theoretical research, efforts are still being made to understand, describe, and model the interplay of the complex mechanisms and the dynamics of optical breakdown phenomena under varying conditions. This chapter presents the experimental procedures and supporting theoretical model for a synergistic effect that was observed between short picosecond optical pulses and nanosecond pulsed electric fields. Throughout this chapter nsPEFs are referred to as "nanosecond electric impulses" or nsEP. This difference in terminology can serve to differentiate between studies performed with cell exposures (nsPEF) and those focused only on interactions between the optical and electrical pulses.

5.1 Introduction

Dielectric breakdown phenomena, and its driving physical processes have been the subject of extensive experimental studies and theoretical models [198, 199, 200, 201, 202, 203]. Such studies have revealed the complex physical processes that drive breakdown, i.e. ionization and how those processes depend on a range of material properties and electric field application. [204, 205, 206, 207, 208, 209].

The effect of electric fields on ionization properties including direct interactions with solvated electrons, band-gap modifications, thermal ionization, and electrical ionization of shallow donors has been the focus of many investigations [210, 211, 212]. However, potential synergy in breakdown mechanisms under varying experimental conditions remains relatively unexplored [213, 214, 215, 216]. One paper of interest by Gorshkov, et al. reported a successful reduction

*Portions of this chapter are reprinted with permission from "Synergistic effect of picosecond optical and nanosecond electrical pulses on dielectric breakdown in aqueous solutions by Coker, Z C, Liang, X-X, Kiester, A S, Noojin, G D, Bixler J N, Ibey, B L, Vogel, A, Yakovlev, V V, 2021. Photonics Research, 9, 3, 416-423, Copyright 2021 Chinese Laser Press [196]

in breakdown thresholds using crossed UV and IR lasers in alkali halide crystals [217]. While this paper demonstrated that a combination of electromagnetic fields can influence breakdown, minimal attention has been given to low-frequency and DC electric field effects on optical breakdown thresholds, particularly in biologically-relevant media. Electric fields have been utilized to increase laser induced emission spectra after optically induced breakdown [218]; however, the presence of externally applied electric fields before or during optical breakdown initiation has often been neglected. Limited efforts focused on interactions of DC electric fields on optically induced breakdown, described in two distinct reports [219, 220], arrived at contradictory conclusions. Furthermore, a more recent report also focused on the influence of DC electric field effects on laser induced breakdown in gasses by Takahashi, et al. [221] provides further support for the results reported by Mullen, et al. reporting an increase in optical pulse energies required to achieve breakdown in gases under the influence of DC electric fields. While Mullen and Takahashi present arguments akin to those of Tulip and Seguin in 1976 [222], that charged particles and free electrons are removed from the focal volume by the electric field. Each of these investigations were limited to gaseous media, which have different diffusive properties and much larger inter-molecular distances than condensed states [223]. A detailed understanding of the opto-electrical breakdown processes, the underlying physics, and how to tightly control them is critical to further developing many new and evolving technologies, particularly in the fields of spectroscopy, micro-machining, and many emerging medical applications.

Past experiments and models based on density functional theory have demonstrated a direct field-dependence for molecular ionization potentials and excitation energies in dielectrics under strong electric field conditions[212, 224]. While the electric fields discussed in these reports ($10^9 - 10^{10}\ V/m$) are well above the dielectric strength of any biologically relevant aqueous solutions ($10^8\ V/m$) [210], the underlying fundamental physics does not change; electrons and ions are still driven by the presence of an external field. Therefore, we hypothesized that we could decrease the effective energy required for a picosecond laser pulse (psLP) to achieve optical breakdown visualized via bubble formation in aqueous solutions through the application of an external

500 ns electrical impulse (nsEP) at the focal volume of the laser (well below the normal dielectric breakdown threshold). In this chapter, we establish an experimental setup to examine the influence of external electric field impulses on optical breakdown thresholds in biological-relevant media. We then provide an explanation of and support for our results through a theoretical opto-electrical breakdown model. We, therefore, introduce a synergistic effect that has yet to be thoroughly investigated or employed using two technologies that are already prevalent in biomedical sciences: nanosecond pulsed electric fields and picosecond laser-induced optical breakdown. This synergistic effect has wide range for potential use in studies of fluid dynamics and for biomedical applications.

5.2 Experimental methods, theory, and design

The band structure of water, and other biological solutions is of critical importance for understanding breakdown behaviors and is the basis for the theoretical modeling provided in this chapter. While for many dielectrics the band structure is fully characterized by the energy gap E_{gap} between valance band (VB) and conduction band (CB) electrons, water exhibits an intermediate energy level, E_{solv}, between these bands. Recent studies have revealed the band gap of water to be about 9.5 eV with the intermediate energy level located at 6.6 eV above the VB [208, 209]. The existence of this intermediate level is due to the network of weak hydrogen bonds between water molecules, in which thermal fluctuations can produce favorable constellations for electron abstraction from excited molecules. These intermediate levels are known as "preexisting traps" and have a number density of about $n_{trap} \sim 10^{19}\ cm^{-3}$. Furthermore, for ultrashort laser pulses, the effective ionization potential, $\widetilde{\Delta}$, the total energy required to excite electrons from the VB to the CB needs to be considered, which takes into account both the band gap and oscillation energy of electrons in the laser electric field [198, 209, 225, 226].

A generalized schematic of aqueous media band structure and associated electron excitation and multiplications during the breakdown process is provided in Fig. 5.1(a) alongside a schematic of the experimental setup Fig. 5.1(b), and example of breakdown threshold for each tested sample

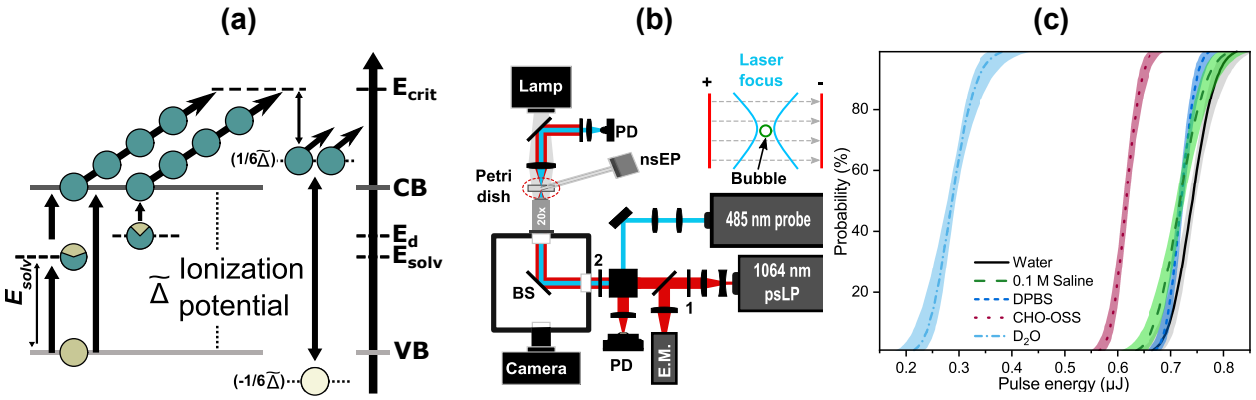

Figure 5.1: Experimental design. (a) Tentative band structure of biological solution and plasma dynamics during the optoelectrical breakdown process. (b) Schematic representation of opto-electrical breakdown setup for bubble formation and detection with red indicating 1064 nm beam path and cyan indicating 485 nm probe beam path. Abbreviations indicate polarizing beam splitter cube (PBS), beam splitter (BS), pulse energy meter (E.M.), dichroic beam splitter (DBS), 750 nm short pass filter (SPF), and photodiodes (PD). Numbers 1 and 2 indicate respective (l/2 λ) wave plates, and 20x 0.4 NA microscope objective (c) Probit analysis curves and 95% confidence intervals of breakdown threshold (E_{th}) measurements across various biologically relevant sample solutions (MiliQ Milipore 18 MW·cm water, 0.1 M saline solution, DPBS, physiological imaging buffer, and D_2O).

Fig. 5.1(c)[2]. Breakdown initiation in water is likely to occur via excitation of a VB electron into a solvated state, followed by rapid excitation into the conduction band. For impurities in water or energetic molecules in biological medium, exogenous donor electrons from these substances can be doped into the intrinsic band gap of water to form an additional excitation channel with reduced energy, E_d, below the CB. The number density of this channel, n_d, depends on the concentration of exogenous donor electrons that is reflected by the molar concentration of biological medium. This concept of treating water as an amorphous semiconductor was first proposed by Williams et al. [227]; the additional excitation channel differs from E_{solv} in that donor electrons are readily available for excitation into the CB at the E_d level, whereas E_{solv} level electrons need to be excited from the VB first and then upconverted into the CB. Electrons in the CB can readily absorb energy from the laser via inverse Bremsstrahlung absorption (IBA). IBA is a process whereby electrons can gain kinetic energy through absorption of photons. As the kinetic energy of the electrons

[2]Additional and more specific detail related to the experimental setup is provided in Appendix C

increases, they eventually reach a critical energy level, sufficient for ionizing other nearby electrons through collisional processes ($E_{crit} \geq 3/2\widetilde{\Delta}$ for parabolic band gap [213, 225]). The residual energy from impact ionization between two electrons is distributed between the initial high-energy electron, the new electron, and the resulting hole from the newly promoted electron. This process thus provides two electrons in the conduction band that may then also undergo IBA and ionize even more electrons in a cascading effect and is referred to as cascade or avalanche ionization (AI). Linz, et al. demonstrated that AI primarily drives the breakdown process for laser pulse duration down to 250 fs, but that the initiation channel is primarily determined by laser pulse parameters and intermediate energy states, with an increasing ratio of carrier density provided by AI over strong field interactions (SFI) with increasing wavelength and pulse duration [209]. E_d is generally smaller than E_{solv}, in biological media when an electric field is applied, donor electrons that already exist at E_d can tunnel through the potential barrier into the CB and serve as additional seed electrons to support the AI process [228].

5.2.1 Opto-electrical breakdown modeling

A single rate equation (SRE) model previously developed by Liang, et al. [226] was employed to simulate breakdown conditions. This SRE model uses an asymptotic regime approach like that derived by Rethfeld [213] but was derived from a simplified energy splitting scheme, compared to Christensen and Balling [215], that accounts for conservation of energy among post-collision particles. The avalanche ionization rate in the asymptotic regime has a closed form $\eta_{AI} \approx ln(2)\sigma_{1pt}I/E_{crit}$ where σ_{1pt} is the cross section of inverse Bremsstrahlung absorption and I is the transient irradiance. The maximum AI rate induced by the Gaussian psLP at its peak irradiance ($I = 5.4 \times 10^{15}\ W/m^2$) in Fig. 5.3(b) is $3.2 \times 10^{12}\ s^{-1}$, whereas the AI rate induced by the nsEP approximated by a 10 μm laser pulse with equivalent electric field strength is $1.3 \times 10^{8}\ s^{-1}$.

This simplified scheme is justified since the asymptotic conditions are fulfilled [226]. More specifically, as determined by Liang, et al. [226] for pulse durations longer than 250 fs (asymptotic regime), the complex multi-rate equation that is generally used to describe inverse Bremsstrahlung absorption and impact ionization can be simplified into a single rate equation. Since the pulse du-

ration in this study is much longer than 250 fs, we chose the asymptotic single rate equation for our optical breakdown model. Additionally, we have extended the model to include an AI contribution term to account for the nanosecond electrical impulse in Eq. 5.1. Electron recombination processes and diffusion out of the focal volume are critically important for picosecond pulse duration and mandatory for longer nanosecond duration; therefore, two additional loss terms are added to account for contributions of recombination and diffusion rates in the target media.

$$\frac{dn_{total}}{dt} = \dot{n}_{SFI}\frac{n_{val}}{n_{bound}} + (\eta_{AI,asymp} + \eta_{AI,DC})n_{total}\frac{n_{val}}{n_{bound}} - \eta_{rec}n_{total}^2 - \eta_{diff}n_{total} \tag{5.1}$$

The first term on the right-hand side of the equation represents the contributions from laser strong field interactions ($\dot{n}_{SFI}$). This term considers the laser-driven excitation of VB electrons to the CB across the entire band gap, E_{gap}, via intermediate level E_{solv} through both multiphoton and tunneling ionization. These ionization rates depend on wavelength, electric field intensity, and band gap as described by the well-known Keldysh formula [198]. Terms $\eta_{AI,asymp}$ and $\eta_{AI,DC}$ denote the avalanche ionization rate for the SRE asymptotic regime for a single laser pulse, and the avalanche ionization rate for the electric impulse, respectively. For a more detailed formulation and derivation of the $\dot{n}_{SFI}$ and η_{AI} terms, the reader is referred to Liang, et al. [226]. The terms n_x denote the number density of charge carriers, with specifying subscripts x indicating: total, valence, and bound, with $n_{val} = n_{bound} - n_{total}$, and the ratio n_{val}/n_{bound} denoting the potential for a depleted valence band in the ionization process. Since the donor electron level is unknown, tunneling of donor electrons by external electric field into the CB is simplified as a background electron density, n_{back}, that approaches the number density of donor electrons, n_d. Finally, η_{rec} and η_{diff} denote losses from electron recombination and diffusion, respectively. Diffusion in polar liquids is very different from diffusion in gases [229]. In polar liquids, the external field from the positively charged ions and from the surrounding polar environment slow down the diffusion of electrons and leads to a reduced ambipolar diffusion coefficient, η_{diff} [223]. In this paper, we use

$\eta_{diff} = 1/\tau_{diff}$ corresponding to diffusion time τ_{diff} = 10 ns, $\eta_{rec} = 1.8 \times 10^{-9}\ cm^3 s^{-1}$ [209] and $n_{bound} = 6.68 \times 10^{22}\ cm^{-3}$ for number density of bound electrons that can be ionized in pure water. The model can, in general, simulate optical breakdown induced by any two wavelength laser pulse combinations with adjustable inter-pulse interval. Additionally, we can effectively "turn off" the contributions from either the psLP or nsEP by setting their individual components to zero. With this in mind, we modeled the contribution from DC electric field impulses via the IBA rate of a 10 μm wavelength laser pulse, as DC breakdown threshold is very closely reflected by that of long wavelength laser pulses such as those from a CO_2 laser pulse [210].

We note that within our model, the band gap and energy level modifications provided by the DC electric field are neglected. This is because, even in the case of our greatest field intensity of 40 kV/cm, the reduction of the band gap E_{gap} is quite small. The band gap reduction is described by Eq. 5.2, as provided by Keldysh while discussing the Keldysh-Franz effect [197].

$$\Delta E_{gap} = [(eE)^2 \frac{\hbar^2}{m_{ll}}]^{1/3} \tag{5.2}$$

Where, e is elementary charge, $\hbar$ is the Dirac constant, and $m_{||}$ is the effective mass of an electron and hole. Taking $E = \ 40\ kV/cm$ and $m_{||}$ as the mass of an electron, we obtained $\Delta E_{gap} = 0.01\, eV$. This value is marginally small when compared with the band gap of water $E_{gap} = \ 9.5\, eV$ and is therefore negligible. Further evidence is provided by findings of Zhu, et.al. where simulation results showed a reduction in the band gap of amorphous SiO_2 of only 0.2 eV under an above-threshold static electric field of $10^{10}\ V/m$.

5.2.2 Opto-electrical breakdown thresholds E_{th}

We used our opto-electrical breakdown model to validate and explain experimental observations against our hypothesis. A schematic of the experimental setup is presented in Fig. 5.1(b). We used a 1064 nm, 14 ps laser (APL-X 1064-532; Attodyne Inc. Toranto, Ontario) to initiate breakdown, which was chosen to exclude direct absorption of light by biological molecules increasing the overall dependence on AI in the breakdown and bubble formation process [209]. The

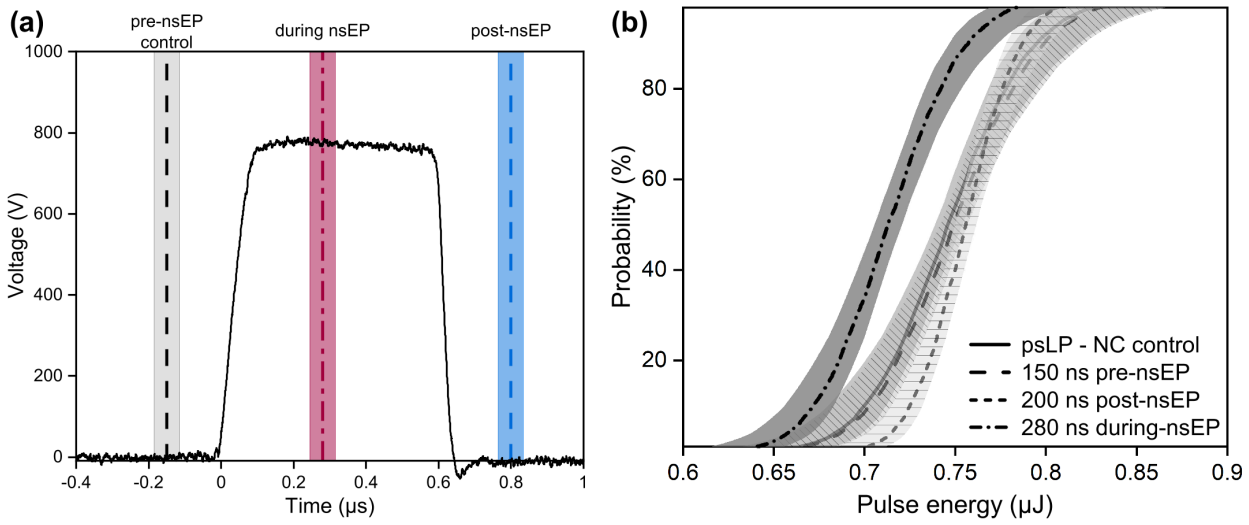

Figure 5.2: Pulse timing and threshold dependence. (a) nsEP electrical impulse trace (40 kV/cm) and relative timing between of psLP pulses to nsEP. (b) Probit analysis curves from respective time points and control validation.

laser spot at the sample volume was estimated near the diffraction limit, with an approximate spot radius of 1.33 μm and Rayleigh length of 7.8 μm, providing a fairly small interaction volume of roughly $V_{plasma} = 14\ \mu m^2$. A 485 nm probe laser with 0.4 mW average power was co-aligned and focused to a photodiode after the sample for breakdown detection. Breakdown events distort the focal volume of the laser and thus are detected as fluctuations in signal intensity measured at the photodiode. A pair of tungsten electrodes were centered about the laser focus, 200 μm above the cover glass of a petri dish. The nsEP system has been described previously [172] and provided a trapezoidal profile electric field with approximately 100 ns rise time, 500 ns working time, and 30 ns fall time for the delivered impulse. All electrical and optical pulse timing was controlled by a pulse delay generator (DG535; Stanford Research Systems, Inc.). The DC field intensities were well below the dielectric breakdown threshold for the target media, no arcing or direct electric breakdown phenomena was observed, and all breakdown events were limited to that of optical breakdown regime. The tungsten electrodes were, however, located within the field of view of the microscope and thus were easily observed during and inspected after each series of experiments via digital camera. No visible damage was detected on the electrode surfaces throughout this study.

Furthermore, the cell culture dishes used to hold the sample volumes were designed for optical imaging of biological targets for extended duration using blue wavelengths and were replaced often. The measured intensity for the 485 nm probe beam did not decrease through the entirety of the experiments indicating that no color centers or other defects were observed that would distort or decrease light transmission and breakdown detection or reduce pulse energy delivery to the sample.

Breakdown threshold energies (E_{th}) were determined by recording bubble formation for each laser pulse from sub-threshold to super-threshold. Here, we define E_{th} as the 50% breakdown probability with energy-probability curves generated by sigmoidal probit regression analysis of 200 - 250 pulses [230]. We measured E_{th} once per day across three days to verify the stability of our measurements and to account for day-to-day variability in laser performance. We found the three-day average for E_{th} in pure water to be $E_{th,3_{Day}} = 0.747 \pm 0.006\ \mu J$. Since the ultimate goal is to translate our research into biologically-relevant applications, we tested optical breakdown threshold energies in a variety of solutions other than pure water: Dulbeccos phosphate-buffered saline (DPBS - Sigma-Aldrich, St. Louis, MO); a pH 7.4 - 300 mOsm/kg live cell physiological imaging solution (referenced as CHO-OSS); 99.9% pure deuterated water (D_2O); and finally 0.1 and 0.5 molarity NaCl saline solutions for testing of donor electron concentration-dependence. DPBS is a standard buffered salt solution used in maintaining cell culture and preparing cell culture experiments. DPBS is commercially available through most life sciences retailers. The CHO-OSS imaging buffer solution contained 135 mM NaCl, 5 mM KCl, 10 mM HEPES, 10 mM glucose, 2 mM $CaCl_2$, and 2 mM $MgCl_2$ with a pH of 7.4 and osmolality of 290310 Osm/kg (all buffer components from Sigma-Aldrich, St. Louis, MO). Each of these samples was selected as biologically-relevant samples, while also providing for controlled variations in chemical composition and concentrations of complex molecules present in biology. Probit curves for determining E_{th} measurement for each sample are provided in Fig. 5.1(c). All experiments were conducted in open air environment in our laboratory. The temperature and humidity of the laboratory were maintained by the laboratory air conditioning system in accordance with standard government laboratory guidelines (70-72 °F and approx. 50% humidity). Dust level was not checked during these

experiments; however, all sample volumes were contained in glass bottom petri dishes typical of cell culture experiments with glass coverslip approximately 170 μm thick (Cat:P35G-1.5-14-C 35 mm Dish, No. 1.5 Coverslip, 14 mm Glass Diameter, Uncoated; Mattek Corporation, Ashland, MA). These petri dishes are manufactured and stored in sterile packaging. Likewise, all sample volumes were kept sterile prior to experiments. Additional care was taken to prevent introduction of dust and other environmental contaminants to the sample space, including replacing all sample volumes every 25 pulses to reduce the impact of impurity build up or potential ionic discharge from the electrodes. Samples were placed above the microscope objective (HCX PL Fluotar; 20x 0.4 NA; Leica Microsystems) with an inverted microscope arrangement; initial trial experiments indicated that focusing too close to the surface of glass cover slip would cause damage to the cover slip surface, leaving marks that would likely impact subsequent results. Therefore, all experiments were carried out at a focal depth of $200\ \mu m$ above the surface of the cover slip, as measured by the probe beam focal spot reflection imaged to our camera, thus avoiding optically-induced damage and any undesired focus related effects. The Sample containers were replaced after each sample trial such that no dish was reused and to minimize potential contamination between samples.

5.3 Results

5.3.1 Opto-electrical breakdown: E_{th} and controls

We measured E_{th} at three separate timing delays between the psLP and nsEP in pure water with the psLP occurring before, during, or after nsEP application to examine the influence of external electrical impulses on optical breakdown thresholds. The temporal profile of nsEP and its relative position to psLP for the various scenarios are shown in Fig. 5.2(a). Figure 5.2(b) shows the breakdown threshold curve for the pre-nsEP control case ($E_{th,pre} = 0.749 \pm 0.008\ \mu J$) is a near-perfect match to the curve using only the psLP with electrodes in place but no charge applied ($E_{th,NC} = 0.746 \pm 0.008\ \mu J$). This result indicates that breakdown events are caused solely by the psLP, with no contribution from nsEP immediately following the psLP. For the post-nsEP case, we found the bubble threshold energy to be $E_{th,post} = 0.756 \pm 0.006\ \mu J$, a 1.3% difference from the

pre-nsEP control scenario. This result is within the expected error of measurements and indicates that nsEP has a limited influence, if any, on the value of E_{th} for the subsequent psLP (time intervals $\geq$ 200 ns). As no difference was seen in pre-, post-, and no-charge control exposures, the pre-nsEP case will serve as the control condition throughout this chapter discussion. Temporal combination of the psLP with nsEP (psLP applied 280 ns after nsEP rise time) resulted in a breakdown threshold measurement of $E_{th,during} = 0.711 \pm 0.004\ \mu J$. This represents a reduction of > 5% than that of the pre-nsEP control case. These results demonstrate that there is not only an observable decrease in breakdown threshold for the combined psLP + nsEP case indicating a dependence on pulse timing, but also that the observed effect is statistically significant, as represented by the separation of 95% confidence intervals at 50% probability during impulse.

5.3.2 Opto-electrical breakdown: modeling

To compare our experimental observations with our opto-electrical breakdown model, we initially selected background impurity density of double-distilled water $n_{imp} = 2.8 \times 10^4\ cm^{-3}$ [231], and calculated the theoretical condition to achieve breakdown to be a critical electron density of $n_{th} = 2.1 \times 10^{20}\ cm^{-3}$.

Our experimental design incorporated bubble formation as the breakdown threshold criteria, which, for ultrashort laser pulses, corresponds to a temperature rise $\Delta T = 148K$ [209]. The critical electron density n_{th} was obtained by the relationship $n_{th} = \Delta T \rho_o C_p / (E_{gap} + \epsilon_{avg}))$ [209], where ρ_o and C_p are the mass density and heat capacity of water respectively, and ϵ_{avg} is the average kinetic energy of CB electrons. ϵ_{avg} approaches 7.2 eV under asymptotic conditions [226]. This carrier density corresponds to an irradiance threshold (I_{th}) of $I_{th} = 5.75 \times 10^{15}\ W/m^2$ for a single psLP at 1064 nm. Figure 5.3(a) shows the plasma dynamics produced by such a laser pulse, and Fig. 5.3(b) shows the overall electron density calculations corresponding to each of the pulse separation times in our experiment. Under these conditions, avalanche ionization contributes most of the free electrons ($n_{max,AI} \approx 2 \times 10^{20}\ cm^{-3}$), with a very small SFI contribution ($n_{max,SFI} \approx 10^{13}\ cm^{-3}$). The simulation predicted a 6% reduction in I_{th} with a laser irradiance threshold of $I_{th} = 5.4 \times 10^{15}\ W/m^2$ for combined psLP and nsEP. The model also predicts that the reduction in

breakdown threshold has a strong dependence on the electrical impulse timing and corresponding increase in carrier density. Our modeling and experimental results both suggest that if an externally applied electric impulse is strong enough, it can provide additional seed electrons to support the ionization process by promoting donor electrons at energy E_d into the CB, thereby reducing E_{th}. Figure 5.3(c) provides a visual explanation for the observed behavior as it relates to biologically relevant solutions which is addressed in the discussion section of this chapter.

The relationship for n_{th} can also be rearranged to provide an estimate for the temperature rise ΔT induced by an nsEP pulse. Immediately following the psLP, CB electron density drops quickly due to recombination and then gradually levels out at $n_{total} = 2.3 \times 10^{16}\ cm^{-3}$ due to a balance between AI induced by nsEP and losses from recombination and diffusion. According to the relationship, thermalization of one set of these electrons leads to temperature rise of $\Delta T = 0.015K$. Considering the duration of the nsEP pulse continues for roughly 300 ns after the psLP, a time much longer than the characteristic recombination lifetime that relates to n_{total} by $\tau_{rec} = 1/(\eta_{rec}\eta_{total})$, or $\tau_{rec} = 24$ ns for $n_{total} = 2.3 \times 10^{16}\ cm^{-3}$ with the assumed $\eta_{rec} = 1.8 \times 10^{-9}\ cm^3 s^{-1}$ [209]. Therefore, about 13 sets of electrons are thermalized which provides to a total temperature rise on the order of $\Delta T = 0.2K$.

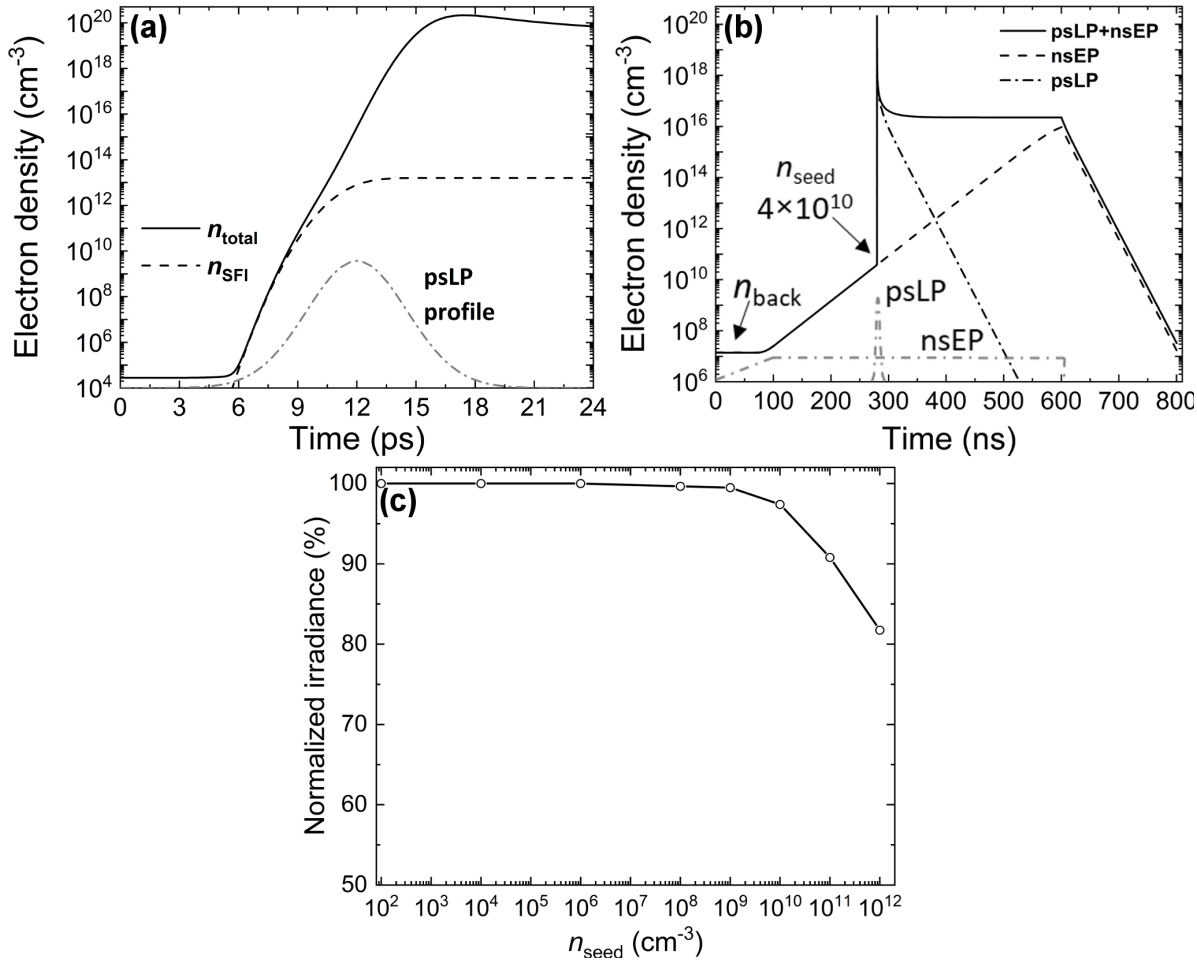

Figure 5.3: Opto-electrical breakdown modeling. (a) Plasma dynamics produced by Gaussian ps laser pulse (solid line) SFI contribution for book-keeping (dashed line); psLP profile (gray dash-dot). (b) Plasma dynamics produced by nsEP + psLP combination (solid), single 40 kV/cm nsEP (dash-dot), and single psLP (dashed line). Profiles of psLP and nsEP, their relative timing shown in gray dash-dotted lines. (c) Visualized thought-experiment for breakdown threshold reduction: normalized irradiance as a function of seed electron density n_{seed} in biological-relevant solutions. A simulated representation of a single psLP thresholds based on different initial seed electron densities as provided by various nsEP intensities. Reference $I_{psLP} = 5.75 \times 10^{15}\ W/m^2$, for $n_{seed} = 10^2\ cm^{-3}$, close to n_{imp} in double distilled water.

5.3.3 Breakdown threshold dependencies

Previous studies have suggested laser polarization (circular versus linear) could impact breakdown thresholds [232]. We investigated the impact of our incident laser's linear polarization angle with respect to nsEP direction (at 40 kV/cm). We observed no polarization dependence beyond the range of expected statistical errors. These results further suggest that psLP dominates initiation of the breakdown process and nsEP produces little impact beyond providing additional seed electrons.[3]

Finally, we examined the effects of nsEP intensity and solution donor electron densities on the observed E_{th} reduction phenomenon. To do this, we first measured and compared optical breakdown thresholds in DPBS under three electric field conditions with power supply output voltages of 1, 1.5, and 2 kV, corresponding to nsEP intensities of 18, 31, and 40 kV/cm, respectively, chosen as approximations to 50%, 75% and 100% of the maximum field intensities attainable across the samples. A reliable maximum was desirable for testing our initial hypothesis, with the two lower field intensities of 19 kV/cm and 31 kV/cm chosen for evaluating any field-intensity dependencies of the synergistic effect.

To explore the impact of donor electron density we prepared NaCl saline solution with 0.1, and 0.5 molarity in pure water and measured the breakdown thresholds with and without a 9 kV/cm electric field. The varying concentration of NaCl solution is akin to various densities of complex molecules in biological solutions capable of providing donor electrons for promotion to the CB. Donor density is important at longer wavelengths, as a greater carrier density in a medium provides a larger number of potential seed electrons for breakdown initiation through thermally-induced collisions or through optical absorption of photons [204, 233, 234].

An inverse relationship between the nsEP field intensity and E_{th} was observed and is shown in Fig. 5.4(a). We recorded E_{th} reductions of 14% at 40 kV/cm, 12.5% at 31 kV/cm, and 7% at 18 kV/cm. These reductions can be attributed to the energetic molecules in DPBS providing additional CB electrons via a reduced excitation energy, E_d, in the presence of the electric field. The apparent

[3] A brief discussion regarding the polarization test results are provided in Appendix C

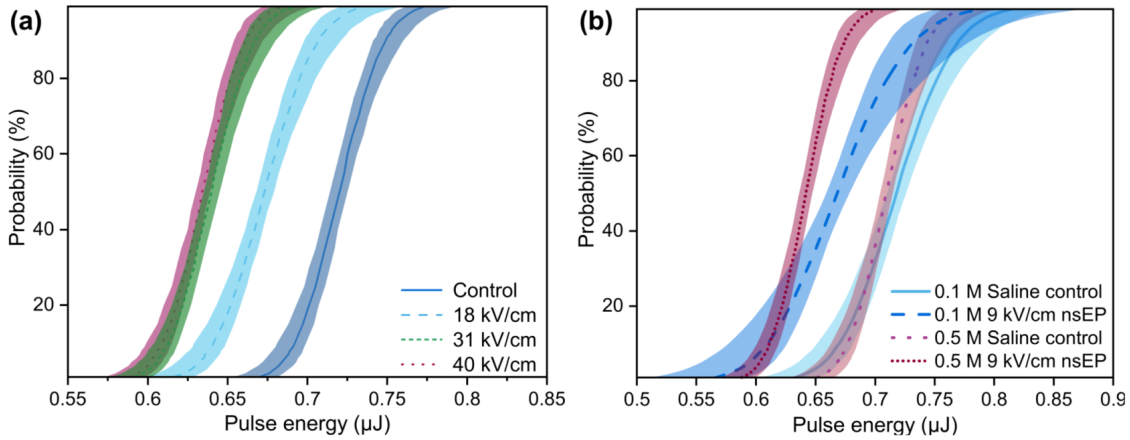

Figure 5.4: Electric field and carrier density dependence. Probit analysis curves for reduction of E_{th} on (a) voltage dependence in DPBS biological solution and (b) donor carrier density in 0.1 M and 0.5 M saline solution with 9 kV/cm nsEP.

saturation effect after 31 kV/cm can be explained by the fact that the donor electrons are almost all excited into the CB and the E_d channel is nearly depleted. We measured breakdown thresholds for each saline control condition to be $E_{th} = 0.718 \pm 0.006\ \mu J$, and $0.709 \pm 0.006\ \mu J$ for 0.1 M and 0.5 M saline, respectively. Furthermore, we measured a reduction of $\Delta E_{th} = 0.050\ \mu J$ and $0.068\ \mu J$ with application of a 9 kV/cm nsEP to the 0.1 M and 0.5 M solutions, respectively. These results are shown in Fig. 5.4(b) and imply that the increased density of donor electrons provided by the saline concentrations leads to not only lower breakdown thresholds in general, but also to a stronger synergistic effect when compared to psLP alone.

5.4 Discussion and outlook

The results presented in this chapter demonstrate that the breakdown process observed with combined psLP and nsEP is initiated solely by the laser pulse. However, if an externally applied electric impulse is strong enough, it can provide a "primer" type effect to the target media, promoting donor electrons at energy E_d into the CB to support the ionization process, thereby reducing E_{th}. Figure 5.3(c) provides a visual explanation for the observed behavior as it relates to biologically relevant solutions. Both the donor level E_d and number density of donors n_d for biological-relevant solutions are unknown; therefore, we are unable to directly simulate threshold

reduction as a function of DC field intensity but alternatively turn to an assumed increasing seed electron density with increasing DC field. Taking this into account, we consider that the extra seed electrons come in the form of donor electrons from energetic molecules in the solutions; this scenario is similar to n-type doping in semiconductors [227]. Donor electrons can be driven by an external electric field into the CB through tunnel ionization, as proposed by Vanraes and Bogaerts [228]. AI induced by the electric impulse is very weak, with associated temperature rise on the order of $\sim$ 1 Kelvin [173], as determined by indicating that the reduction phenomenon observed is specifically driven by nsEP providing additional seed electrons to the CB and not by nsEP driving AI following the optical pulse.

For example, Fig. 5.3(b) shows that when breakdown is initiated in water 200 ns after the falling edge of a 40 kV/cm nsEP, the carrier density has again dropped below the minimum threshold, as determined by the first density by which irradiance threshold is shown to decrease at $n_{seed} \leq 10^8\ cm^{-3}$ in Fig. 5.3(c). We determine this threshold for n_{seed} through the depiction in Fig. 5.3(c) where irradiance threshold first begins to decrease. This agrees with experimental observations shown in Fig. 5.2(b). If we contemplate the thought-experiment explanation provided in Fig. 5.3(c) and consider the dynamics of n_{seed} following the end of the electrical impulse shown in Fig. 5.2(b), it follows that as n_{seed} drops to its original value, the threshold normalizes as well. The promoted CB electrons, absent the external electric field, will go toward solvation as they lose kinetic energy through collisions and then get trapped at the intermediate energy level above the valence band; the lifetime of these processes can be as long as 300 ns [208, 235]. Breakdown simulation results demonstrate that the diffusion rates are critical for psLPs applied immediately following nsEP and determine whether there are enough seed electrons present to reduce the optical breakdown threshold. The influence of diffusion rate for CB electron density decay, post-nsEP, follows an exponential decay of the form $n_{total} \propto e^{-t/\tau_{diff}}$. As the characteristic diffusion time ($\tau_{diff} = 10\ ns$) is much smaller than the characteristic recombination lifetime, diffusion is the dominant decay mechanisms. Furthermore, the 40 kV/cm maximum field applied in our experiment was too weak to provide sufficient carriers for AI to entirely compensate for losses of CB

electrons due to recombination and diffusion; if a stronger field were applied, we could then measure E_{th} as a function of delay between the end of nsEP and the applied laser pulse. We can see by the plot in Fig. 5.3(c) that an external electric field providing $n_{seed} = 10^{12}\ cm^{-3}$ can reduce E_{th} by $\approx 20\%$ and as mentioned previously, $n_{seed} \leq 10^{8}\ cm^{-3}$ cannot have such an effect. Using the initial electron densities of the media and the respective measured E_{th} at various times following the falling edge of nsEP along with the results from our model, we can then extrapolate the ambipolar diffusion constant, τ_{diff}, of a target media. A specific case that warrants additional study is that of heavy water (D_2O), as shown in Fig. 5.1(c); where there was reported a notably lower breakdown threshold compared to that of distilled water. Several investigations have shown similarities, as well as small but not insignificant differences, between the dielectric properties of water H_2O and heavy water D_2O [236, 237, 238]. A more in-depth investigation following the methodology presented in a recent report by Perry, et al. may yield interesting results [239]. Likewise, the correlation between the DC field strength and the seed electron density will be pursued in future studies.

We note that these results demonstrate optical pulse synergy with a relatively long, 600-ns, electrical impulse and that shorter picosecond-pulse delivery systems are are commercially available capable of providing much shorter duration pulses, down to 200-ps, with sharp rise and fall times that would allow for substantially higher electrical fields to be applied. Employing such systems would further expand the capabilities and application of the discovered synergistic effect. As it stands, the synergistic effect that we have observed can be employed to enhance a wide range of laser-based applications in medicine. A report by Yanik, et al. demonstrated the use of 200 fs NIR laser pulses as a low-energy option for performing neuron axotomy in C. elegans [240]. Our results indicate that we can achieve an even further reduction of optical pulse energy requirements for micro- and nano-scale surgeries, and as well a potential method for reducing collateral damage to nearby cells and tissue. Furthermore, ablative fractional laser (AFL)-assisted drug delivery is a powerful tool for topical drug delivery systems that uses a range of specific laser parameters suited to specific drugs, treatments, damage thresholds and patient conditions [241]. Reducing the energy

threshold for tissue ablation would allow for a wider range of parameter selections, particularly in cases where residual damage is a concern for treatment. Reducing laser pulse energy requirements or even removing the need for material specific laser parameters would help to advance these techniques and their applications. We plan to expand this investigation to include biological systems and the effects of opto-electroporation of cells [242, 243, 244]. Application-based studies are currently under way utilizing the synergistic behavior detailed in this chapter for targeted cell response, membrane permeabilization, dye uptake, and translations to targeted drug delivery and DNA transfection[4].

5.5 Chapter summary

In summary, a novel approach to control optical breakdown with external electrical pulses was proposed and demonstrated both theoretically and experimentally. The developed theory and accompanying experimental data provide a better understanding of the mechanisms underlying combined electric field and pulsed laser interactions at short time scales. Our results indicate that breakdown process under intense picosecond laser irradiation with concurrent DC electric field is initiated solely by the laser pulse, with the DC electric field acting as a primer by providing additional seed electrons for breakdown initiation. As this method can, under carefully considered circumstances, provide for an environment with a DC electric field sufficiently strong as to compensate for diffusion and recombination rates in a target media, it is expected that we can gleam further insight into direct ambipolar diffusion measurements in specific target media, based on time-dependent measurements of E_{th} following the end of a DC electric field pulse in the future.

[4] An additional discussion related to preliminary cell-based studies is provided in Appendix C.

6. CONCLUSIONS

In conclusion, the past two decades have seen Brillouin spectroscopy evolve from a slow and extremely limited spectroscopic technique to a modern imaging modality with limitless potential. The work presented in this dissertation further demonstrates that advances in Brillion spectroscopy have enabled it as an applicable technique for biological investigations through time-resolved measurements of cell and subcellular biomechanical properties on a microscope platform. By coupling Brillouin spectroscopy with Raman spectroscopy, our custom built system can be used to measure and observe changes of whole cell and intracellular compartments with both mechanical and chemical specificity. The capability to observe how the properties of biological materials react and change in response to external stimuli represents a powerful advancement in the field of cellular biomechanics as these properties in cells and tissues are critical to physical and pathological processes. Brillouin microscopy has unbarred potential as a non-invasive, label-free tool for future applications in biomedical research and for the development of clinical diagnostics and treatment techniques.

This work contributes to the many efforts progressing the development and applications of Brillouin spectroscopy. We have provided a performance assessment for both a modern VIPA-based Brillouin spectrometer and a commercially-available tandem Fabry-Perot interferometer system; this assessment was published in the journal Optics Express, 2018 [113]. We have demonstrated Brillouin spectroscopy as a viable means for time-resolved mechanical measurements of cellular and subcellular structures along with 2D and 3D mechanical mapping of subcellular components; results are currently being prepared for publication. Additionally, we have presented findings related to a synergistic effect between short, picosecond optical pulses and nanosecond pulsed electric fields that results in a reduction of the optical pulse energy required to initiate breakdown events; results were published in the journal Photonics Research, 2021 [196].

Additional works have also been carried out beyond the scope of this dissertation over the last six years (data not shown here, but have contributed to over twenty conference presentations and

papers). We have worked toward a multitude of goals: establishing new protocols and applications of Brillouin spectroscopy ranging from plant stresses to burn injuries, engineering a dual-spectroscopy system capable of simultaneous Brillouin and low-frequency Raman measurements, the development of an up-conversion nanoparticle based smart substrate for remote temperature sensing, and assessing cell responses to combined optical and electrical stimuli with the intent to provide enhancement or inhibition of cell responses from targeted cell regions in culture conditions.

Our next steps include further developing our understanding of cell plasma membrane charging and discharging through use of ultra-fast imaging techniques such as streak, strobe, and compressed ultra-fast photography to visualize cell membrane potentials during nsPEF application [245, 246, 247]. We are also working toward combining another complimentary all-optical mechanical assessment method, quantitative phase imaging, with Brillouin spectroscopy [164]. Future Brillouin spectroscopy studies may also focus on taking advantage of quantum-enhancement of spectral signals for both enhanced sensitivity and increased imaging speeds [248].

While substantial instrumentation improvements have been made over the last two decades, much work is yet to be done for Brillouin technology to realize its full potential. It is our hope that Brillouin spectroscopy may one day become a standard elastography technique with myriad of biomedical and clinical applications at both macro (tissue level) and micro (cellular level) scales.

REFERENCES

[1] N. Roll-Hansen, "On the Reduction of Biology to Physical Science," *Synthese*, vol. 20, no. 2, pp. 277–289, 1969.

[2] K. A. Jansen, D. M. Donato, H. E. Balcioglu, T. Schmidt, E. H. Danen, and G. H. Koenderink, "A guide to mechanobiology: Where biology and physics meet," *Biochimica et Biophysica Acta (BBA) - Molecular Cell Research*, vol. 1853, pp. 3043–3052, Nov. 2015.

[3] A. Mukherjee, A. Barai, R. K. Singh, W. Yan, and S. Sen, "Nuclear plasticity increases susceptibility to damage during confined migration," *PLOS Computational Biology*, vol. 16, p. e1008300, Oct. 2020.

[4] P. Heine, A. Ehrlicher, and J. Käs, "Neuronal and metastatic cancer cells: Unlike brothers," *Biochimica et Biophysica Acta (BBA) - Molecular Cell Research*, vol. 1853, pp. 3126–3131, Nov. 2015.

[5] L. Chaubet, A. R. Chaudhary, H. K. Heris, A. J. Ehrlicher, and A. G. Hendricks, "Dynamic actin cross-linking governs the cytoplasms transition to fluid-like behavior," *MBoC*, vol. 31, pp. 1744–1752, July 2020.

[6] K. H. Vining and D. J. Mooney, "Mechanical forces direct stem cell behaviour in development and regeneration," *Nat Rev Mol Cell Biol*, vol. 18, pp. 728–742, Dec. 2017.

[7] B. A. Krajina, B. L. LeSavage, J. G. Roth, A. W. Zhu, P. C. Cai, A. J. Spakowitz, and S. C. Heilshorn, "Microrheology reveals simultaneous cell-mediated matrix stiffening and fluidization that underlie breast cancer invasion," *Science Advances*, vol. 7, p. eabe1969, Feb. 2021.

[8] Y. L. Han, A. F. Pegoraro, H. Li, K. Li, Y. Yuan, G. Xu, Z. Gu, J. Sun, Y. Hao, S. K. Gupta, Y. Li, W. Tang, H. Kang, L. Teng, J. J. Fredberg, and M. Guo, "Cell swelling, softening and

invasion in a three-dimensional breast cancer model," *Nature Physics*, vol. 16, pp. 101–108, Jan. 2020.

[9] B. Szachowicz-Petelska, I. Dobrzyska, Z. A. Figaszewski, and J. Kudelski, "Changes in the Physico-Chemical Properties of Human Kidney Cell Membranes during the Cancer Transformation," *Advances in Biological Chemistry*, vol. 4, pp. 223–231, June 2014.

[10] J.-L. Gennisson, T. Deffieux, M. Fink, and M. Tanter, "Ultrasound elastography: Principles and techniques," *Diagnostic and Interventional Imaging*, vol. 94, pp. 487–495, May 2013.

[11] G. P. Tolstykh, C. A. Olsovsky, B. L. Ibey, and H. T. Beier, "Ryanodine and IP3 receptor-mediated calcium signaling play a pivotal role in neurological infrared laser modulation," *Neurophotonics*, vol. 4, no. 2, pp. 1 – 8, 2017.

[12] J. C. Ullery, H. T. Beier, and B. L. Ibey, "Sensitivity of Cells to Nanosecond Pulsed Electric Fields is Dependent on Membrane Lipid Microdomains," in *1st World Congress on Electroporation and Pulsed Electric Fields in Biology, Medicine and Food & Environmental Technologies*, pp. 239–242, 2016.

[13] C. C. Roth, R. D. Glickman, G. P. Tolstykh, L. E. Estlack, E. K. Moen, I. Echchgadda, H. T. Beier, R. A. B. Jr, and B. L. Ibey, "Evaluation of the Genetic Response of U937 and Jurkat Cells to 10-Nanosecond Electrical Pulses (nsEP)," *PLOS ONE*, vol. 11, p. e0154555, May 2016.

[14] A. G. Pakhomov, A. M. Bowman, B. L. Ibey, F. M. Andre, O. N. Pakhomova, and K. H. Schoenbach, "Lipid nanopores can form a stable, ion channel-like conduction pathway in cell membrane," *Biochem Biophys Res Commun*, vol. 385, pp. 181–186, July 2009.

[15] S. Franklin, B. L. Ibey, K. Nash, and H. T. Beier, "Measurement of changes in plasma membrane phospholipid polarization following nanosecond pulsed electric field exposure," in *Terahertz and Ultrashort Electromagnetic Pulses for Biomedical Applications*, vol. 8585, pp. 136 – 142, SPIE, 2013.

[16] R. L. Vincelette, C. C. Roth, M. P. McConnell, J. A. Payne, H. T. Beier, and B. L. Ibey, "Thresholds for Phosphatidylserine Externalization in Chinese Hamster Ovarian Cells following Exposure to Nanosecond Pulsed Electrical Fields (nsPEF)," *PLoS ONE*, vol. 8, no. 4, pp. 1–12, 2013.

[17] G. P. Tolstykh, H. T. Beier, C. C. Roth, G. L. Thompson, J. A. Payne, M. A. Kuipers, and B. L. Ibey, "Activation of intracellular phosphoinositide signaling after a single 600 nanosecond electric pulse," *Bioelectrochemistry*, vol. 94, pp. 23–29, Dec. 2013.

[18] B. L. Ibey, W. P. Roach, and A. G. Pakhomov, "Quantification of cell sensitivity to nanosecond duration electrical pulses," in *Photons and Neurons*, vol. 7180, pp. 127 – 135, SPIE, 2009.

[19] U. Zimmermann, "Electric field-mediated fusion and related electrical phenomena," *Biochim Biophys Acta*, vol. 694, pp. 227–277, Nov. 1982.

[20] M. Wang, Y. Zhang, C. Cai, J. Tu, X. Guo, and D. Zhang, "Sonoporation-induced cell membrane permeabilization and cytoskeleton disassembly at varied acoustic and microbubble-cell parameters," *Scientific Reports*, vol. 8, p. 3885, Mar. 2018.

[21] R. A. Barnes, C. C. Roth, H. T. Beier, G. Noojin, C. Valdez, J. Bixler, E. Moen, M. Shadaram, and B. L. Ibey, "Probe beam deflection optical imaging of thermal and mechanical phenomena resulting from nanosecond electric pulse (nsEP) exposure in-vitro," *Opt. Express, OE*, vol. 25, pp. 6621–6643, Mar. 2017.

[22] G. L. Thompson, C. Roth, G. Tolstykh, M. Kuipers, and B. L. Ibey, "Disruption of the actin cortex contributes to susceptibility of mammalian cells to nanosecond pulsed electric fields," *Bioelectromagnetics*, vol. 35, no. 4, pp. 262–272, 2014.

[23] G. Thompson, J. A. Payne, C. C. Roth, G. J. Wilmink, and B. L. Ibey, "Local plasma membrane permeabilization of living cells by nanosecond electric pulses using atomic force microscopy," in *Nanoscale Imaging, Sensing, and Actuation for Biomedical Applications VIII, 79080U*, p. 79080U, Feb. 2011.

[24] G. L. Thompson, C. C. Roth, D. R. Dalzell, M. Kuipers, and B. L. Ibey, "Calcium influx affects intracellular transport and membrane repair following nanosecond pulsed electric field exposure," *J Biomed Opt*, vol. 19, p. 055005, May 2014.

[25] E. K. Moen, B. L. Ibey, H. T. Beier, and A. M. Armani, "Investigating membrane nanoporation induced by bipolar pulsed electric fields via second harmonic generation," *Appl. Phys. Lett.*, vol. 109, p. 113701, Sept. 2016.

[26] A. G. Pakhomov, I. Semenov, S. Xiao, O. N. Pakhomova, B. Gregory, K. H. Schoenbach, J. C. Ullery, H. T. Beier, S. R. Rajulapati, and B. L. Ibey, "Cancellation of cellular responses to nanoelectroporation by reversing the stimulus polarity," *Cell Mol Life Sci*, vol. 71, pp. 4431–4441, Nov. 2014.

[27] C. M. Valdez, R. A. Barnes, C. C. Roth, E. K. Moen, G. A. Throckmorton, and B. L. Ibey, "Asymmetrical bipolar nanosecond electric pulse widths modify bipolar cancellation," *Scientific Reports*, vol. 7, p. 16372, Nov. 2017.

[28] B. L. Ibey, J. N. Bixler, C. C. Roth, and H. T. Beier, "Evaluation of membrane potential changes induced by unipolar and bipolar nanosecond pulsed electric fields," in *High-Speed Biomedical Imaging and Spectroscopy IV*, vol. 10889, p. 1088913, International Society for Optics and Photonics, Mar. 2019.

[29] C. M. Valdez, R. Barnes, C. C. Roth, E. Moen, and B. Ibey, "The interphase interval within a bipolar nanosecond electric pulse modulates bipolar cancellation," *Bioelectromagnetics*, vol. 39, pp. 441–450, Sept. 2018.

[30] E. B. Sözer and P. T. Vernier, "Modulation of biological responses to 2 ns electrical stimuli by field reversal," *Biochimica et Biophysica Acta (BBA) - Biomembranes*, vol. 1861, pp. 1228–1239, June 2019.

[31] D. W. Ball, *Field Guide to Spectroscopy*. 1000 20th Street, Bellingham, WA 98227-0010 USA: SPIE, May 2006.

[32] J. D. Jackson, *Classical electrodynamics; 2nd ed.* New York, NY: Wiley, 1975.

[33] C. V. Raman, "Molecular Diffraction of Light," *Nature*, vol. 110, pp. 505–506, Oct. 1922.

[34] C. V. Raman, "A new radiation," *Indian Journal of Physics*, vol. 2, pp. 387–398, 1928.

[35] C. V. Raman and K. S. Krishnan, "The production of new radiations by light scattering. Part I," *Proceedings of the Royal Society of London. Series A, Containing Papers of a Mathematical and Physical Character*, vol. 122, pp. 23–35, Jan. 1929.

[36] A. Smekal, "Zur Quantentheorie der Dispersion," *Naturwissenschaften*, vol. 11, pp. 873–875, Oct. 1923.

[37] R. Singh and F. Riess, "The 1930 Nobel Prize for Physics: A Close Decision?," *Notes and Records of the Royal Society of London*, vol. 55, no. 2, pp. 267–283, 2001.

[38] I. L. Fabelinski, "The discovery of combinational scattering of light (the Raman effect)," *Sov. Phys. Usp.*, vol. 21, p. 780, Sept. 1978.

[39] H NUSSBAUMER, H. D. SCHMID, and M. Vogel, "Raman scattering as a diagnostic possibility in astrophysics," *Astronomy and Astrophysics*, vol. 211, pp. L27–30, 1989.

[40] R. L. McCreery, *Raman spectroscopy for chemical analysis*. No. v. 157 in Chemical analysis, New York: John Wiley & Sons, 2000.

[41] L. Brillouin, "Diffusion de la lumière et des rayons X par un corps transparent homogène. Influence de l'agitation thermique," *Ann. Phys.(Paris)*, vol. 17, no. 21, pp. 88–122, 1922.

[42] G. Landsberg and L. Mandelstam, "Über die Lichtzerstreuung in Kristallen," *Z. Physik*, vol. 50, pp. 769–780, Nov. 1928.

[43] T. Sebastian, K. Schultheiss, B. Obry, B. Hillebrands, and H. Schultheiss, "Micro-focused Brillouin light scattering: imaging spin waves at the nanoscale," *Front. Phys.*, vol. 3, p. 35, 2015.

[44] R. Freeman, R. Lemasters, T. Kalejaiye, F. Wang, G. Chen, J. Ding, M. Wu, V. E. Demidov, S. O. Demokritov, H. Harutyunyan, and S. Urazhdin, "Brillouin light scattering of spin

waves inaccessible with free-space light," *Phys. Rev. Research*, vol. 2, p. 033427, Sept. 2020.

[45] D. C. Liptak, J. C. Reber, J. F. Maguire, and M. S. Amer, "On the development of a confocal Rayleigh-Brillouin microscope," *Review of Scientific Instruments*, vol. 78, p. 016106, Jan. 2007.

[46] M. Damzen, V. Vlad, V. Babin, and A. Mocofanescu, *Stimulated Brillouin Scattering: Fundamentals and Applications*. CRC Press, 2003, 1 ed., 2003.

[47] G. Antonacci, T. Beck, A. Bilenca, J. Czarske, K. Elsayad, J. Guck, K. Kim, B. Krug, F. Palombo, R. Prevedel, and G. Scarcelli, "Recent progress and current opinions in Brillouin microscopy for life science applications," *Biophys Rev*, vol. 12, pp. 615–624, May 2020.

[48] S. Mattana, S. Caponi, F. Tamagnini, D. Fioretto, and F. Palombo, "Viscoelasticity of amyloid plaques in transgenic mouse brain studied by Brillouin microspectroscopy and correlative Raman analysis," *J Innov Opt Health Sci*, vol. 10, Nov. 2017.

[49] S. Mattana, M. Mattarelli, L. Urbanelli, K. Sagini, C. Emiliani, M. D. Serra, D. Fioretto, and S. Caponi, "Non-contact mechanical and chemical analysis of single living cells by microspectroscopic techniques," *Light: Science & Applications*, vol. 7, pp. 17139–17139, Feb. 2018.

[50] G. Scarcelli and S. H. Yun, "Confocal Brillouin microscopy for three-dimensional mechanical imaging," *Nature Photonics*, vol. 2, no. 1, pp. 39–43, 2007.

[51] G. Scarcelli, P. Kim, and S. Yun, "In vivo measurement of age-related stiffening in the crystalline lens by Brillouin optical microscopy," *Biophys J*, vol. 101, pp. 1539–1545, Sept. 2011.

[52] Mandelstam, "On light scattering by an inhomogeneous medium," *J. Russ. Phys. Chem. Soc.*, vol. 58, 1926.

[53] D. J. Weidner, K. Swyler, and H. R. Carleton, "Elasticity of microcrystals," *Geophysical Research Letters*, vol. 2, no. 5, pp. 189–192, 1975.

[54] S. Speziale, H. Marquardt, and T. S. Duffy, "Brillouin Scattering and its Application in Geosciences," *Reviews in Mineralogy and Geochemistry*, vol. 78, pp. 543–603, Jan. 2014.

[55] N. H. Wan, F. Meng, T. Schröder, R.-J. Shiue, E. H. Chen, and D. Englund, "High-resolution optical spectroscopy using multimode interference in a compact tapered fibre," *Nature Communications*, vol. 6, p. 7762, July 2015.

[56] A.-Q. Jiang, K.-Y. Zang, H.-T. Tu, J.-K. Chen, W.-J. Lu, O. Yoshie, X.-P. Wang, X.-D. Xiang, Y.-P. Lee, B. Chen, Y.-X. Zheng, S.-Y. Wang, H.-B. Zhao, Y.-M. Yang, and L.-Y. Chen, "Ultrahigh-resolution spectrometer based on 19 integrated gratings," *Scientific Reports*, vol. 9, p. 10211, July 2019.

[57] K. J. Koski and J. L. Yarger, "Brillouin imaging," *Applied Physics Letters*, vol. 87, no. 6, pp. 20–23, 2005.

[58] Y. Ike, S. Tsukada, and S. Kojima, "High-resolution Brillouin spectroscopy with angular dispersion-type Fabry-Perot interferometer and its application to a quartz crystal," *Review of Scientific Instruments*, vol. 78, p. 076104, July 2007.

[59] Z. Meng and V. V. Yakovlev, "Optimizing signal collection efficiency of the VIPA-based Brillouin spectrometer," *Journal of Innovative Optical Health Sciences*, vol. 8, no. 4, p. 1550021, 2015.

[60] J. R. Sandercock, "Brillouin scattering study of SbSI using a double-passed, stabilised scanning interferometer," *Optics Communications*, vol. 2, pp. 73–76, July 1970.

[61] J. M. Vaughan and J. T. Randall, "Brillouin scattering, density and elastic properties of the lens and cornea of the eye," *Nature*, vol. 284, no. 5755, pp. 489–491, 1980.

[62] M. Vaughan, *The Fabry-Perot interferometer: history, theory, practice and applications*. CRC press, 1989.

[63] J. G. Dil, "Brillouin scattering in condensed matter," *Rep. Prog. Phys.*, vol. 45, pp. 285–334, Mar. 1982.

[64] D. Walton, J. J. Vanderwal, H. Xia, and P. Zhao, "The use of area detectors in Brillouin spectroscopy," *Review of Scientific Instruments*, vol. 67, pp. 2727–2731, Aug. 1996.

[65] K. J. Koski, J. Müller, H. D. Hochheimer, and J. L. Yarger, "High pressure angle-dispersive Brillouin spectroscopy: A technique for determining acoustic velocities and attenuations in liquids and solids," *Review of Scientific Instruments*, vol. 73, pp. 1235–1241, Mar. 2002.

[66] M. Shirasaki, "Filtering Characteristics of Virtually-Imaged Phased-Array," in *Integrated Photonics Research (1996), paper IMC3*, p. IMC3, Optical Society of America, Apr. 1996.

[67] M. Shirasaki, "Large angular dispersion by a virtually imaged phased array and its application to a wavelength demultiplexer," *Opt. Lett., OL*, vol. 21, pp. 366–368, Mar. 1996.

[68] G. Scarcelli and S. H. Yun, "Multistage VIPA etalons for high-extinction parallel Brillouin spectroscopy.," *Optics express*, vol. 19, no. 11, pp. 10913–10922, 2011.

[69] P. J. Horoyski and M. L. W. Thewalt, "Fourier Transform Raman and Brillouin Spectroscopy Using Atomic Vapor Filters," *Appl. Spectrosc., AS*, vol. 48, pp. 843–847, July 1994.

[70] Z. Meng, A. J. Traverso, and V. V. Yakovlev, "Background clean-up in Brillouin microspectroscopy of scattering medium," *Optics express*, vol. 22, no. 5, pp. 5410–5, 2014.

[71] G. Antonacci, G. Lepert, C. Paterson, and P. Török, "Elastic suppression in Brillouin imaging by destructive interference," *Applied Physics Letters*, vol. 107, p. 061102, Aug. 2015.

[72] E. Edrei, M. C. Gather, and G. Scarcelli, "Integration of spectral coronagraphy within VIPA-based spectrometers for high extinction Brillouin imaging," *Opt. Express*, vol. 25, no. 6, pp. 6895–6903, 2017.

[73] E. Edrei and G. Scarcelli, "Brillouin micro-spectroscopy through aberrations via sensorless adaptive optics," *Appl. Phys. Lett.*, vol. 112, p. 163701, Apr. 2018.

[74] D. S. Bedborough and D. A. Jackson, "Brillouin scattering study of gelatin gel using a double passed Fabry-Perot spectrometer," *Polymer*, vol. 17, pp. 573–576, July 1976.

[75] S. Cusack and A. Miller, "Determination of the elastic constants of collagen by Brillouin light scattering," *Journal of Molecular Biology*, vol. 135, pp. 39–51, Nov. 1979.

[76] R. Harley, D. James, A. Miller, and J. W. White, "Phonons and the elastic moduli of collagen and muscle," *Nature*, vol. 267, pp. 285–287, May 1977.

[77] J. Randall, J. M. Vaughan, and S. Cusak, "Brillouin scattering in systems of biological significance [and discussion]," *Philosophical Transactions of the Royal Society of London. Series A, Mathematical and Physical Sciences*, vol. 293, no. 1402, pp. 341–348, 1979.

[78] J.-P. LePesant, L. Powers, and P. S. Pershan, "Brillouin light scattering measurement of the elastic properties of aligned multilamella lipid samples," *PNAS*, vol. 75, pp. 1792–1795, Apr. 1978.

[79] G. Maret, R. Oldenbourg, G. Winterling, K. Dransfeld, and A. Rupprecht, "Velocity of high frequency sound waves in oriented DNA fibres and films determined by Brillouin scattering," *Colloid & Polymer Sci*, vol. 257, pp. 1017–1020, Oct. 1979.

[80] M. B. Hakim, S. M. Lindsay, and J. Powell, "The speed of sound in DNA," *Biopolymers*, vol. 23, no. 7, pp. 1185–1192, 1984.

[81] W. Doster, B. Simon, G. Schmidt, and W. Mayr, "Compressibility of lysozyme in solution from time-resolved brillouin difference spectroscopy," *Biopolymers*, vol. 24, pp. 1543–1548, Aug. 1985.

[82] N. Berovic, N. Thomas, R. A. Thornhill, and J. M. Vaughan, "Observation of Brillouin scattering from single muscle fibres," *Eur Biophys J*, vol. 17, pp. 69–74, June 1989.

[83] S. Cusack and S. Lees, "Variation of longitudinal acoustic velocity at gigahertz frequencies with water content in rat-tail tendon fibers," *Biopolymers*, vol. 23, no. 2, pp. 337–351, 1984.

[84] Z. Meng, A. J. Traverso, C. W. Ballmann, M. A. Troyanova-Wood, and V. V. Yakovlev, "Seeing cells in a new light: a renaissance of Brillouin spectroscopy," *Adv. Opt. Photon.*, vol. 8, pp. 300–327, June 2016.

[85] R. Sanctuary, R. Bactavatchalou, U. Müller, W. Possart, P. Alnot, and J. K. Krüger, "Acoustic profilometry within polymers as performed by Brillouin microscopy," *Journal of Physics D: Applied Physics*, vol. 36, no. 21, pp. 2738–2742, 2003.

[86] W. L. Johnson, S. A. Kim, Z. N. Utegulov, J. M. Shaw, and B. T. Draine, "Optimization of arrays of gold nanodisks for plasmon-mediated brillouin light scattering," *J. Phys. Chem. C*, vol. 113, pp. 14651–14657, Aug. 2009.

[87] Z. N. Utegulov, J. M. Shaw, B. T. Draine, S. A. Kim, and W. L. Johnson, "Surface-plasmon enhancement of Brillouin light scattering from gold-nanodisk arrays on glass," p. 66411M, Sept. 2007.

[88] E. E. Eloranta, "High Spectral Resolution Lidar," in *Lidar: Range-Resolved Optical Remote Sensing of the Atmosphere*, Springer Series in Optical Sciences, pp. 143–163, New York, NY: Springer, 2005.

[89] G. D. Hickman, J. M. Harding, M. Carnes, A. Pressman, G. W. Kattawar, and E. S. Fry, "Aircraft laser sensing of sound velocity in water: Brillouin scattering," *Remote Sensing of Environment*, vol. 36, no. 3, pp. 165–178, 1991.

[90] R. Prevedel, A. Diz-Muñoz, G. Ruocco, and G. Antonacci, "Brillouin microscopy: an emerging tool for mechanobiology," *Nature Methods*, vol. 16, pp. 969–977, Oct. 2019.

[91] F. Palombo and D. Fioretto, "Brillouin Light Scattering: Applications in Biomedical Sciences," *Chem. Rev.*, vol. 119, pp. 7833–7847, July 2019.

[92] G. Scarcelli and S. H. Yun, "In vivo Brillouin optical microscopy of the human eye," *Opt. Express, OE*, vol. 20, pp. 9197–9202, Apr. 2012.

[93] G. Scarcelli, S. Kling, E. Quijano, R. Pineda, S. Marcos, and S. H. Yun, "Brillouin microscopy of collagen crosslinking: Noncontact depth-dependent analysis of corneal elastic

modulus," *Investigative Ophthalmology and Visual Science*, vol. 54, no. 2, pp. 1418–1425, 2013.

[94] S. Besner, G. Scarcelli, R. Pineda, and S.-H. Yun, "In Vivo Brillouin Analysis of the Aging Crystalline Lens," *Invest Ophthalmol Vis Sci*, vol. 57, pp. 5093–5100, Oct. 2016.

[95] S. H. Yun and D. Chernyak, "Brillouin microscopy: assessing ocular tissue biomechanics," *Current Opinion in Ophthalmology*, vol. 29, pp. 299–305, July 2018.

[96] N. M. E. Ayad, S. Kaushik, and V. M. Weaver, "Tissue mechanics, an important regulator of development and disease," *Philosophical Transactions of the Royal Society B: Biological Sciences*, vol. 374, p. 20180215, Aug. 2019.

[97] S. Budday, T. C. Ovaert, G. A. Holzapfel, P. Steinmann, and E. Kuhl, "Fifty Shades of Brain: A Review on the Mechanical Testing and Modeling of Brain Tissue," *Arch Computat Methods Eng*, vol. 27, pp. 1187–1230, Sept. 2020.

[98] J. A. Hardy and G. A. Higgins, "Alzheimer's disease: the amyloid cascade hypothesis," *Science*, vol. 256, pp. 184–185, Apr. 1992.

[99] K. Fukui, S. Takayanagi, D. Suga, and M. Matsukawa, "Measurement of Wave Velocity in Cortical Bone by Micro-Brillouin Scattering Technique: Effect of Bone Tissue Properties," *Jpn. J. Appl. Phys.*, vol. 51, p. 07GF20, July 2012.

[100] M. Matsukawa, R. Tsubota, M. Kawabe, and K. Fukui, "Application of a micro-Brillouin scattering technique to characterize bone in the GHz range," *Ultrasonics*, vol. 54, pp. 1155–1161, July 2014.

[101] M. Troyanova-Wood, C. Gobbell, Z. Meng, A. A. Gashev, and V. V. Yakovlev, "Optical assessment of changes in mechanical and chemical properties of adipose tissue in diet-induced obese rats," *Journal of Biophotonics*, vol. 9, pp. 1–10, 2017.

[102] M. Troyanova-Wood, Z. Meng, and V. V. Yakovlev, "Differentiating melanoma and healthy tissues based on elasticity-specific Brillouin microspectroscopy," *Biomed. Opt. Express, BOE*, vol. 10, pp. 1774–1781, Apr. 2019.

[103] M. TroyanovaWood, C. Gobbell, Z. Meng, O. Gasheva, A. Gashev, and V. V. Yakovlev, "Assessing the effect of prolonged use of desloratadine on adipose Brillouin shift and composition in rats," *Journal of Biophotonics*, vol. 14, no. 1, p. e202000269, 2021.

[104] Z. Steelman, Z. Meng, A. J. Traverso, and V. V. Yakovlev, "Brillouin spectroscopy as a new method of screening for increased CSF total protein during bacterial meningitis," *Journal of Biophotonics*, vol. 8, no. 5, pp. 408–414, 2015.

[105] R. J. J. Riobóo, M. Desco, and M. V. Gómez-Gaviro, "Impact of optical tissue clearing on the Brillouin signal from biological tissue samples," *Biomed Opt Express*, vol. 10, pp. 2674–2683, May 2019.

[106] J. Margueritat, A. Virgone-Carlotta, S. Monnier, H. Delanoë-Ayari, H. C. Mertani, A. Berthelot, Q. Martinet, X. Dagany, C. Rivière, J.-P. Rieu, and T. Dehoux, "High-Frequency Mechanical Properties of Tumors Measured by Brillouin Light Scattering," *Phys. Rev. Lett.*, vol. 122, p. 018101, Jan. 2019.

[107] R. SchlüSSler, S. Möllmert, S. Abuhattum, G. Cojoc, P. Müller, K. Kim, C. Möckel, C. Zimmermann, J. Czarske, and J. Guck, "Mechanical Mapping of Spinal Cord Growth and Repair in Living Zebrafish Larvae by Brillouin Imaging," *Biophysical Journal*, vol. 115, pp. 911–923, Sept. 2018.

[108] R. Raghunathan, J. Zhang, C. Wu, J. Rippy, M. Singh, K. V. Larin, and G. Scarcelli, "Evaluating biomechanical properties of murine embryos using Brillouin microscopy and optical coherence tomography," *J Biomed Opt*, vol. 22, Aug. 2017.

[109] J. Zhang, R. Raghunathan, J. Rippy, C. Wu, R. H. Finnell, K. V. Larin, and G. Scarcelli, "Tissue biomechanics during cranial neural tube closure measured by Brillouin microscopy and optical coherence tomography," *Birth Defects Research*, vol. 111, no. 14, pp. 991–998, 2019.

[110] G. Scarcelli, W. J. Polacheck, H. T. Nia, K. Patel, A. J. Grodzinsky, R. D. Kamm, and S. H. Yun, "Noncontact three-dimensional mapping of intracellular hydromechanical properties

by Brillouin microscopy," *Nature Methods*, vol. 12, pp. 1132–1134, Dec. 2015.

[111] G. Antonacci and S. Braakman, "Biomechanics of subcellular structures by non-invasive Brillouin microscopy," *Scientific Reports*, vol. 6, p. 37217, Nov. 2016.

[112] G. Antonacci, V. de Turris, A. Rosa, and G. Ruocco, "Background-deflection Brillouin microscopy reveals altered biomechanics of intracellular stress granules by ALS protein FUS," *Communications Biology*, vol. 1, pp. 1–8, Sept. 2018.

[113] Z. Coker, M. Troyanova-Wood, A. J. Traverso, T. Yakupov, Z. N. Utegulov, and V. V. Yakovlev, "Assessing performance of modern Brillouin spectrometers," *Optics Express*, vol. 26, p. 2400, Jan. 2018.

[114] G. Antonacci, M. R. Foreman, C. Paterson, and P. Török, "Spectral broadening in Brillouin imaging," *Applied Physics Letters*, vol. 103, no. 22, pp. 5–8, 2013.

[115] K. Berghaus, J. Zhang, S. H. Yun, and G. Scarcelli, "High-finesse sub-GHz-resolution spectrometer employing VIPA etalons of different dispersion," *Opt. Lett., OL*, vol. 40, pp. 4436–4439, Oct. 2015.

[116] K. Elsayad, S. Werner, M. Gallemi, J. Kong, E. R. Sanchez Guajardo, L. Zhang, Y. Jaillais, T. Greb, and Y. Belkhadir, "Mapping the subcellular mechanical properties of live cells in tissues with fluorescence emission-Brillouin imaging," *Science Signaling*, vol. 9, no. 435, pp. rs5–rs5, 2016.

[117] Z. Meng and V. V. Yakovlev, "Precise Determination of Brillouin Scattering Spectrum Using a Virtually Imaged Phase Array (VIPA) Spectrometer and Charge-Coupled Device (CCD) Camera," *Applied Spectroscopy*, vol. 70, no. 8, pp. 1356–1363, 2016.

[118] C. Song, E. Sánchez-Ortiga, M. R. Foreman, and P. Török, "Optimisation of a single stage VIPA spectrometers (Conference Presentation)," in *Optical Elastography and Tissue Biomechanics IV*, vol. 10067, p. 100670N, International Society for Optics and Photonics, Apr. 2017.

[119] M. Troyanova-Wood, Z. Meng, and V. V. Yakovlev, "Elasticity-based identification of tumor margins using Brillouin spectroscopy," in *SPIE BiOS*, pp. 97190P–97190P, International Society for Optics and Photonics, 2016.

[120] I. Remer and A. Bilenca, "Background-free Brillouin spectroscopy in scattering media at 780 nm via stimulated Brillouin scattering," *Optics Letters*, vol. 41, no. 5, pp. 926–929, 2016.

[121] A. J. Traverso, J. V. Thompson, Z. A. Steelman, Z. Meng, M. O. Scully, and V. V. Yakovlev, "Dual Raman-Brillouin microscope for chemical and mechanical characterization and imaging," *Analytical Chemistry*, vol. 87, no. 15, pp. 7519–7523, 2015.

[122] A. J. Martin and W. Brenig, "Model for Brillouin Scattering in Amorphous Solids," *Physica Status Solidi (B)*, vol. 64, no. 1, pp. 163–172, 1974.

[123] M. Shirasaki, A. N. Akhter, and C. Lin, "Virtually imaged phased array with graded reflectivity," *IEEE Photonics Technology Letters*, vol. 11, no. 11, pp. 1443–1445, 1999.

[124] S. Xiao, A. M. Weiner, and C. Lin, "A dispersion law for virtually imaged phased-array spectral dispersers based on paraxial wave theory," *IEEE Journal of Quantum Electronics*, vol. 40, no. 4, pp. 420–426, 2004.

[125] K. V. Berghaus, S. H. Yun, and G. Scarcelli, "High Speed Sub-GHz Spectrometer for Brillouin Scattering Analysis," *JoVE (Journal of Visualized Experiments)*, p. e53468, Dec. 2015.

[126] Z. Meng and V. V. Yakovlev, "Optimizing signal collection efficiency of the VIPA-based Brillouin spectrometer," *J. Innov. Opt. Health Sci.*, vol. 08, p. 1550021, Nov. 2014.

[127] N. Ismail, C. C. Kores, D. Geskus, and M. Pollnau, "Fabry-Pérot resonator: spectral line shapes, generic and related Airy distributions, linewidths, finesses, and performance at low or frequency-dependent reflectivity," *Opt. Express*, vol. 24, p. 16366, July 2016.

[128] M. J. Weber, *Handbook of optical materials*. Boca Raton : CRC press, 10 ed., 2003.

[129] "Origin(pro)."

[130] J. Rheims, J. Köser, and T. Wriedt, "Refractive-index measurements in the near-IR using an Abbe refractometer," *Meas. Sci. Technol.*, vol. 8, pp. 601–605, June 1997.

[131] G. W. Willard, "Ultrasonic Absorption and Velocity Measurements in Numerous Liquid," *The Journal of the Acoustical Society of America*, vol. 12, no. 3, pp. 438–448, 1941.

[132] K. Liang, J. Xu, P. Zhang, Y. Wang, Q. Niu, L. Peng, and B. Zhou, "Temperature Dependence of the Rayleigh Brillouin Spectrum Linewidth in Air and Nitrogen," *Sensors*, vol. 17, no. 7, p. 1503, 2017.

[133] A. Fiore, J. Zhang, P. Shao, S. H. Yun, and G. Scarcelli, "High-extinction VIPA-based Brillouin spectroscopy of turbid biological media," *Applied Physics Letters*, vol. 108, no. 203701, pp. 1–9, 2016.

[134] D. S. Bryan, M. Stack, K. Krysztofiak, U. Cicho, D. G. Thomas, A. Surcel, E. S. Schiffhauer, M. A. Beckett, N. N. Khodarev, L. Xue, E. C. Poli, A. T. Pearson, M. C. Posner, D. N. Robinson, R. S. Rock, and R. R. Weichselbaum, "4-Hydroxyacetophenone modulates the actomyosin cytoskeleton to reduce metastasis," *Proc Natl Acad Sci USA*, vol. 117, pp. 22423–22429, Sept. 2020.

[135] Y. Shen, B. U. S. Schmidt, H. Kubitschke, E. W. Morawetz, B. Wolf, J. A. Käs, and W. Losert, "Detecting heterogeneity in and between breast cancer cell lines," *Cancer Convergence*, vol. 4, p. 1, Feb. 2020.

[136] Y. Shen, X. Wang, J. Lu, M. Salfenmoser, N. M. Wirsik, N. Schleussner, A. Imle, A. Freire Valls, P. Radhakrishnan, J. Liang, G. Wang, T. Muley, M. Schneider, C. Ruiz de Almodovar, A. Diz-Muñoz, and T. Schmidt, "Reduction of Liver Metastasis Stiffness Improves Response to Bevacizumab in Metastatic Colorectal Cancer," *Cancer Cell*, vol. 37, pp. 800–817.e7, June 2020.

[137] R. Gaetani, E. A. Zizzi, M. A. Deriu, U. Morbiducci, M. Pesce, and E. Messina, "When Stiffness Matters: Mechanosensing in Heart Development and Disease," *Front. Cell Dev. Biol.*, vol. 8, 2020.

[138] P. Shao, A. M. Eltony, T. G. Seiler, B. Tavakol, R. Pineda, T. Koller, T. Seiler, and S.-H. Yun, "Spatially-resolved Brillouin spectroscopy reveals biomechanical abnormalities in mild to advanced keratoconus in vivo," *Sci Rep*, vol. 9, May 2019.

[139] L. Wang, J. Xia, J. Li, T. L. Hagemann, J. R. Jones, E. Fraenkel, D. A. Weitz, S.-C. Zhang, A. Messing, and M. B. Feany, "Tissue and cellular rigidity and mechanosensitive signaling activation in Alexander disease," *Nature Communications*, vol. 9, p. 1899, May 2018.

[140] W. Zhao, B. Choate, and S. Ji, "Material properties of the brain in injury-relevant conditions Experiments and computational modeling," *Journal of the Mechanical Behavior of Biomedical Materials*, vol. 80, pp. 222–234, Apr. 2018.

[141] E. Moeendarbary and A. R. Harris, "Cell mechanics: principles, practices, and prospects," *WIREs Systems Biology and Medicine*, vol. 6, no. 5, pp. 371–388, 2014.

[142] M. Gupta, B. R. Sarangi, J. Deschamps, Y. Nematbakhsh, A. Callan-Jones, F. Margadant, R.-M. Mège, C. T. Lim, R. Voituriez, and B. Ladoux, "Adaptive rheology and ordering of cell cytoskeleton govern matrix rigidity sensing," *Nature Communications*, vol. 6, p. 7525, June 2015.

[143] M. Kräter, J. Sapudom, N. C. Bilz, T. Pompe, J. Guck, and C. Claus, "Alterations in Cell Mechanics by Actin Cytoskeletal Changes Correlate with Strain-Specific Rubella Virus Phenotypes for Cell Migration and Induction of Apoptosis," *Cells*, vol. 7, p. 136, Sept. 2018.

[144] W. Liu and C. Wu, "Rheological Study of Soft Matters: A Review of Microrheology and Microrheometers," *Macromol. Chem. Phys.*, vol. 219, p. 1700307, Feb. 2018.

[145] D. R. Overby, E. H. Zhou, R. Vargas-Pinto, R. M. Pedrigi, R. Fuchshofer, S. T. Braakman, R. Gupta, K. M. Perkumas, J. M. Sherwood, A. Vahabikashi, Q. Dang, J. H. Kim, C. R. Ethier, W. D. Stamer, J. J. Fredberg, and M. Johnson, "Altered mechanobiology of Schlemms canal endothelial cells in glaucoma," *PNAS*, vol. 111, pp. 13876–13881, Sept. 2014.

[146] V. Lam, T. Bigley, S. S. Terhune, and T. Wakatsuki, "A Method for Quantifying Mechanical Properties of Tissue following Viral Infection," *PLOS ONE*, vol. 7, p. e42197, Aug. 2012.

[147] T. Ye, N. Phan-Thien, B. C. Khoo, and C. T. Lim, "Stretching and Relaxation of Malaria-Infected Red Blood Cells," *Biophysical Journal*, vol. 105, pp. 1103–1109, Sept. 2013.

[148] E. Jonietz, "Mechanics: The forces of cancer," *Nature*, vol. 491, pp. S56–S57, Nov. 2012.

[149] T. Panciera, A. Citron, D. Di Biagio, G. Battilana, A. Gandin, S. Giulitti, M. Forcato, S. Bicciato, V. Panzetta, S. Fusco, L. Azzolin, A. Totaro, A. P. Dei Tos, M. Fassan, V. Vindigni, F. Bassetto, A. Rosato, G. Brusatin, M. Cordenonsi, and S. Piccolo, "Reprogramming normal cells into tumour precursors requires ECM stiffness and oncogene-mediated changes of cell mechanical properties," *Nat Mater*, vol. 19, pp. 797–806, July 2020.

[150] W. Xu, R. Mezencev, B. Kim, L. Wang, J. McDonald, and T. Sulchek, "Cell Stiffness Is a Biomarker of the Metastatic Potential of Ovarian Cancer Cells," *PLOS ONE*, vol. 7, p. e46609, Oct. 2012.

[151] E. H. Barriga, K. Franze, G. Charras, and R. Mayor, "Tissue stiffening coordinates morphogenesis by triggering collective cell migration in vivo," *Nature*, vol. 554, pp. 523–527, Feb. 2018.

[152] A. M. Handorf, Y. Zhou, M. A. Halanski, and W.-J. Li, "Tissue Stiffness Dictates Development, Homeostasis, and Disease Progression," *Organogenesis*, vol. 11, pp. 1–15, Jan. 2015.

[153] Y. Nematbakhsh and C. T. Lim, "Cell biomechanics and its applications in human disease diagnosis," *Acta Mech Sin*, vol. 31, pp. 268–273, Apr. 2015.

[154] F.-S. Quan and K. S. Kim, "Medical applications of the intrinsic mechanical properties of single cells," *Acta Biochimica et Biophysica Sinica*, vol. 48, pp. 865–871, Oct. 2016.

[155] C. F. Guimarães, L. Gasperini, A. P. Marques, and R. L. Reis, "The stiffness of living tissues and its implications for tissue engineering," *Nature Reviews Materials*, vol. 5, pp. 351–370, May 2020.

[156] Y. Ding, G.-K. Xu, and G.-F. Wang, "On the determination of elastic moduli of cells by AFM based indentation," *Sci Rep*, vol. 7, p. 45575, Apr. 2017.

[157] C. L. Essmann, D. Martinez-Martinez, R. Pryor, K.-Y. Leung, K. B. Krishnan, P. P. Lui, N. D. E. Greene, A. E. X. Brown, V. M. Pawar, M. A. Srinivasan, and F. Cabreiro, "Mechanical properties measured by atomic force microscopy define health biomarkers in ageing C . elegans," *Nature Communications*, vol. 11, p. 1043, Feb. 2020.

[158] L. Guillou, A. Babataheri, P.-H. Puech, A. I. Barakat, and J. Husson, "Dynamic monitoring of cell mechanical properties using profile microindentation," *Sci Rep*, vol. 6, p. 21529, Aug. 2016.

[159] Y. Zhang, F. Wei, Y.-C. Poh, Q. Jia, J. Chen, J. Chen, J. Luo, W. Yao, W. Zhou, W. Huang, F. Yang, Y. Zhang, and N. Wang, "Interfacing 3D magnetic twisting cytometry with confocal fluorescence microscopy to image force responses in living cells," *Nat Protoc*, vol. 12, pp. 1437–1450, July 2017.

[160] D. Herráez-Aguilar, E. Madrazo, H. López-Menéndez, M. Ramírez, F. Monroy, and J. Redondo-Muñoz, "Multiple particle tracking analysis in isolated nuclei reveals the mechanical phenotype of leukemia cells," *Sci Rep*, vol. 10, p. 6707, Dec. 2020.

[161] J. Guck, S. Schinkinger, B. Lincoln, F. Wottawah, S. Ebert, M. Romeyke, D. Lenz, H. M. Erickson, R. Ananthakrishnan, D. Mitchell, J. Käs, S. Ulvick, and C. Bilby, "Optical Deformability as an Inherent Cell Marker for Testing Malignant Transformation and Metastatic Competence," *Biophysical Journal*, vol. 88, pp. 3689–3698, May 2005.

[162] S. Wang and K. V. Larin, "Optical coherence elastography for tissue characterization: a review," *J. Biophoton*, vol. 8, pp. 279–302, Apr. 2015.

[163] Z. A. Steelman, D. S. Ho, K. K. Chu, and A. Wax, "Light-scattering methods for tissue diagnosis," *Optica, OPTICA*, vol. 6, pp. 479–489, Apr. 2019.

[164] W. J. Eldridge, Z. A. Steelman, B. Loomis, and A. Wax, "Optical Phase Measurements of Disorder Strength Link Microstructure to Cell Stiffness," *Biophysical Journal*, vol. 112, pp. 692–702, Feb. 2017.

[165] C. Bevilacqua, R. Prevedel, and A. Diz-Muñoz, "Brillouin microscopy measuring mechanics in biology using light," *infocus*, pp. 41–47, Mar. 2020.

[166] Z. Meng, S. C. Bustamante Lopez, K. E. Meissner, and V. V. Yakovlev, "Subcellular measurements of mechanical and chemical properties using dual Raman-Brillouin microspectroscopy," *Journal of Biophotonics*, vol. 9, no. 3, pp. 201–207, 2015.

[167] J. Zhang, F. Alisafaei, M. Nikoli, X. A. Nou, H. Kim, V. B. Shenoy, and G. Scarcelli, "Nuclear Mechanics within Intact Cells Is Regulated by Cytoskeletal Network and Internal Nanostructures," *Small*, vol. 16, p. 1907688, May 2020.

[168] H. Shams, M. Soheilypour, M. Peyro, R. Moussavi-Baygi, and M. R. K. Mofrad, "Looking Under the Hood of Cellular Mechanotransduction with Computational Tools: A Systems Biomechanics Approach across Multiple Scales," *ACS Biomater. Sci. Eng.*, vol. 3, pp. 2712–2726, Nov. 2017.

[169] F. Martino, A. R. Perestrelo, V. Vinarský, S. Pagliari, and G. Forte, "Cellular Mechanotransduction: From Tension to Function," *Front. Physiol.*, vol. 9, 2018.

[170] L. Galluzzi, T. Yamazaki, and G. Kroemer, "Linking cellular stress responses to systemic homeostasis," *Nature Reviews Molecular Cell Biology*, vol. 19, pp. 731–745, Nov. 2018.

[171] G. E. Devlin, J. L. Davis, L. Chase, and S. Geschwind, "Absorption of Unshifted Scattered Light by a Molecular I2 Filter in Brillouin and Raman Scattering," *Appl. Phys. Lett.*, vol. 19, pp. 138–141, Sept. 1971.

[172] B. L. Ibey, S. Xiao, K. H. Schoenbach, M. R. Murphy, and A. G. Pakhomov, "Plasma membrane permeabilization by 60- and 600-ns electric pulses is determined by the absorbed dose," *Bioelectromagnetics*, vol. 30, no. 2, pp. 92–99, 2009.

[173] C. C. Roth, R. A. Barnes, B. L. Ibey, H. T. Beier, L. Christopher Mimun, S. M. Maswadi, M. Shadaram, and R. D. Glickman, "Characterization of Pressure Transients Generated by Nanosecond Electrical Pulse (nsEP) Exposure," *Sci Rep*, vol. 5, p. 15063, Dec. 2015.

[174] G. Van Rossum and F. L. Drake, *Python 3 Reference Manual*. Scotts Valley, CA: CreateSpace, 2009.

[175] MATLAB, *version 7.10.0 (R2010a)*. Natick, Massachusetts: The MathWorks Inc., 2010.

[176] C. A. Lieber and A. Mahadevan-Jansen, "Automated method for subtraction of fluorescence from biological Raman spectra," *Appl Spectrosc*, vol. 57, pp. 1363–1367, Nov. 2003.

[177] B. L. Ibey, D. G. Mixon, J. A. Payne, A. Bowman, K. Sickendick, G. J. Wilmink, W. P. Roach, and A. G. Pakhomov, "Plasma membrane permeabilization by trains of ultrashort electric pulses," *Bioelectrochemistry*, vol. 79, no. 1, pp. 114–121, 2010.

[178] Z. A. Steelman, G. P. Tolstykh, H. T. Beier, and B. L. Ibey, "Cellular response to high pulse repetition rate nanosecond pulses varies with fluorescent marker identity," *Biochemical and Biophysical Research Communications*, vol. 478, no. 3, pp. 1261–1267, 2016.

[179] L. Carr, S. M. Bardet, R. C. Burke, D. Arnaud-Cormos, P. Leveque, and R. P. OConnor, "Calcium-independent disruption of microtubule dynamics by nanosecond pulsed electric fields in U87 human glioblastoma cells," *Scientific Reports*, vol. 7, p. 41267, Jan. 2017.

[180] G. P. Tolstykh, G. L. Thompson, H. T. Beier, Z. A. Steelman, and B. L. Ibey, "nsPEF-induced PIP2 depletion, PLC activity and actin cytoskeletal cortex remodeling are responsible for post-exposure cellular swelling and blebbing," *Biochemistry and Biophysics Reports*, vol. 9, no. October 2016, pp. 36–41, 2017.

[181] P. A. Pullarkat, P. A. Fernández, and A. Ott, "Rheological properties of the Eukaryotic cell cytoskeleton," *Physics Reports*, vol. 449, pp. 29–53, Sept. 2007.

[182] T.-J. Chen, C.-C. Wu, and F.-C. Su, "Mechanical models of the cellular cytoskeletal network for the analysis of intracellular mechanical properties and force distributions: A review," *Medical Engineering & Physics*, vol. 34, pp. 1375–1386, Dec. 2012.

[183] W. W. Ahmed, t. Fodor, and T. Betz, "Active cell mechanics: Measurement and theory," *Biochimica et Biophysica Acta (BBA) - Molecular Cell Research*, vol. 1853, pp. 3083–3094, Nov. 2015.

[184] L. Blanchoin, R. Boujemaa-Paterski, C. Sykes, and J. Plastino, "Actin Dynamics, Architecture, and Mechanics in Cell Motility," *Physiological Reviews*, vol. 94, pp. 235–263, Jan. 2014.

[185] G. M. Cooper, "Structure and Organization of Actin Filaments," *The Cell: A Molecular Approach. 2nd edition*, 2000.

[186] P. Chugh and E. K. Paluch, "The actin cortex at a glance," *J Cell Sci*, vol. 131, July 2018.

[187] C. A. Schneider, W. S. Rasband, and K. W. Eliceiri, "NIH Image to ImageJ: 25 years of image analysis," *Nature Methods*, vol. 9, pp. 671–675, July 2012.

[188] O. Gavet and J. Pines, "Progressive activation of CyclinB1-Cdk1 coordinates entry to mitosis," *Dev Cell*, vol. 18, pp. 533–543, Apr. 2010.

[189] Z. A. Steelman, W. J. Eldridge, and A. Wax, "Response to Comment on Is the nuclear refractive index lower than cytoplasm? Validation of phase measurements and implications for light scattering technologies," *Journal of Biophotonics*, vol. 11, no. 6, p. e201800091, 2018.

[190] M. Breton and L. M. Mir, "Microsecond and nanosecond electric pulses in cancer treatments," *Bioelectromagnetics*, vol. 33, no. 2, pp. 106–123, 2012.

[191] D. Xiao, C. Yao, H. Liu, C. Li, J. Cheng, F. Guo, and L. Tang, "Irreversible electroporation and apoptosis in human liver cancer cells induced by nanosecond electric pulses," *Bioelectromagnetics*, vol. 34, no. 7, pp. 512–520, 2013.

[192] E. Neumann, "Membrane electroporation and direct gene transfer," *Bioelectrochemistry and Bioenergetics*, vol. 28, pp. 247–267, Aug. 1992.

[193] M.-P. Rols, C. Delteil, M. Golzio, P. Dumond, S. Cros, and J. Teissie, "In vivo electrically mediated protein and gene transfer in murine melanoma," *Nature Biotechnology*, vol. 16, pp. 168–171, Feb. 1998.

[194] G. Saldaña, I. Álvarez, S. Condón, and J. Raso, "Microbiological Aspects Related to the Feasibility of PEF Technology for Food Pasteurization," *Critical Reviews in Food Science and Nutrition*, vol. 54, pp. 1415–1426, Nov. 2014.

[195] O. M. Nesin, O. N. Pakhomova, S. Xiao, and A. G. Pakhomov, "Manipulation of cell volume and membrane pore comparison following single cell permeabilization with 60- and 600-ns electric pulses," *Biochimica et Biophysica Acta (BBA) - Biomembranes*, vol. 1808, pp. 792–801, Mar. 2011.

[196] Z. N. Coker, X.-X. Liang, A. S. Kiester, G. D. Noojin, J. N. Bixler, B. L. Ibey, A. Vogel, and V. V. Yakovlev, "Synergistic effect of picosecond optical and nanosecond electrical pulses on dielectric breakdown in aqueous solutions," *Photon. Res.*, vol. 9, pp. 416–423, Mar. 2021.

[197] L. Keldysh, "The effect of a strong electric field on the optical properties of insulating crystals," *J.E.T.P.*, vol. 34 (7), pp. 788 – 790, Nov. 1958.

[198] L. Keldysh, "Ionization in the field of a strong electromagnetic wave," *Sov. Phys. JETP*, vol. 20, no. 5, pp. 1307–1314, 1965.

[199] K. G. McKay, "Avalanche Breakdown in Silicon," *Physical Review*, vol. 94, pp. 877–884, May 1954.

[200] R. R. Alfano and S. L. Shapiro, "Observation of Self-Phase Modulation and Small-Scale Filaments in Crystals and Glasses," *Physical Review Letters*, vol. 24, pp. 592–594, Mar. 1970.

[201] M. Lenzner, J. Krüger, S. Sartania, Z. Cheng, C. Spielmann, G. Mourou, and F. Kautek, "Femtosecond optical breakdown in dielectrics," *Physical Review Letters*, vol. 80, no. 18, pp. 4076–4079, 1998.

[202] A. Vogel, N. Linz, S. Freidank, and G. Paltauf, "Femtosecond-laser-induced nanocavitation in water: Implications for optical breakdown threshold and cell surgery," *Physical Review Letters*, vol. 100, no. 3, pp. 1–4, 2008.

[203] A. A. Manenkov and A. M. Prokhorov, "Laser-induced damage in solids," *Sov. Phys. Usp.*, vol. 29, pp. 104–122, Jan. 1986.

[204] P. K. Kennedy, "A First-Order Model for Computation of Laser-Induced Breakdown Thresholds in Ocular and Aqueous Media: Part ITheory," *IEEE Journal of Quantum Electronics*, vol. 31, no. 12, pp. 2241–2249, 1995.

[205] D. Hammer, R. Thomas, G. Noojin, B. Rockwell, P. Kennedy, and W. Roach, "Experimental investigation of ultrashort pulse laser-induced breakdown thresholds in aqueous media," *IEEE Journal of Quantum Electronics*, vol. 32, pp. 670–678, Apr. 1996.

[206] K. Nahen and A. Vogel, "Plasma formation in water by picosecond and nanosecond Nd:YAG laser pulses - Part II: Transmission, scattering, and reflection," *IEEE Journal on Selected Topics in Quantum Electronics*, vol. 2, no. 4, pp. 861–871, 1996.

[207] B. A. Rockwell, R. J. Thomas, and A. Vogel, "Ultrashort laser pulse retinal damage mechanisms and their impact on thresholds," *Medical Laser Application*, vol. 25, no. 2, pp. 84–92, 2010.

[208] N. Linz, S. Freidank, X. X. Liang, H. Vogelmann, T. Trickl, and A. Vogel, "Wavelength dependence of nanosecond infrared laser-induced breakdown in water: Evidence for multiphoton initiation via an intermediate state," *Physical Review B - Condensed Matter and Materials Physics*, vol. 91, no. 13, pp. 1–10, 2015.

[209] N. Linz, S. Freidank, X. X. Liang, and A. Vogel, "Wavelength dependence of femtosecond laser-induced breakdown in water and implications for laser surgery," *Physical Review B*, vol. 94, no. 2, pp. 1–19, 2016.

[210] N. Bloembergen, "Laser-induced electric breakdown in solids," *IEEE Journal of Quantum Electronics*, vol. 10, pp. 375–386, Mar. 1974.

[211] J. M. Wiesenfeld and E. P. Ippen, "Dynamics of electron solvation in liquid water," *Chemical Physics Letters*, vol. 73, pp. 47–50, July 1980.

[212] Z. Zhu, A. Chutia, H. Tsuboi, M. Koyama, A. Endou, H. Takaba, M. Kubo, C. A. D. Carpio, P. Selvam, and A. Miyamoto, "Theoretical Simulation of Dielectric Breakdown by Molecular Dynamics and Tight-Binding Quantum Chemistry Methods," *Japanese Journal of Applied Physics*, vol. 46, pp. 1853–1858, Apr. 2007.

[213] B. Rethfeld, "Unified model for the free-electron avalanche in laser-irradiated dielectrics," *Physical Review Letters*, vol. 92, no. 18, pp. 1–4, 2004.

[214] B. Rethfeld, "Free-electron generation in laser-irradiated dielectrics," *Physical Review B*, vol. 73, Jan. 2006.

[215] B. H. Christensen and P. Balling, "Modeling ultrashort-pulse laser ablation of dielectric materials," *Physical Review B - Condensed Matter and Materials Physics*, vol. 79, no. 15, pp. 1–10, 2009.

[216] K. Wædegaard, D. B. Sandkamm, L. Haahr-Lillevang, K. G. Bay, and P. Balling, "Modeling short-pulse laser excitation of dielectric materials," *Applied Physics A*, vol. 117, pp. 7–12, Jan. 2014.

[217] B. Gorshkov, A. Epifanov, A. A. Manenkov, and A. Panov, "Studies of Laser-Produced Damage toTransparent Optical Material in the UV Region and in Crossed UV-IR Beams," in *Proceedings, Thirteenth Annual Symposiumon Optical Materials for High Power Lasers*, pp. 76–86, Nov. 1981.

[218] A. Robledo-Martinez, H. M. Sobral, and L. A. Garcia-Villarreal, "Signal Enhancement in Laser-Induced Breakdown Spectroscopy Using Gated High-Voltage Pulses," *IEEE Transactions on Plasma Science*, vol. 46, no. 7, pp. 2392–2396, 2018.

[219] R. A. Mullen and J. N. Matossian, "Quenching optical breakdown with an applied electric field," *Optics Letters*, vol. 15, no. 11, p. 601, 1990.

[220] E. Y. Loktionov, N. A. Pasechnikov, A. V. Pavlov, Y. S. Protasov, and V. D. Telekh, "Investigation of electrooptical breakdown threshold in gas mixtures of complex chemical composition," *Journal of Physics: Conference Series*, vol. 652, p. 012043, Nov. 2015.

[221] E. Takahashi and S. Kato, "Influence of DC electric field on Nd:YAG laser-induced breakdown in gases," *OSA Continuum*, vol. 3, p. 3030, Nov. 2020.

[222] J. Tulip and H. Seguin, "Influence of a transverse electric field on laserinduced gas breakdown," *Appl. Phys. Lett.*, vol. 23, pp. 135–136, Aug. 1973.

[223] N. Kroll and K. M. Watson, "Theoretical Study of Ionization of Air by Intense Laser Pulses," *Physical Review A*, vol. 5, pp. 1883–1905, Apr. 1972.

[224] H. S. Smalø, y. Hestad, S. Ingebrigtsen, and P.-O. Åstrand, "Field dependence on the molecular ionization potential and excitation energies compared to conductivity models for insulation materials at high electric fields," *Journal of Applied Physics*, vol. 109, p. 073306, Apr. 2011.

[225] A. Vogel, J. Noack, G. Hüttman, and G. Paltauf, "Mechanisms of femtosecond laser nanosurgery of cells and tissues," *Applied Physics B: Lasers and Optics*, vol. 81, no. 8, pp. 1015–1047, 2005.

[226] X.-X. Liang, Z. Zhang, and A. Vogel, "Multi-rate-equation modeling of the energy spectrum of laser-induced conduction band electrons in water," *Optics Express*, vol. 27, p. 4672, Feb. 2019.

[227] F. Williams, S. P. Varma, and S. Hillenius, "Liquid water as a lone-pair amorphous semiconductor," *The Journal of Chemical Physics*, vol. 64, pp. 1549–1554, Feb. 1976.

[228] P. Vanraes and A. Bogaerts, "Plasma physics of liquidsA focused review," *Applied Physics Reviews*, vol. 5, p. 031103, Sept. 2018.

[229] C. DeMichelis, "Laser induced gas breakdown: A bibliographical review," *IEEE Journal of Quantum Electronics*, vol. 5, pp. 188–202, Apr. 1969.

[230] C. Cain, G. Noojin, and L. Manning, "A Comparison Of Various Probit Methods For Analyzing Yes/No Data On A Log Scale," *AL/OE-TR-1996-0102: 46*, p. 44, 1996.

[231] T. Kovalchuk, G. Toker, V. Bulatov, and I. Schechter, "Laser breakdown in alcohols and water induced by 1064nm nanosecond pulses," *Chemical Physics Letters*, vol. 500, pp. 242–250, Nov. 2010.

[232] B. Varghese, S. Turco, V. Bonito, and R. Verhagen, "Effects of polarization and apodization on laser induced optical breakdown threshold," *Optics Express*, vol. 21, p. 18304, July 2013.

[233] C. A. Sacchi, "Laser-induced electric breakdown in water," *Journal of the Optical Society of America B*, vol. 8, no. 2, p. 337, 1991.

[234] A. Vogel, J. Noack, K. Nahen, D. Theisen, S. Busch, U. Parlitz, D. X. Hammer, G. D. Noojin, B. A. Rockwell, and R. Birngruber, "Energy balance of optical breakdown in water at nanosecond to femtosecond time scales," *Applied Physics B: Lasers and Optics*, vol. 68, no. 2, pp. 271–280, 1999.

[235] D. N. Nikogosyan, A. A. Oraevsky, and V. I. Rupasov, "Two-photon ionization and dissociation of liquid water by powerful laser UV radiation," *Chemical Physics*, vol. 77, pp. 131–143, May 1983.

[236] D. W. Shoesmith and W. Lee, "The ionization constant of heavy water (D $_2$$ O) in the temperature range 298 to 523 K," *Can. J. Chem.*, vol. 54, pp. 3553–3558, Nov. 1976.

[237] G. A. Vidulich, D. F. Evans, and R. L. Kay, "The dielectric constant of water and heavy water between 0 and 40.degree.," *J. Phys. Chem.*, vol. 71, pp. 656–662, Feb. 1967.

[238] G. Veda Prakash, R. Kumar, K. Saurabh, Nasir, V. P. Anitha, M. B. Chowdhuri, and A. Shyam, "Comparative study of electrical breakdown properties of deionized water and heavy water under pulsed power conditions," *Review of Scientific Instruments*, vol. 87, p. 015115, Jan. 2016.

[239] C. F. Perry, P. Zhang, F. B. Nunes, I. Jordan, A. von Conta, and H. J. Wörner, "Ionization Energy of Liquid Water Revisited," *J. Phys. Chem. Lett.*, vol. 11, pp. 1789–1794, Mar. 2020.

[240] M. F. Yanik, H. Cinar, H. N. Cinar, A. D. Chisholm, Y. Jin, and A. Ben-Yakar, "Functional regeneration after laser axotomy," *Nature*, vol. 432, pp. 822–822, Dec. 2004.

[241] E. Wenande, R. R. Anderson, and M. Haedersdal, "Fundamentals of fractional laser-assisted drug delivery: An in-depth guide to experimental methodology and data interpretation," *Advanced Drug Delivery Reviews*, vol. 153, pp. 169–184, Jan. 2020.

[242] G. Campargue, B. Zielinski, S. Courvoisier, C. Sarpe, T. Winkler, A. Sentfleben, L. Bonacina, T. Baumert, and J. P. Wolf, "Live cells assessment of opto-poration by a single femtosecond temporal Airy laser pulse," *AIP Advances*, vol. 8, p. 125105, Dec. 2018.

[243] H. Schneckenburger, "Laser-assisted optoporation of cells and tissues a mini-review," *Biomedical Optics Express*, vol. 10, no. 6, p. 2883, 2019.

[244] S. Patskovsky, M. Qi, and M. Meunier, "Single point single-cell nanoparticle mediated pulsed laser optoporation," *The Analyst*, vol. 145, no. 2, pp. 523–529, 2020.

[245] H. T. Beier, C. C. Roth, J. N. Bixler, A. V. Sedelnikova, and B. L. Ibey, "Visualization of Dynamic Sub-microsecond Changes in Membrane Potential," *Biophysical Journal*, vol. 116, pp. 120–126, Jan. 2019.

[246] J. Liang, P. Wang, L. Zhu, and L. V. Wang, "Single-shot stereo-polarimetric compressed ultrafast photography for light-speed observation of high-dimensional optical transients with picosecond resolution," *Nat Commun*, vol. 11, p. 5252, Dec. 2020.

[247] T. Kim, J. Liang, L. Zhu, and L. V. Wang, "Picosecond-resolution phase-sensitive imaging of transparent objects in a single shot," *Science Advances*, vol. 6, p. eaay6200, Jan. 2020.

[248] C. A. Casacio, L. S. Madsen, A. Terrasson, M. Waleed, K. Barnscheidt, B. Hage, M. A. Taylor, and W. P. Bowen, "Quantum correlations overcome the photodamage limits of light microscopy," *arXiv:2004.00178 [physics, physics:quant-ph]*, Sept. 2020.

[249] S. H. Chung and E. Mazur, "Surgical applications of femtosecond lasers," *Journal of Biophotonics*, vol. 2, no. 10, pp. 557–572, 2009.

[250] S. C. Jeoung, M. S. Sidhu, J. S. Yahng, H. J. Shin, and G. Baik, "Application of ultrafast laser optoperforation for plant pollen walls and endothelial cell membranes," in *Advances in Lasers and Electro Optics*, ch. 35, IntechOpen, 2010.

[251] P. Ronchi, S. Terjung, and R. Pepperkok, "At the cutting edge: Applications and perspectives of laser nanosurgery in cell biology," *Biological Chemistry*, vol. 393, no. 4, pp. 235–248, 2012.

[252] C. L. Hoy, O. Ferhanolu, M. Yildirim, K. H. Kim, S. S. Karajanagi, K. M. C. Chan, J. B. Kobler, S. M. Zeitels, and A. Ben-Yakar, "Clinical ultrafast laser surgery: Recent advances and future directions," *IEEE Journal on Selected Topics in Quantum Electronics*, vol. 20, no. 2, 2014.

APPENDIX A

THE WAVE EQUATION FROM MAXWELL'S EQUATIONS

Maxwell's equations, which provide a foundation for all electromagnetic theory are given in differential form as:

$$\begin{aligned} \nabla \cdot \mathbf{E} &= \frac{\rho}{\epsilon_0} \\ \nabla \cdot \mathbf{B} &= 0 \\ \nabla \times \mathbf{E} &= -\frac{\partial \mathbf{B}}{\partial t} \\ \nabla \times \mathbf{B} &= \mu_0 \left(\mathbf{J} + \epsilon_0 \frac{\partial \mathbf{E}}{\partial t} \right) \end{aligned} \tag{A.1}$$

Maxwell's equations introduce the electric field $\mathbf{E}$ and the magnetic field $\mathbf{B}$, and includes the source variables of electric charge density ρ and electric current density $\mathbf{J}$. Also included are the *universal constants* for the permittivity of free space $\epsilon_0 \approx 8.854 \times 10^{-12}$ Farads/meter, and permeability of free space $\mu_0 = 4\pi \times 10^{-7}$ Henries/meter.

We can derive the standard wave equation for the electric field $\mathbf{E}$ by first taking the curl of the third equation above, that is:

$$\nabla \times (\nabla \times \mathbf{E}) = \nabla \times \left(-\frac{\partial \mathbf{B}}{\partial t} \right) \tag{A.2}$$

Making use of the vector identity $\nabla \times (\nabla \times \mathbf{E}) = \nabla(\nabla \cdot \mathbf{E}) - \nabla^2 \mathbf{E}$ on the left-hand side, noting that $\nabla \cdot \mathbf{E} = 0$, and while substituting in the fourth Maxwell equation above for the right-hand side, i.e. ($\nabla \times \mathbf{B} = \mu_0 \epsilon_0 \frac{\partial \mathbf{E}}{\partial t}$), we get:

$$\nabla \times (\nabla \times \mathbf{E}) = -\nabla^2 \mathbf{E} = \nabla \times \left(-\frac{\partial \mathbf{B}}{\partial t} \right) // = -\frac{\partial}{\partial t}(\nabla \times \mathbf{B}) = -\mu_0 \epsilon_0 \frac{\partial^2 \mathbf{E}}{\partial t^2} \tag{A.3}$$

Which, when taking the second and last terms reduces to:

$$\nabla^2 \mathbf{E} = \mu_0 \epsilon_0 \frac{\partial^2 \mathbf{E}}{\partial t^2} \tag{A.4}$$

Finally, we arrive at the wave equation through subtracting the right-hand side term from both sides, noting that the quantities μ_0 and ϵ_0 have dimensions (F/m) and (H/m), respectively, and when written in terms of their base SI units are $(s^4 A^2/kg\ m^2)/m$ and $(kg\ m^2/s^2 A^2)/m$, which is of the unit form s^2/m^2. Therefore, we find that that $c = \frac{1}{\sqrt{\mu_0 \epsilon_0}}$. This gives:

$$\nabla^2 \mathbf{E} - \frac{1}{c^2} \frac{\partial^2 \mathbf{E}}{\partial t^2} = 0 \tag{A.5}$$

One can derive the wave equation for the magnetic field using a similar approach, yielding the same result, in terms of field **B**. This equation has solutions in the form of infinite plane waves:

$$\mathbf{E} = \mathbf{E}_0 e^{i(\mathbf{k}\cdot\mathbf{r} - \omega t)} + c.c. \tag{A.6}$$

where *c.c.* is the complex conjugate of the first part of the equation. The simplest solutions to these differential equations can be expressed in terms of simple sinusoidal wave functions traveling in one dimension with amplitude A:

$$E(x,t) = A\cos\left(kx - \omega t + \theta\right) \tag{A.7}$$

where $k = 2\pi/\lambda$ is the wavenumber, $\omega = 2\pi f$ is the angular frequency, and λ the wavelength, and θ the phase constant, or phase shift. This solution also has the variable relations $c = \omega/k = 1/\sqrt{\mu\epsilon} = \lambda f = \nu$. Furthermore, it is not uncommon to see this solution to the wave equation written in the form of $E(x,t) = A\cos(\varphi)$, where the phase φ encompasses everything within the cosine term. In this case, the angular frequency and wave vector can be expressed as $\omega = -\partial\varphi/\partial t$ and $k = \partial\varphi/\partial t$.

APPENDIX B

A PROPOSED UNIT FOR UNIFIED BRILLOUIN REPORTING

Significant variability can be found regarding the specific quantities notation and symbolism throughout the literature reporting Brillouin spectroscopy experimental procedures and results. Generally, each laboratory group tends to have their own preferred selection, ranging from ω, Ω, ω_B to $\Delta\nu, \Delta f$, and so on. These variations come from individual preferences for symbolism, and through happenstance, however they can make understanding specific values in relation to other experiments and reports rather tedious. This tedium is further compounded by the fact that comparing results from various Brillouin spectroscopy experiments is rarely direct, as the magnitude of the Brillouin frequency shift is inversely proportional to the wavelength of incident light, and naturally, many different light sources and wavelengths are desirable for specific experimental conditions and setups. During a recent Brillouin microscopy-focused workshop in Europe, this issue was brought to light and a method to address it was proposed [47]. The proposed solution is the use of a dimensionless quantity, referred to as the *Brillouin elastic contrast*, which should not require much in the way of additional measurements or assumptions and could be used as a "normalized Brillouin frequency shift" based on a common material, by which measurements could be more easily compared across different systems and wavelengths. The proposed *Brillouin elastic contrast* is given by equation B.1:

$$\overline{\nu}_B = \nu_B / \nu_B^{(w)} - 1 \tag{B.1}$$

Where ν_B is the measured Brillouin frequency shift in the sample and $\nu_B^{(w)}$ is the Brillouin frequency shift of distilled water measured using the same setup under the same thermodynamic conditions as those for the sample. $\overline{\nu}_B$ is therefore independent of the laser wavelength, and can generally approximate correction for various conditions such as temperature and objective numerical aperture (provided the measurements are taken using the same objective).

Similarly, a normalized Brillouin linewidth measurement, referred to as the *Brillouin viscous*

contrast is given by

$$\overline{\Gamma}_B = \Gamma_B / \Gamma_B^{(w)} - 1 \tag{B.2}$$

Naturally, the naming convention is intended to reflect to both the means by which the value was measured (Brillouin spectroscopy), the information it conveys (elasticity and viscosity for $\overline{\nu}_B$ and $\overline{\Gamma}_B$ respectively).

APPENDIX C

ADDITIONAL DETAIL ON EXPERIMENTAL DESIGN FOR OPTO-ELECTRIC BREAKDOWN THRESHOLDS

A schematic of the experimental setup is provided in Fig. 5.1 of the main text. The following sections provide more specific detail on the individual pieces of equipment used in the experimental setup and the results regarding breakdown thresholds on laser polarization dependence. The final section of this appendix includes a discussion on preliminary experimental data and results while attempting concurrent nsPEF and optical pulse exposures with cells in cell culture conditions.

C.1 Optical breakdown detection

A 1064 nm picosecond laser with ∼14-ps pulse duration (APL-X 1064-532; Attodyne Inc. Toranto, Ontario) was used to initiate breakdown in target solutions. The 1064 nm pulse width was measured to be 14 ś 2 ps using two distinct measurement tools: an autocorrelator and a streak camera. The 1064 nm beam was expanded and combined with an 80 MHz 485 nm laser with 0.4 mW average power (LDH-P-C-485 series, PDL 800-B driver; PicoQuant GmbH. Berlin, Germany) through a beam splitting cube. A half-waveplate was placed in the path of the 1064 nm beam before the combining cube to control the pulse energy. The energy directed away from the microscope was deflected to a photodiode (ET-2030; Electro-Optics Technology, Inc. Traverse City, MI, USA) and used for triggering of an oscilloscope (TDS3054C; TekTronix, Beaverton, OR, USA) which was utilized for temporal measurements and breakdown detection. The 485 nm coaligned laser acted as both an alignment beam for the invisible NIR laser and as an optical probe for detecting breakdown events at the focal volume through deflection methods. A 50/50 beam splitter deflected approximately 50% NIR pulse energies to an energy meter (J3-09; Coherent, Inc. Santa Clara, CA, USA) that was used to calculate pulse energies delivered to the sample for each pulse. A ratio of pulse energy at the detector and objective was recorded at the start of experiments each day. Each laser pulse was measured at this beam splitter during all experiments and then multiplied by

the appropriate energy ratio. The measured and calculated energy of every pulse was recorded. Recording the energy delivered by every pulse in an experiment allowed allowed for us to account for any pulse-to-pulse variability in the laser system. The combined beams were coupled into the rear port of an inverted microscope (DMI 4000B; Leica Microsystems, Wetzlar, Germany) and focused through a 20X, 0.4 NA microscope objective (HCX PL Fluotar; Leica Microsystems). Light after the sample was collected and passed through a 750 nm short-pass filter (FESH0750; ThorLabs, Inc. Newton, NJ, USA) and focused to an AC-coupled amplified photodiode (PDA10A Si Amplified detector; ThorLabs, Inc.) that measured the intensity of the 485 nm probe-beam. As the 1064 nm picosecond pulses caused breakdown in the sample, they would distort the focal volume and thereby deflect the 485 nm probe beam, reducing the signal intensity measured at the photodiode. The AC-coupling and 80 MHz repetition rate of the 485 nm laser helped to detect very small, short-lived bubbles that would otherwise have been invisible to a DC- coupled detector or CW source, as the scattered signal in these cases is considerably small compared to the total transmitted light through the focal volume. Finally, an additional half-waveplate was placed just before the microscope to control laser polarization angle and test for any dependence of breakdown thresholds on the laser polarization with respect to the electric field direction.

C.2 Electrical impulse delivery system

The nanosecond electric impulse was delivered to the sample across a pair of tungsten electrodes 0.125 mm in diameter, spaced roughly 200 mm apart, placed approximately 200 mm above the cover glass of a petri dish and positioned with the focal volume of our probe-beam at the center. A bright field image of the electrodes with a highlighted region for the focal volume is shown alongside a COMSOL Multiphysics® simulation of the approximate electric field distribution between the electrodes in Fig. C.1. Additional numerical simulations have previously been reported showing dependence of electrode positioning on electric field distribution between the electrodes [172]. The electrical system driving the impulse utilized a Model 350 high-power pulse generator (Velonex, Inc.) that provided a wide range of electrical pulse widths and intensities ranging from 100 ns to 300 ms up to 2.1 kV. A pulse delay generator (DG535; Stanford Research Systems, Inc.)

was used to trigger both the optical and electrical components and allowed for repeatable and precise trigger timing of all pulses. The Model 350 was set to specific voltages between 0 V and 2 kV for all experiments with impulse time of 600 ns in all cases. The resultant electric field was dependent on the separation distance and thickness of the electrodes as well as conductivity of the examined medium. Low conductivity solutions, such as pure water inhibit current flow and thus provide for a higher measured voltage across the electrodes. Conversely, higher conductivity solutions allow easier current flow across the electrodes and thus a lower electric field. For example, the electric field measured with the Model 350 set to an output voltage of 1 kV was approximately 800 V across the electrodes ($\sim$40 kV/cm) in pure water (MiliQ Milipore; 18.2 MW·cm), and approximately 365 V ($\sim$18 kV/cm) in cell imaging buffer solution (69.8 W·cm). We triggered the Model 350 with a 600 ns square pulse throughout the study, resulting in a trapezoidal profile output pulse with approximately 100 ns observed rise time, 500 ns working time, and 30 ns fall time.

C.3 Examining the polarization dependence

We investigated the impact of incident laser polarization on the reduction of E_{th}, with respect to the direction of applied nsEP (at 40 kV/cm) in pure water (MiliQ Milipore 18 MW·cm). We tested the laser polarization angle by measuring E_{th} in pure water with 40 kV/cm nsEP while rotating the polarizer in increments of 15°from 0°to 45°thereby rotating our plane of polarization across a full 90°range. Results are demonstrated in Fig. C.2. We found a negligible maximum difference of 1.2% across all measurements with an average threshold of $E_{th} = 0.713\ \ 0.004\ \mu J$. We, therefore, observed no polarization dependence beyond statistical errors, further suggesting that psLP dominates the breakdown initiation process and nsEP produces little to no impact beyond providing additional seed electrons.

C.4 Application to cell-based studies and targeted response

Within the last year, an investigation began into testing cellular responses to nsPEF with the intent of combining picosecond laser pulse exposures, following the exposure protocols discussed in the main text. Previous researchers have demonstrate that optical pulses can cause optopo-

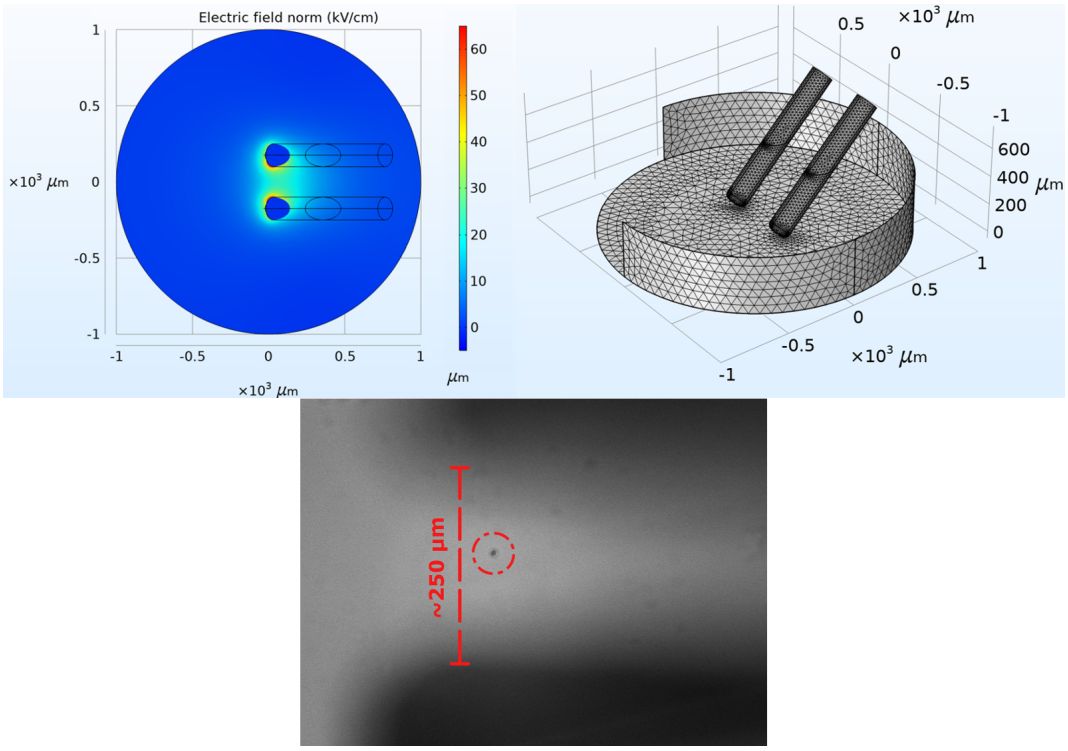

Figure C.1: Electric impulse delivery system: Electric field distribution and example of simulation mesh as determined by COMSOL Multiphysics® software (Top) and microscope bright field view of electrodes and laser-induced damage on a substrate for focal volume reference.

ration type effects and micro-bubble formation leading to destabilization of cell plasma membranes, which can enable the uptake of nano-dyes as well as initiate drug delivery and DNA transfection[244]. Furthermore, ultra-fast lasers (< 250 fs) have been utilized in the study and development of micro- and nano-scale surgeries [249, 250, 251, 252]. The applications of laser pulses for membrane permeabilization are very similar to those of nsEP discussed in the main text. We, therefore, have developed a study to attempted to apply a combination of these exposures (psLP + nsEP) on cells. We have modeled this study to reflect common nsEP-based nanoporation studies utilizing YO-PRO-1 dye a marker for cell membrane permeabilization. We present our first preliminary results in Fig. C.3. The fluorescent images shown in Fig. C.3 represent our first attempt at testing the individual and combined exposure conditions. We used a confocal microscope (Zeiss LSM 710; Carl Zeiss MicroImaging GmbH, Jena, Germany) with DIC40X 1.2NA objective (Carl Zeiss MicroImaging) in conjunction with the ZEN 2012 software (Zen 2012 SP1

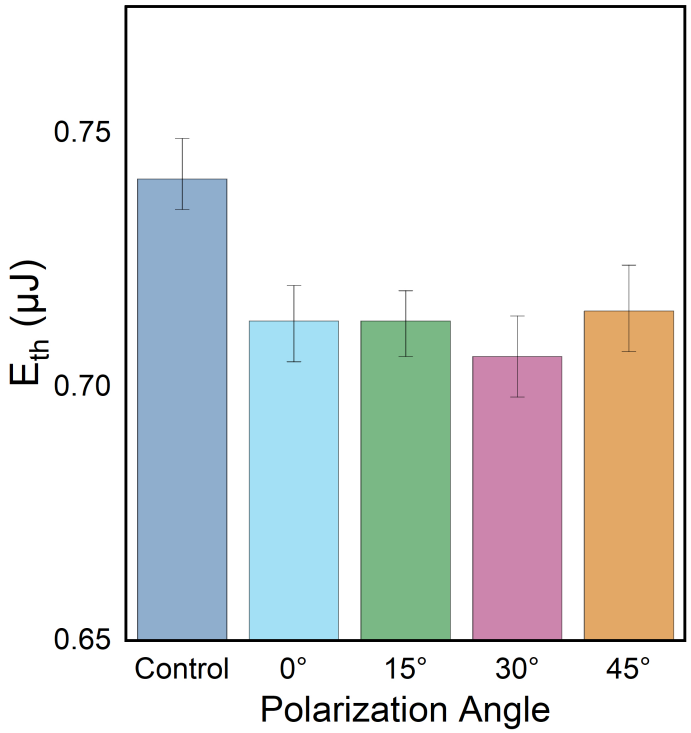

Figure C.2: Polarization-dependence testing: E_{th} dependence on incident laser polarization angle with respect to electric field direction. E_{th} measurements recorded in water for each respective laser polarization angle as it was coupled into microscope and focused to sample medium.

Black Edition Ver. 8,1,3,484, Carl Zeiss Microscopy GmbH) to acquire images of CHO-K1 cells and YO-PRO-1 dye uptake after exposures. The psLP was capable of selectively destroying or removing cells from the substrate surface layer without inducing obvious damage to neighboring cells, but did induce some dye uptake, indicating minor levels of membrane disruption. nsEP exposure induced dye uptake, as expected. Interestingly, when the laser was brought below breakdown threshold energy and combined with nsEP (psLP + nsEP), we saw a reduction in uptake in cells in the region immediately around the psLP focal region (shown in Fig. C.3). We hope to continue our study beyond this preliminary phase of research to investigate potential for long-term damage to cells under concurrent exposures, to develop specific targeted control or inhibition protocols. Selective control of cell responses to these types of exposures will allow for more specific targeted dye uptake procedures, and later to specified targeted drug delivery and DNA transfection.

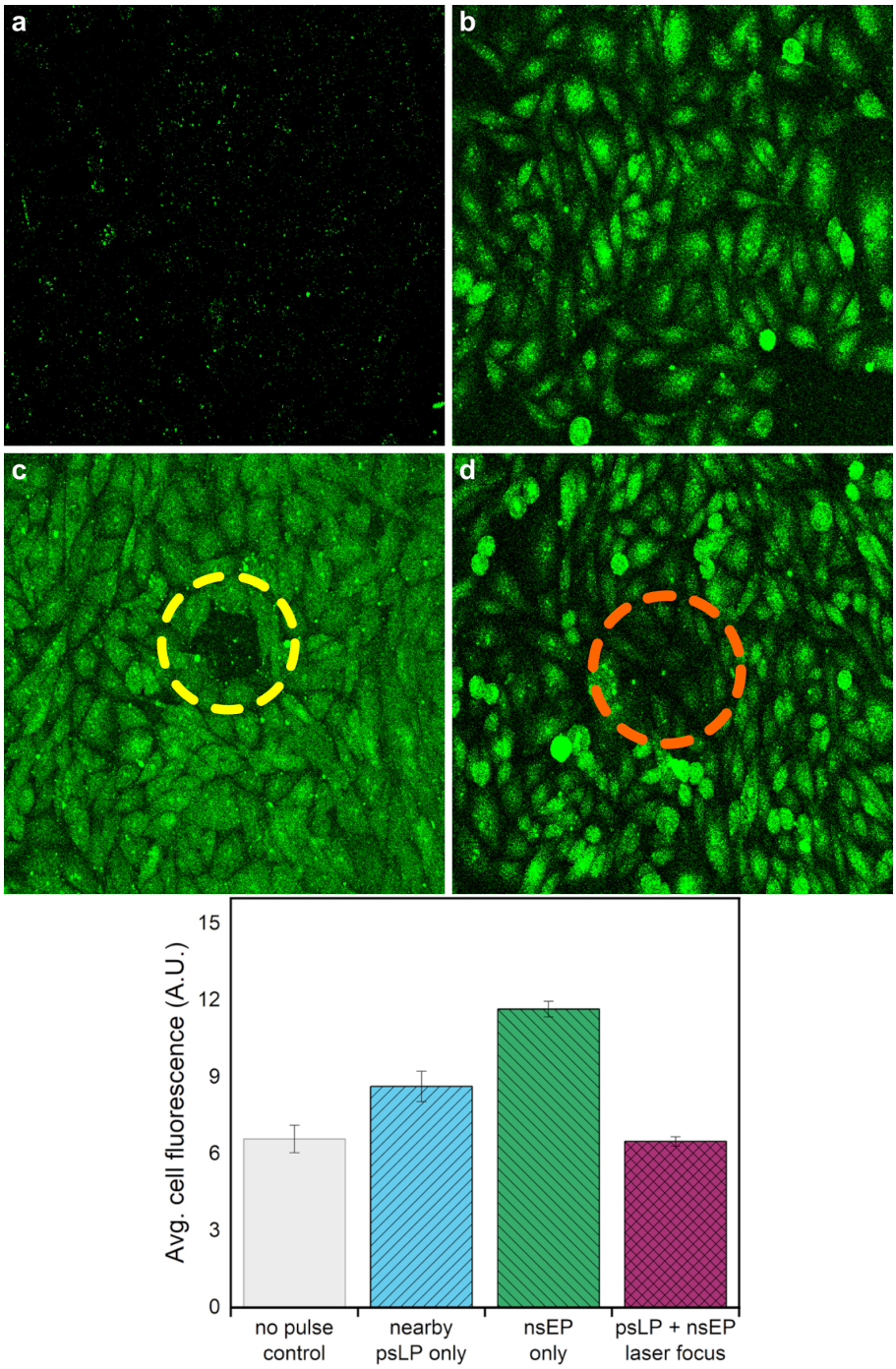

Figure C.3: Preliminary results for concurrent exposures and cell-based studies. Fluorescent images showing YO-PRO-1 dye uptake under (a) control, (b) nsEP alone, (c) psLP alone, and (d) combined psLP+nsEP exposure conditions. Yellow dashed circle in c indicates where cells were removed from culture layer by breakdown event. Orange dashed circle in (d) indicates where psLP was focused above cells and an area of reduced YO-PRO dye uptake in targeted cells, compared to surrounding cells exposed to nsEP.